

REPORT DOCUMENTATION PAGE

Form Approved
OMB No. 0704-0188

AD-A235 309



2

To average 1 hour per response, including the time for reviewing instructions, searching existing data sources, writing the collection of information, and completing and reviewing the collection of information. Send comments regarding this burden estimate or any other aspect of the report to Washington Headquarters Services, Directorate for Information Operations and Research, 1215 Jefferson Davis Highway, Suite 1204, Arlington, VA 22202-4302, Attention: Director, Reporters and Analysts, DOD Form 14 (GSA FPMR (41 CFR) 101-11, subpart J, 35 CFR 1.11) and the Office of Management and Budget, Paperwork Reduction Project (0704-0188), Washington, DC 20503.

DATE July 1991	3. REPORT TYPE AND DATES COVERED Final Report 1/1/88 to 12/31/90
-------------------	---

5. FUNDING NUMBERS

61102F 2303/B1

4. TITLE AND SUBTITLE

Boron Combustion Model Development with Kinetic Sensitivity Analysis and Measurement of Key Chemical Rate Parameters

6. AUTHOR(S)

R. C. Brown, C. E. Kolb, S. Y. Cho, R. A. Yetter,
H. R. Rabitz, and F. L. Dryer

7. PERFORMING ORGANIZATION NAME(S) AND ADDRESS(ES)

Aerodyne Research, Inc.
Billerica, MA 01821

AFOSR-TR-

8. PERFORMING ORGANIZATION REPORT NUMBER

91 0337

9. SPONSORING/MONITORING AGENCY NAME(S) AND ADDRESS(ES)

AFOSR/NC
Building 410
Bolling AFB, DC 20332-6448

10. SPONSORING/MONITORING AGENCY REPORT NUMBER

F49620-88-C-0048

11. SUPPLEMENTARY NOTES

12a. DISTRIBUTION/AVAILABILITY STATEMENT

Approved for public release; distribution is unlimited

12b. DISTRIBUTION CODE

13. ABSTRACT (Maximum 200 words)

See Back

APR 6 1991



Accession For

NTIS GRANT	<input type="checkbox"/>
DTIC TAB	<input type="checkbox"/>
Unannounced	<input type="checkbox"/>
Justification	<input type="checkbox"/>

By

Distribution/

Availability Code

Avail. Subject

Dist Special

A-1

14. SUBJECT TERMS

15. NUMBER OF PAGES

106

16. PRICE CODE

17. SECURITY CLASSIFICATION OF REPORT
UNCLASSIFIED18. SECURITY CLASSIFICATION OF THIS PAGE
UNCLASSIFIED19. SECURITY CLASSIFICATION OF ABSTRACT
UNCLASSIFIED20. LIMITATION OF ABSTRACT
SAR

91426004

13. This report presents kinetics models for the chemically facilitated gasification of the ubiquitous boron oxide coating that inhibits particulate boron ignition and the second stage high temperature boron surface burning that occurs once the oxide coating has been removed. These models include a homogeneous gas phase oxidation mechanism consisting of 19 chemical species and 58 forward and reverse elementary reactions, multicomponent gas phase diffusion and heterogeneous reactions between gas phase oxidation products and the boron oxide/boron surface. Kinetic mechanisms are formulated to describe the heterogeneous surface reactions for both $B_2O_3(l)$ and $B(s)$ surfaces in terms of simple adsorption and desorption reaction steps. Thermochemical parameters for these reaction steps are estimated from the current heats of formation and gas phase bond energies for the major reactants. Reaction rate parameters are estimated from available experimental data or using elementary transition state theory arguments.

The kinetic processes are treated using a generalized kinetics computer code, with embedded gradient sensitivity analysis, for chemically reacting flows. This code was developed to provide a quantitative model for the nonsteady-state combustion of a one-dimensional (particle radius) spherical particle. This code uses a non-linear, implicit partial differential equation solver with fully automatic time step/mode control that is compatible with formal gradient sensitivity analysis techniques.

BORON COMBUSTION MODEL DEVELOPMENT WITH
KINETIC SENSITIVITY ANALYSIS AND
MEASUREMENT OF KEY CHEMICAL
RATE PARAMETERS

Prepared by

R.C. Brown and C.E. Kolb
Center of Chemical and Environmental Physics
Aerodyne Research, Inc.
45 Manning Road
Billerica, MA 01821

and

S.Y. Cho, R.A. Yetter and F.L. Dryer
Department of Mechanical and Aerospace Engineering
Princeton University
Princeton, NJ 08544

and

H.R. Rabitz
Department of Chemistry
Princeton University
Princeton, NJ 08544

Prepared for

L.P. Davis
Chemical and Atmospheric Sciences Directorate
Air Force Office of Scientific Research
Bolling Air Force Base
Washington, D.C. 20332

January 1991

PROJECT SUMMARY

Title: Boron Combustion Model Development with Kinetic Sensitivity Analysis
and Measurement of Key Chemical Rate Parameters

Principal Investigators: Dr. C.E. Kolb

Center of Chemical and Environmental Physics
Aerodyne Research, Inc.
Billerica, MA 01821

Drs. F.L. Dryer and R.A. Yetter
Department of Mechanical and Aerospace Engineering
Princeton University
Princeton, NJ 08544

Research Personnel: Dr. R.C. Brown, Aerodyne Research, Inc.

Dr. K.D. Annen, Aerodyne Research, Inc.

Dr. H. Rabitz, Princeton University

Dr. S.Y. Cho, Princeton University

Inclusive Dates: 1 January 1988 - 31 December 1990

Contract Number: F49620-88-C-0048

Research Objective: To develop a physical and chemical model for particulate boron-assisted hydrocarbon combustion and to use gradient sensitivity analysis to identify key chemical reaction mechanisms and critical uncertainties in thermochemical and kinetic parameters.

Presentations and papers:

- (1) R.C. Brown, C.E. Kolb, H. Rabitz, S.Y. Cho, R.A. Yetter and F.L. Dryer, "Kinetic Model for Liquid B₂O₃ Gasification in a Hydrocarbon Combustion Environment: I. Heterogeneous Surface Reactions," accepted for publication in the International Journal of Chemical Kinetics, 1991.
- (2) S.Y. Cho, R.A. Yetter, F.L. Dryer, R.C. Brown, C.E. Kolb and H. Rabitz, "Kinetic Model for Liquid B₂O₃ Gasification in a Hydrocarbon Combustion Environment: II. Model Results with Gradient Sensitivity Analysis," to be submitted to the International Journal of Chemical Kinetics, 1991.
- (3) R.C. Brown, C.E. Kolb, H. Rabitz, S.Y. Cho, R.A. Yetter and F.L. Dryer, "Homogeneous and Heterogeneous Kinetic Models for Hydrocarbon Assisted Boron Combustion," Invited paper to be presented at the Symposium on Gas-Phase Metal Reactions, 4th Chemical Congress of North America, New York City, August, 1991 and published in the Symposium's proceedings.

(4) R.C. Brown, C.E. Kolb, H. Rabitz, S.Y. Cho, R.A. Yetter and F.L. Dryer
"Kinetic Model for High Temperature Hydrocarbon Assisted Boron
Combustion," submitted to the International Journal of Chemical
Kinetics, 1991.

Summary of Accomplishments:

(1) Previous and ongoing experimental research and modeling efforts were reviewed and key issues for detailed studies were identified.

(2) Thermochemical data (entropies, heats of formation and bond energies) for all relevant species were reviewed and the most recent data was incorporated into the combustion model.

(3) A one dimensional, nonsteady-state model for the combustion of a spherical particle was formulated and the associated computer codes developed. This model can currently treat particle shrinkage, density changes, multi-component gas phase diffusion to the particle surface, Stefan flux radiative heat transfer, and homogeneous (gas/gas) and heterogeneous (gas/solid) chemical reactions.

(4) Gradient sensitivity analysis techniques were extended to heterogeneous kinetic systems with spatial and temporal dependence and the computational methodology needed to compute sensitivity coefficients were incorporated into the computer codes.

(5) The most potentially important heterogeneous surface reactions were identified, elementary kinetic mechanisms were formulated, and reaction enthalpies and rate parameters were generated from available experimental data or estimated from elementary transition state arguments.

(6) Model results were obtained for the gasification of a liquid boron oxide particle and for the surface oxidation of a solid boron particle.

ABSTRACT

This document is the final report to the Air Force Office of Scientific Research on work performed under contract F49620-88-C-0048. It covers the period between January 1, 1988 and December 31, 1990. The project's primary objectives were to model hydrocarbon assisted boron combustion for air-breathing systems and apply gradient sensitivity analysis to determine key reaction pathways and critical uncertainties in thermochemical and kinetic parameters.

This report presents kinetic models for the chemically facilitated gasification of the ubiquitous boron oxide coating that inhibits particulate boron ignition and the second stage high temperature boron surface burning that occurs once the oxide coating has been removed. These models include a homogeneous gas phase oxidation mechanism consisting of 19 chemical species and 58 forward and reverse elementary reactions, multicomponent gas phase diffusion and heterogeneous reactions between gas phase oxidation products and the boron oxide/boron surface. Kinetic mechanisms are formulated to describe the heterogeneous surface reactions for both $B_2O_3(l)$ and $B(s)$ surfaces in terms of simple adsorption and desorption reaction steps. Thermochemical parameters for these reaction steps are estimated from the current heats of formation and gas phase bond energies for the major reactants. Reaction rate parameters are estimated from available experimental data or using elementary transition state theory arguments.

The kinetic processes are treated using a generalized kinetics computer code, with embedded gradient sensitivity analysis, for chemically reacting flows. This code was developed to provide a quantitative model for the nonsteady-state combustion of a one-dimensional (particle radius) spherical particle. This code uses a non-linear, implicit partial differential equation solver with fully automatic time step/node control that is compatible with formal gradient sensitivity analysis techniques.

TABLE OF CONTENTS

<u>Section</u>		<u>Page</u>
	ABSTRACT.....	
1	INTRODUCTION.....	1-1
	1.1 Statement of Problems and Research Objectives.....	1-1
	1.2 Program Scope.....	1-3
	1.3 Program Overview.....	1-3
	1.4 Report Outline.....	1-8
	1.5 References for Section 1.0.....	1-9
2	ONE DIMENSIONAL SPHERICAL BORON PARTICLE MODEL.....	2-1
	2.1 Governing Equations for the Gas Phase.....	2-1
	2.2 Governing Equations for the Condensed Phase.....	2-6
	2.3 Governing Equations for the Surface Species.....	2-7
	2.4 Initial, Boundary, and Interface Conditions.....	2-7
	2.5 Numerical Methods.....	2-9
	2.5.1 Temporal Intergration.....	2-9
	2.5.2 Spatial Discretization.....	2-11
	2.5.3 M-FEM Formulation.....	2-14
	2.5.4 Nodel Equations.....	2-16
	2.5.5 Solution Procedure.....	2-22
	2.6 Sensitivity Analysis.....	2-23
	2.6.1 Description of Sensitivity Coefficients.....	2-24
	2.6.2 Calculation of Sensitivity Coeffecients.....	2-26
	2.7 References for Section 2.0.....	2-28
3	HETEROGENEOUS SURFACE REACTION MECHANISMS.....	3-1
	3.1 Overview.....	3-1
	3.2 Gas Phase Boron Speciation and Thermodynamics.....	3-3
	3.2.1 Gas Phase Reactants, Heats of Formation and Entropies.....	3-3
	3.2.2 Gas Phase Bond Energies.....	3-5
	3.3 Definition of Elementary Reactions.....	3-5
	3.3.1 Adsorption Reactions.....	3-7
	3.3.2 First Order Desorption Reactions.....	3-8
	3.3.3 Second Order Reactions.....	3-9

TABLE OF CONTENTS (Continued)

<u>Section</u>		<u>Page</u>
3.4	Boron Oxide Surface Reactions.....	3-10
3.4.1	Global Reactions.....	3-10
3.4.2	Oxide Structure.....	3-11
3.4.3	Adsorption Thermodynamics and Kinetics.....	3-14
3.4.4	Desorption Reactions.....	3-15
3.5	Boron Particle Surface Reactions.....	3-17
3.5.1	Global Reactions.....	3-18
3.5.2	Experimental Rate Data.....	3-18
3.5.3	Kinetic Model.....	3-22
3.6	References for Section 3.0.....	3-26
4	MODEL RESULTS.....	4-1
4.1	B ₂ O ₃ Gasification.....	4-1
4.2	High Temperature B(s) Surface Oxidation.....	4-18
4.3	References for Section 4.0.....	4-24

LIST OF ILLUSTRATIONS

<u>Figure</u>		<u>Page</u>
1.1	Combustion of a Single Boron Particle in Chemically Reactive Environments.....	1-4
1.2	Simplified Boron Particle Combustion Model.....	1-6
3.1	(a) One proposed structure of vitreous B_2O_3 consisting of boroxy rings interconnected by BO_3 units. (b) Surface structural unit used in the kinetic model to describe surface adsorption and desorption reaction steps.....	3-13
4.1	Temporal variation of the $B_2O_3(l)$ gasification rate and percent surface coverage by adsorption products for a 50 μm particle at an ambient temperature of 1800 K.....	4-2
4.2	Calculated $B_2O_3(l)$ gasification rates due to surface reactions and physical evaporation as a function of particle diameter at ambient temperatures of (a) 1600 K and (b) 1800 K.....	4-4
4.3	Calculated $B_2O_3(l)$ gasification rates due to surface reactions and physical evaporation as a function of particle diameter at ambient temperatures of (a) 2000 K and (b) 2200 K.....	4-5
4.4	Calculated overall $B_2O_3(l)$ gasification rates as a function of particle diameter at ambient temperatures of 1600 K, 1800 K, 2000 K, and 2200 K.....	4-7
4.5	Radial species mass fraction and temperature profiles for an ambient temperature of 1800 K and droplet diameters of (a) 50 μm , and (b) 500 μm	4-8

LIST OF ILLUSTRATIONS (Continued)

<u>Figure</u>		<u>Page</u>
4.6	Adsorption fluxes as a function of droplet diameter for ambient temperatures of (a) 1600 K, (b) 1800 K, (c) 2000 K and (d) 2200 K.....	4-10
4.7	Desorption fluxes as a function of droplet diameter for ambient temperatures of (a) 1600 K, (b) 1800 K, (c) 2000 K and (d) 2200 K.....	4-12
4.8	Surface reaction flux as a function of droplet diameter for ambient temperatures of (a) 1600 K, (b) 1800 K, (c) 2000 K and (d) 2200 K.....	4-14
4.9	Percentage surface coverage as a function of droplet diameter for ambient temperatures of (a) 1600 K, (b) 1800 K, (c) 2000 K and (d) 2200 K.....	4-16
4.10	Sensitivity coefficients profiles as a function of droplet diameter for an ambient temperatures of 1800 K.....	4-18
4.11	Calculated B(s) burning rate constant for an ambient temperature of 1400 K and 2000 K.....	4-19
4.12	Particulate boron oxidation temperature profiles for an ambient temperature of (a) 1400 K and (b) 1500 K.....	4-21
4.13	Species mass fraction radial profiles for the oxidation of a 200 μm spherical boron particle in a JP4/air mixture at an ambient temperature of 1400 K.....	4-22
4.14	Species mass fraction radial profiles for the oxidation of a 200 μm spherical boron particle in a JP4/air mixture at an ambient temperature of 2000 K.....	4-23

LIST OF TABLES

<u>Table</u>	<u>Page</u>
1 $\Delta H_f,298$ and S_{298} for Primary Gas Phase Speciation.....	3-4
2 Gas Phase Bond Energies.....	3-6
3 Boron Oxide Surface: Global Reactions	3-11
4 Boron Oxide Surface: Adsorption Reactions.....	3-15
5 Boron Oxide Surface: First Order Desorption Reactions.....	3-16
6 Boron Surface: Global Reactions.....	3-19
7 B_{12}^+ Cluster Reaction Product Channels.....	3-20
8 Boron Surface: Adsorption Reaction.....	3-24
9 Boron Surface: First Order Desorption Reactions.....	3-25
10 Boron Surface: Second Order Reactions.....	3-26
13 The Ambient Mixture Compositions in Mole Fractions Obtained from Equilibrium Calculation of a JP-4/Air Mixture with an Equivalence Ratio of 0.5.....	4-1

1.0 INTRODUCTION

1.1 Statement of Problem and Research Objectives

For several decades elemental boron has long been proposed as an advanced fuel for combustion and propulsion systems because of its high energy density.^{1-1,1-2} Based on the heats of combustion, the gravimetric heating value of elemental boron is approximately 35% greater than JP4, a widely used conventional liquid hydrocarbon fuel, and approximately 85% greater than metallic aluminum, another advanced fuel candidate currently used in solid fueled rockets. On a volumetric basis, boron is even more appealing with a heating value approximately 300% greater than JP4 and 60% greater than aluminum. These potential advantages have sparked a great deal of interest in the enhancement of conventional liquid hydrocarbon combustion via the addition of particulate boron in the form of slurry suspensions. For air-breathing systems, however, the theoretical potential has not been fully realized in either research or practical combustors.¹⁻³

Two major unresolved combustion problems are the poor combustion efficiency and inadequate ignition characteristics of boron particles.¹⁻³ To achieve the full theoretical performance of boron combustion, boron particles must ignite and completely burn (i.e. reach final products of gaseous H₂O, gaseous CO₂ and liquid boria B₂O₃) within a very limited residence time (2 - 10 ms). The poor combustion efficiency results from slow kinetically controlled condensation processes to form the liquid phase metal oxide which do not reach the desired equilibria during the short residence times available in most combustion devices. The ignition problem results from the formation of an oxide coating on unburned boron fuel particles which inhibits boron surface oxidation and vaporization during the initial heat-up phase of the particle.

Finding adequate solutions to these practical problems has been hindered by the absence of a fundamental understanding of the combustion processes. The current understanding of boron combustion consists of, at best, an overall description of the most probable physical and chemical processes; i.e. knowledge of elementary processes and parameters is significantly lacking. It is apparent from previous combustion research, that if solutions to the current problems preventing practical application of boron combustion are to be found, additional research will be required, particularly at the elementary level.

Recognition of the research needed to help resolve the practical difficulties associated with boron combustion has motivated several on-going research efforts designed to obtain a better understanding of the combustion process at the molecular level. These include experimental studies of small boron cluster structure, stability and reactivity,¹⁻⁴⁻¹⁻⁷ detailed chemical kinetic combustion modeling,¹⁻⁸⁻¹⁻¹⁵ flow reactor rate measurements for bulk boron oxidation and gasification by O(g), CO₂(g), B₂O₃(g) and H₂O(g)¹⁻¹⁶⁻¹⁻²¹ and boron surface structure and reactivity studies.^{1-22,1-23}

As part of this ongoing research effort, the objective of the present program was to construct a detailed model for particulate boron assisted hydrocarbon combustion. The goal of the program was to obtain a better fundamental understanding of the elementary processes and the role these processes play during the entire combustion process. Since the long range success of this program would be dependent on the ability to obtain the necessary data for input to such a model, the program was designed to be closely coordinated with concurrent experimental work by other groups. In addition, the program relied on gradient sensitivity analysis techniques^{1-24,1-25} to aid the development and validation of the model and to efficiently interface modeling and experimental programs.

1.2 Program Scope

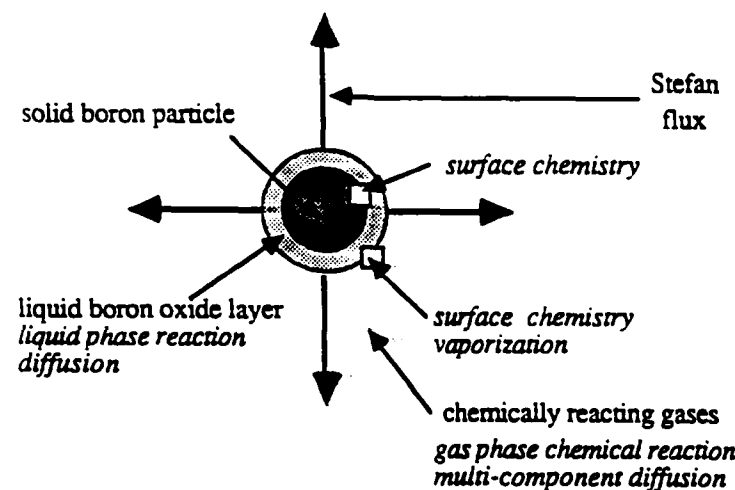
Boron-assisted hydrocarbon combustion is complex process which includes a heterogeneous (solid/gas and solid/liquid) ignition, volatilization and oxidation phase, a homogeneous (gas/gas) oxidation phase, and a heterogeneous (gas/liquid) condensation phase as combustion products cool.¹⁻³ In earlier work, the homogeneous boron combustion phase was modeled and gradient sensitivity analysis was used to determine key reaction pathways and critical uncertainties in thermodynamic and kinetic parameters.^{1-11,1-12} The primary goal of the current research was to develop a combustion model for the initial heterogeneous ignition, volatilization and oxidation phase of boron combustion and to couple that model to the homogeneous oxidation model developed earlier. As in the previous work, gradient sensitivity analysis techniques^{1-24,1-25} were used to identify key reaction mechanisms and critical uncertainties in molecular thermodynamic and kinetic parameters.

1.3 Program Overview

Experimental observations indicate that the combustion of boron particles occurs in two stages. Macek,¹⁻²⁶ for example, observed that after heating to between 1800 K and 2000 K, the boron particle becomes luminous and glows for a short period of time, but may fade out as the boron particle is weighted with a molten boron oxide layer. If the ambient temperature is sufficiently high, then this initial ignition state is followed by second stage of burning which is much brighter and longer than the first stage. The second stage corresponds to the full-fledged combustion of a "clean" boron particle which occurs once the oxide coating has been removed by vaporization and heterogeneous surface reactions.

Figure 1.1 depicts schematically the two stages characterizing the combustion of a single boron particle in chemically reactive environments. As indicated in this figure, a detailed simulation of the combustion process

1. Ignition Stage



2. Combustion Stage

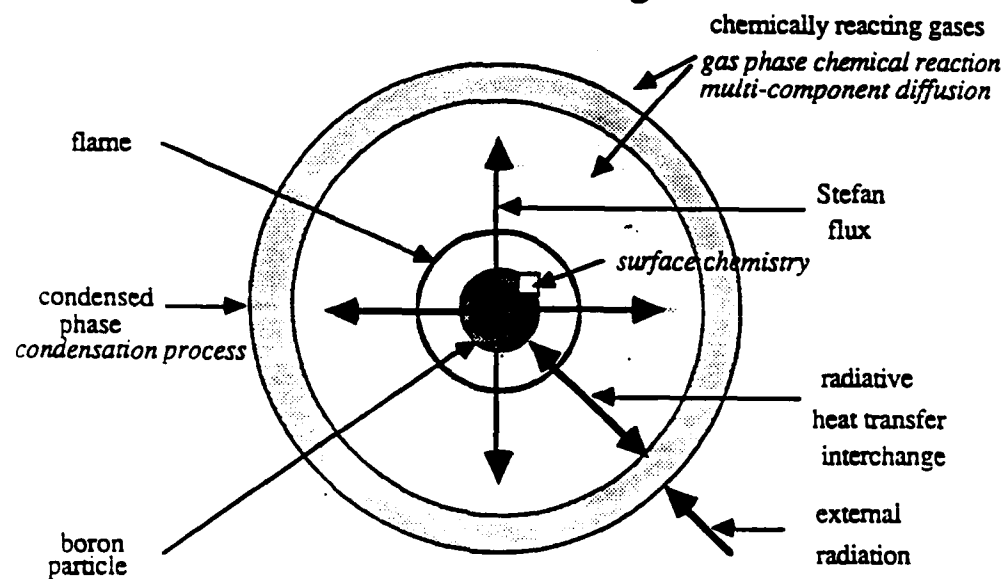


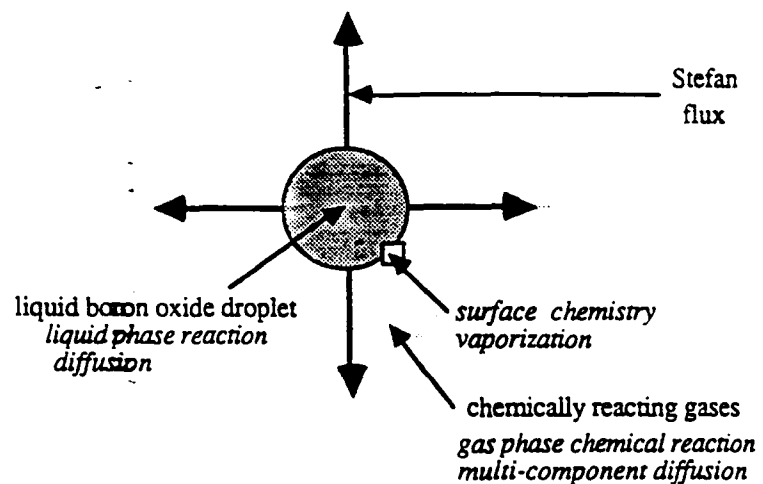
Figure 1.1. Combustion of a Single Boron Particle in Chemically Reactive Environments

requires homogeneous gas phase oxidation reactions and multicomponent gas phase diffusion to the particle surface, heterogeneous surface reactions between gas phase species and the oxide (stage 1) or solid boron (stage 2) surface, liquid oxide phase diffusion and chemistry, heterogeneous reactions at the boron oxide-solid boron interface, Stefan flux from the particle surface and radiative heat transfer.

Modeling the full combustion process is clearly an inherently formidable task. Consequently, the approach of the current program was to develop a complete combustion model in successive stages which would progressively build on each other by incorporating additional important processes. Each distinct stage was designed to focus on key issues concerning the combustion process and was iteratively upgraded to reflect comparisons with phenomenological observations and new experimental or theoretical measurements of thermochemical and kinetic parameters.

Accordingly, a simplified description of boron combustion was formulated which focused on the gasification of molten boron oxide layer and the second stage, high temperature surface burning of a solid boron particle. A schematic presentation of these sub-models is shown in Figure 1.2. The liquid oxide droplet model is a first-order representative of that phase of boron combustion when the boron particle is coated with an appreciable oxide layer. The oxide layer is removed at the surface through vaporization. However, at high temperatures the gasification process can involve chemical transformations. Several earlier investigations^{1-3,1-27} have indicated that water, for example, can promote ignition. Similarly, because of its low volatility, gasification of particulate boron involves chemical transformation at the surface into more volatile suboxides and suboxyhydrides. Thus, one key objective of this submodel was to reliably predict the heterogeneous kinetic mechanisms by which surrounding gases significantly affect the rates of boron and boron oxide gasification evaporation.

1. Chemically Facilitated Vaporization of a Liquid Boron Oxide Droplet



2. Combustion of a Boron Particle with Clean Surface

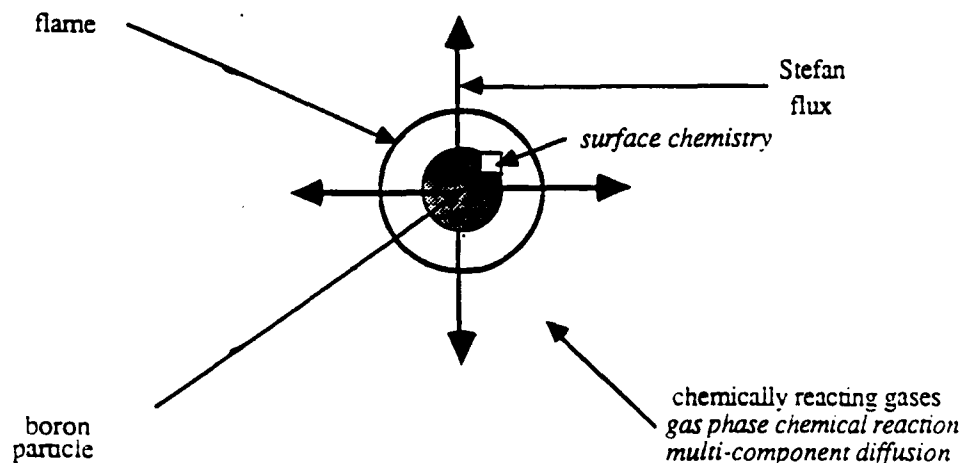


Figure 1.2. Simplified Boron Particle Combustion Model

During the first year of this program, the two submodels depicted in Figure 1.2 were treated using the continuously stirred reactor model (CSRM).¹⁻¹³ This is a steady-state model in which spatial degrees-of-freedom are eliminated by assuming a thin control volume perpendicular to the flow direction which is well mixed so that species profiles are uniform. The goal of that work was to upgrade the homogeneous gas phase oxidation model by incorporating heat and mass transport. Mass transport was treated by both (1) parameterizing the mass fluxes by the residence time and (2) using molar production rates for heterogeneous surface reactions. The results of that analysis were presented in the first annual report and will not be reproduced here.¹⁻¹³ The principle result, however, was that the kinetic calculations, coupled with sensitivity analysis, indicated that the reactions identified previously^{1-11,1-12} as being important in the homogeneous oxidation model for a closed system remain the dominant mechanisms when heat and mass fluxes are included.

During the second year, the CCRM was superseded with a detailed one-dimensional, time dependent spherical particle combustion model and the associated computer codes which include the capability to compute sensitivity coefficients were completed.¹⁻¹⁴ This model represents state-of-the-art modeling technology and marks a significant achievement in the proposed goals of this project. The spherical particle model can describe particle shrinkage, density changes, Soret effects and radiative heat transfer. In addition, the ability to treat surface speciation and elementary absorption and desorption reactions represents an unsurpassed level of detail in modeling such complex systems. As in earlier work, gradient sensitivity analysis techniques were incorporated into the computer codes to facilitate the identification of key mechanisms and system parameters, as well as to provide an internal mechanism to aid in evaluating the validity and self-consistency of the model input parameters. This extension of gradient sensitivity analysis techniques to heterogeneous processes such as particle ignition was

not only critical to the successful treatment of boron combustion, but will be a major contribution to models of other inherently heterogeneous chemical systems.

During the third year, the most potentially important heterogeneous surface reactions were identified, first-order formulations of the reaction mechanisms were developed and thermochemical and reaction rate parameters were estimated. These surface reaction mechanisms include adsorption and desorption processes and, therefore, differ considerably from earlier modeling work in their level of microscopic detail. This was motivated by the desire to ultimately provide a more realistic model of boron combustion which, for example, would provide a description of surface speciation and a more accurate dependence of reaction rates on species concentration. Thus, while the proposed mechanisms are presently very speculative because of the lack of detailed experimental or theoretical data for elementary processes, they provide the needed first step in developing an accurate combustion model. In addition, the detailed level of description complements concurrent experimental studies on small boron clusters¹⁻⁴⁻¹⁻⁷ by Anderson's group at Stony Brook and boron surface structure and reactivity^{1-22,1-23} by Trenary's group at Chicago. Thus, the reaction mechanisms presented in this report should be viewed as an initial formulation which can be modified and iteratively upgraded as new experimental data becomes available.

1.4 Report Outline

Section 2.0 presents the mathematical formulation of the combustion process. This includes the governing equations for mass and energy conservation, as well as a description of the numerical techniques used to solve these equations. The formalism and computational methods for applying gradient sensitivity analysis techniques to heterogeneous processes with spatial and temporal dependence are also presented in Section 2.0. Heterogeneous surface reactions, reaction mechanisms and estimates of

thermochemical and parameters are presented in Section 3.0. Section 4.0 presents model results for boron oxide gasification and particulate boron surface burning in hydrocarbon combustion environments.

1.5 References for Section 1.0

- 1-1 Brudette, G.W., Lander, H.R. and McCoy, J.R., "High Density Fuels for Cruise Missiles," AIAA, 78-267, 1978.
- 1-2 Anon, "State-of-the-art Review of Boron Fuel Technology," Aero. Propulsion Laboratory, Wright-Patterson Air Force Base, 1980.
- 1-3 Faeth, G.M., "Status of Boron Combustion Research," Report of the Boron Combustion Specialists Workshop, Air Force Office of Scientific Research, October 1984, also partially published under the same title in the Proceedings of the 21st JANNAF Combustion Meeting, Laurel, MD, October 1984.
- 1-4 Hanley, L., Whitten, J.L. and Anderson, S.L., "Collision-Induced Dissociation and ab Initio Studies of Boron Cluster Ions: Determination of Structures and Stabilities," J. Phys. Chem. 92, 5803 (1988).
- 1-5 Hanley, L. and Anderson, S.L., "Oxidation of Small Boron Clusters Ions (B_{1-13}^+) by Oxygen," J. Chem. Phys. 89, 2848 (1988).
- 1-6 Ruatta, S.A., Hanley, L. and Anderson, S.L., "Dynamics of Boron Cluster Ion Reactions with Deuterium: Adduct Formation and Decay," J. Chem. Phys. 91, 226 (1989).
- 1-7 Hintz, P.A., Ruatta, S.A. and Anderson, S.L., "Interaction of Boron Cluster Ions with Water: Single Collision Dynamics and Sequential Etching," J. Chem. Phys. 92, 292 (1990).
- 1-8 King, M.K., "Ignition and Combustion of Boron Particles and Clouds," J. Spacecraft and Rockets 19, 294 (1982).
- 1-9 King, M.K., "Single Particle Boron Ignition Modeling," 19th JANNAF Combustion Meeting, Volume II., pg. 27, October 1982.
- 1-10 Glassman, I., Williams, F.A. and Antaki, P., "A Physical and Chemical Interpretation of Boron Particle Combustion," 20th Symposium (International) on Combustion, 2057 (1984).

1-11 Yetter, R.A., Cho, S.Y., Rabitz, H., Dryer, F.L., Brown, R.C. and Kolb, C.E., "Chemical Kinetic Modeling and Sensitivity Analyses for Boron Assisted Hydrocarbon Combustion," Twenty-Second Symposium (International) on Combustion, p. 919, The Combustion Institute (1988).

1-12 Yetter, R.A., Rabitz, H., Dryer, F.L., Brown, R.C. and Kolb, C.E., "Kinetics of High Temperature B/O/H/C/ Chemistry," Combustion and Flame 83, 43 (1991).

1-13 Brown, R.C., Annen, K.D., Kolb, C.E., Cho, S.Y., Yetter, R.A., Dryer, F.L., and Rabitz, H., "First Annual Report on Boron Combustion Model Development with Kinetic Sensitivity Analysis," Aerodyne Research, Inc. Report No. ARI-RR-703, May 1989.

1-14 Brown, R.C., Annen, K.D., Kolb, C.E., Cho, S.Y., Yetter, R.A., Dryer, F.L., and Rabitz, H., "Second Annual Report on Boron Combustion Model Development with Kinetic Sensitivity Analysis," Aerodyne Research, Inc. Report No. ARI-RR-764, February 1990.

1-15 Brown, R.C., Kolb, C.E., Rabitz, H., Cho, S.Y., Yetter, R.A. and Dryer F.L., "Kinetic Model for Liquid B_2O_3 Gasification in a Hydrocarbon Combustion Environment: I. Heterogeneous Surface Reactions," accepted for publication in the International Journal of Kinetics, December 1990.

1-16 Rosner, D.E. and Allendorf, H.D., "Kinetic Studies of the Attack of Refractory Materials by Oxygen Atoms and Chlorine Atoms," Proc. 3rd Int. Symp. on High Temp. Tech., 707, Butterworths, London (1969).

1-17 Gomez, A., Zvuloni, R. and Rosner, D.E., "Flow Reactor Studies of Boron Vaporization and Kinetically-Controlled Oxidation Using Microwave-Induced Plasma Emission Spectroscopy: Preliminary Results," presented at the 1986 Technical Meeting. The Combustion Institute Eastern States Section, Dec. 12, 1986, San Juan, Puerto Rico, and at the Joint Meeting of the French and Italian Section of the Combustion Institute, June 16, 1987, Amalfi, Italy.

1-18 Zvuloni, R., Gomez, A. and Rosner, D.E., "Direct Measurements of the High Temperature Kinetics of Solid Boron Gasification by Its Higher Oxide $B_2O_3(g)$: Chemical Propulsion Implications," J. Propulsion and Power, in press (1989).

1-19 Zvuloni, R. and Rosner, D.E., "High Temperature Gasification Rate of Solid Boron In Mixtures of its Highest Oxide $B_2O_3(g)$, and Water Vapor," AIAA J. Propulsion and Power, Submitted 1989.

1-20 Zvuloni, R. and Rosner, D.E., "High Temperature Kinetics of Solid Boron Gasification by its Higher Oxide $B_2O_3(g)$; Flow Reactor Technique, Rate Measurements and Their Implications," *J. Phys. Chem.*, submitted, 1989.

1-21 Zvuloni, R. "Flow Reactor Studies of High Temperature Gasification Kinetics of Solid Boron and Carbon and Their Chemical Propulsion Implications," Ph.D. Dissertation, Yale University of Chemical Engineering, May 1990.

1-22 Trenary, M., "The Structure and Reactivity of Boron Surfaces," AFOSR Annual Technical Report, University of Illinois at Chicago (January 1989).

1-23 Trenary, M., "The Structure and Reactivity of Boron Surfaces," Second Annual Technical Report, AFOSR-88-0111, (January 1990).

1-24 Rabitz, H., "Sensitivity Analysis of Combustion Systems," in *The Mathematics of Combustion*, J. Buckmaster, Ed., SIAM, Philadelphia (1985).

1-25 Rabitz, H., "On Determining Important Aspects of Combustion Kinetics Modeling with Sensitivity Analysis," Lectures in Applied Mathematics 24, 499 (1986).

1-26 Macek, A., "Combustion of Boron Particles at Atmospheric Pressure," *Combustion Science and Technology* 1, 181 (1969).

1-27 Turns, S.R., Holl, J.T., Solomon, A.S.P. and Faeth, G.M., "Gasification of Boron Oxide Drops in Combustion Gases," *Combust. Sci. and Tech.* 43, 287 (1985).

2.0 ONE DIMENSIONAL SPHERICAL PARTICLE COMBUSTION MODEL

This section describes the mathematical formulation of a one-dimensional, nonsteady-state model for the combustion of a spherical particle. Sections 2.1 - 2.3 present mass, species and energy conservation equations and Section 2.4 specifies the appropriate boundary conditions. In Section 2.5, the numerical methods used to solve these strongly coupled partial differential equations (PDE) are discussed and qualitatively compared with other frequently used numerical techniques. The application of sensitivity analysis techniques to problems in which system variables and parameters are both temporally and spatially dependent is discussed in Section 2.6 and includes a description of the computational method used to calculate sensitivity coefficients.

2.1 Governing Equations for the Gas Phase

The governing equations for overall mass, species, and energy conservation in the gas phase are

$$\frac{\partial \rho_g}{\partial t} + \frac{1}{r^{a-1}} \frac{\partial}{\partial r} (r^{a-1} \rho_g v_r) = 0 \quad (2-1)$$

$$\rho_g \frac{\partial Y_{g,i}}{\partial t} + \rho_g v_r \frac{\partial Y_{g,i}}{\partial r} = - \frac{1}{r^{a-1}} \frac{\partial (r^{a-1} \rho_g Y_{g,i} v_r)}{\partial r} + R_{g,i} \quad (2-2)$$

$$\rho_g \bar{C}_{p,g} \frac{\partial T_g}{\partial t} + \rho_g \bar{C}_{p,g} v_r \frac{\partial T_g}{\partial r} = \frac{1}{r^{a-1}} \frac{\partial}{\partial r} (r^{a-1} \lambda_g \frac{\partial T_g}{\partial r}) - \sum_{i=1}^{i=n} (Y_{g,i} v_{r,i} C_{p,g,i}) \frac{\partial T_g}{\partial r} - \sum_{i=1}^{i=n} R_{g,i} H_{g,i} \quad (2-3)$$

where "a" represents a geometrical factor ($a = 0$ for cartesian coordinates, $a = 1$ for cylindrical coordinates, and $a = 2$ for spherical coordinates). ρ_g denotes the density of the gas mixture, $\bar{C}_{p,g}$ the specific heat capacity of the gas mixture at constant pressure, λ_g the thermal conductivity of the gas mixture, $Y_{g,i}$ the mass fraction of the i^{th} species in the gas phase, T_g the temperature of the gas mixture, $C_{p,g,i}$ the specific heat capacity of the i^{th} gas phase species, $H_{g,i}$ the specific enthalpy of the i^{th} species with respect to the mixture of remaining species, $v_{r,i}$ the diffusion velocity of the i^{th} species, v_r the fluid velocity in the radial direction, r the radial coordinate, and $R_{g,i}$ the mass production rate of the i^{th} species by gas phase chemical reaction. The ideal gas equation of state relates $Y_{g,i}$, ρ_g and T_g by

$$P = \rho_g R^0 T_g \sum_{i=1}^{i=n} \frac{Y_{g,i}}{W_i} \quad (2-4)$$

where P is the thermodynamic pressure, R^0 the universal gas constant, and W_i the molecular weight of the i^{th} species.

The transport model recommended by Coffee and Heimerl²⁻¹ is used to describe multi-component diffusion processes. According to Coffee and Heimerl²⁻¹ the diffusive flux is described by

$$v_i = d_{r,i} + d_{t,i} + d_c \quad (2-5)$$

where $d_{r,i}$ is the ordinary diffusion velocity, $d_{t,i}$ is the thermal diffusion velocity, and d_c is the constant diffusion velocity. The ordinary diffusion coefficient can be conveniently calculated by using an effective binary diffusivity D_i as follows,

$$d_{r,i} = - \frac{D_i}{X_i} \frac{\partial X_{g,i}}{\partial r} \quad (2-6)$$

where $X_{g,i}$ is the mole fraction of the i^{th} species in the gas phase and D_i is dependent on radial position. In order to generalize the binary diffusion formulas and mass transfer correlations by simply using the D_i , it is assumed (Curtiss - Hirshfelder approximation) that all but the i^{th} species move with the same velocity. Then the D_i can be related to the binary diffusion coefficients D_{if} through the following relation.

$$D_i = - \frac{\sum_j \frac{X_{g,i}}{D_{ij}}}{1 - \sum_j \frac{Y_{g,i}}{D_{ij}}} \quad (2-7)$$

The thermal diffusion velocity, $d_{t,i}$, is obtained by employing the thermal diffusion ratio (tD_i).

$$d_{t,i} = \frac{D_i t_{Di}}{X_{g,i}} \frac{1}{T_g} \frac{\partial T_g}{\partial r} \quad (2-8)$$

The constant diffusion velocity, d_c , is introduced to assure the zero net diffusive flux.

$$d_c = - \sum_{j=1}^{j=n} Y_j (d_{r,j} + d_{t,j}) \quad (2-9)$$

The transport coefficients are calculated by using the Transport Package developed by Kee et al.,²⁻² which evaluates gas phase conductivities and diffusion coefficients from the Lennard-Jones potential, the well depth, the collision diameter, the dipole moment, the polarizability, and the rotational relaxation collision number.

The inner boundary located at the droplet surface moves as the droplet surface regresses. Thus, a density weighted coordinate transformation is introduced to immobilize the regressing interface location. Specifically, defining ϕ by

$$\phi = \int_{r_p}^r r'^{a-1} \rho_g(r', t) dr' \quad (2-10)$$

then

$$\frac{\partial \phi}{\partial r} = r^{a-1} \rho_g(r, t) \quad (2-11)$$

and

$$\frac{\partial \phi}{\partial t} = - r^{a-1} \rho_g v_r + m_p \quad (2-12)$$

where

$$m_p = r^{a-1} \rho_g v_r \left(1 - \frac{\rho_g}{\rho_c}\right) \quad r=r_p \quad (2-13)$$

The gas phase density (ρ_g) is usually much smaller than the condensed phase density (ρ_c), i.e. $\rho_g \ll \rho_c$, except in the critical conditions, such that the m_p becomes identical to the mass flow rate. The following relationships derived from the chain rule are used to perform the coordinate transformation:

$$\frac{\partial}{\partial r} = \frac{\partial \phi}{\partial r} \frac{\partial}{\partial \phi} = r^{a-1} \rho_g \frac{\partial}{\partial \phi} \quad (2-14)$$

$$\frac{\partial}{\partial t} = \frac{\partial \phi}{\partial t} \frac{\partial}{\partial \phi} + \frac{\partial}{\partial t} = (m_p - r^{a-1} \rho_g v_r) \frac{\partial}{\partial \phi} + \frac{\partial}{\partial t} \quad (2-15)$$

The continuity equation, Equation (2-1), is automatically satisfied in the new coordinate system. Using Equations (2-14) and (2-15), the species and energy conservation equations, Equations (2-2) and (2-3), become

$$\frac{\partial Y_{g,i}}{\partial t} + m_p \frac{\partial Y_{g,i}}{\partial \phi} = - \frac{\partial (r^{a-1} \rho_g Y_{g,i} v_{r,i})}{\partial \phi} + \frac{R_{g,i}}{\rho_g} \quad (2-16)$$

$$\bar{C}_{pg} \frac{\partial T_g}{\partial t} + m_p \bar{C}_{pg} \frac{\partial T_g}{\partial \phi} = \frac{\partial}{\partial \phi} (r^2(a-1) \rho_g \lambda_g \frac{\partial T_g}{\partial \phi}) -$$

$$r^{a-1} \rho_g \sum_{i=1}^{i=n} (Y_{g,i} v_{r,i} C_{p,g,i}) \frac{\partial T}{\partial \phi} - \frac{\sum_{i=1}^{i=n} R_{g,i} H_{g,i}}{\rho_g} \quad (2-17)$$

2.2 Governing Equations for the Condensed Phase

The size of the condensed phase (oxide droplet or boron particle) is continuously decreasing with time as combustion or vaporization proceeds. The overall mass conservation condition determines the rate of change of the particle diameter by

$$\frac{\partial r_p}{\partial t} = \frac{\rho_g}{\rho_c} v_r \text{ at } r = r_p \quad (2-18)$$

where ρ_c is the particle density. The energy conservation equation becomes

$$\rho_c C_{p,c} \frac{\partial T_c}{\partial t} = \frac{1}{r^{a-1}} \frac{\partial}{\partial r} (\lambda_c r^{a-1} \frac{\partial T_c}{\partial r}) \quad (2-19)$$

where the subscript c denotes the condensed phase, r_p the particle radius, $C_{p,c}$ the specific heat capacity and λ_c the thermal conductivity.

$$\rho_c C_{p,c} \frac{\partial T_c}{\partial t} = \frac{1}{r_p^{a-1} \eta^{a-1}} \frac{\partial}{\partial \eta} (\lambda_c \eta^{a-1} \frac{\partial T_c}{\partial \eta}) - \rho_c C_{p,c} \frac{\partial \eta}{\partial t} \frac{\partial T_c}{\partial \eta} \quad (2-20)$$

2.3 Governing Equations for the Surface Species

In the present surface chemistry model, chemical reactions among surface species or between surface species and gaseous species are not considered. Therefore, the governing equations for the surface species can be written as

$$\frac{d r_p^2 C_{s,i}}{dt} = r_p^2 R_{s,i} \quad (2-21)$$

$k=ns$

$$R_{s,i} = \sum_{k=1}^n v'_{a,i,k} k_{a,k} C_{g,k} - k_{d,i} C_{s,i} \quad (2-22)$$

where $v'_{a,i,k}$ denotes the stoichiometric coefficient for species i appearing as a adsorption product of species k , $k_{a,k}$ the adsorption rate constant for gaseous species k , $k_{d,i}$ the desorption rate constant for surface species i , $C_{s,i}$ the concentration of surface species i .

2.4 Initial, Boundary, and Interface Conditions

In order to solve the governing equations described above, the attending initial, boundary, and interface conditions should be specified. Initial conditions specifies the species concentration and ambient and particle temperatures at $t = 0$, i.e.

$$Y_{g,i}(0, r) = Y_{g,io}(r) \quad r_p < r < \infty \quad (2-23)$$

$$T_g(0, r) = T_{g,o}(r) \quad r_p < r < \infty \quad (2-24)$$

$$T_c(0, r) = T_{c,o}(r) \quad 0 < r < r_p \quad (2-25)$$

The boundary conditions at the left hand side, which is positioned at the center of the condensed phase, are based on no flux conditions for both chemical species and temperature of the condensed phase. Thus, at $r = 0$

$$\frac{\partial T}{\partial r} = 0 \quad (2-26)$$

The boundary conditions at the right hand side are assumed to be same as the ambient conditions so that at $r = \infty$

$$Y_g = Y_{g,\infty} \quad (2-27)$$

$$T_{g,i} = T_{g,i\infty} \quad (2-28)$$

The temperature profile is continuous across the interface,

$$\text{at } r = r_p, \quad T_g = T_s \quad . \quad (2-29)$$

The interface conditions at the surface of the condensed phase are determined by considering the mass balance across the boundary; the chemical species flux at the surface is same as the amount destroyed or produced by the surface chemical reactions

$$R_{s,i} = \rho_g Y_{g,i} (v_r + v_{r,i}) \quad (2-30)$$

Summing the above equations over chemical species and using the fact that summation of diffuse fluxes should be equal to zero, the mass flux ($\rho_g v_r$) at the surface can be written,

$$\rho_g v_r]_{r=r_p} = \sum_{i=1}^{i=N} R_{s,i} \quad (2-31)$$

Similarly, the energy balance across the interface yields

$$(\lambda_g \frac{\partial T}{\partial r})_g = \sum_{i=1}^{i=n} R_{s,i} + (\lambda_s \frac{\partial T}{\partial r})_s \quad (2-32)$$

2.5 Numerical Methods

In Sections 2.1 thru 2.4, the vaporization and combustion of isolated droplets are treated as an initial boundary value problem in which governing parabolic PDEs are strongly coupled due to strong chemical interactions. General solution procedures for initial boundary value problems are, first, to discretize the spatial part of the differential equations and, then, to integrate the resulting system of ordinary differential equations over time.

2.5.1 Temporal Integration

Widely used numerical techniques for temporal integration in chemically reactive flow problems include time splitting techniques,²⁻³ semi-implicit

methods,^{2-4,2-5} Newton linearization techniques, and Gear type non-linear iterations.²⁻⁶

A high computational efficiency may be achieved by using the time splitting technique in solving chemically reactive flow problems.²⁻⁷⁻²⁻¹⁰ The time splitting technique breaks complex interactions among processes into individual processes such that each individual process, especially chemical kinetics, can be solved separately. Therefore, the number of simultaneous equations to be solved can be dramatically reduced. For problems with disparate time scales among sub-processes, an efficient temporal integration is achieved by applying the appropriate time step according to the characteristic time scale of each sub-process. Thus, for chemically reactive flow problems in which chemical processes are much faster than transport processes, a small time step is applied to resolve chemistry equations, whereas transport equations can be integrated with a large time step. In addition, a high degree of parallelism can be achieved because chemistry equations at each grid point are decoupled and solved in parallel. This makes the time splitting techniques extremely favorable to the parallel super computer architectures such as the Connection Machine and the Massively Parallel processes.²⁻¹¹ However, numerical accuracy may be considerably degraded when solutions from individually splitted differential equations are combined to yield real solutions. Furthermore, as the system approaches extinction, the time scale of transport processes becomes comparable to or even smaller than that of chemical processes, and the interaction between transport and chemical processes become important. Thus, the time splitting technique which decouples these processes may not resolve the transition from quasi-steady burning to extinction accurately.

A Newton linearization technique²⁻¹²⁻²⁻¹³ or semi-implicit method²⁻¹³ may be applied to decouple highly non-linear equations appearing in chemically reactive flow problems. Numerical comparisons between these two techniques in solving transport/reaction equations were made by Yuk.²⁻¹⁴ These techniques

may not resolve numerical stiffness problems arising from chemical species with high reaction fluxes such as radicals. Because the chemical species with high reaction fluxes are very likely to be in the steady state, these numerical problems may be avoided by carefully applying the pseudo-steady state approximation to remove numerically stiff differential equations from the ODE systems. However, if used inappropriately, the steady state approximation may be a source of a significant error.

In the present study, Gear's implicit method²⁻⁶ is employed to integrate systems of stiff ODEs over time. Gear's method automatically controls the time step and the order of integration to maintain requisite levels of stability and accuracy in the time domain. Even though Gear's method yields accurate numerical solutions compared to the other techniques described above, it requires inversion of a large matrix, which is a computationally intensive operation. It is hoped that the numerical code developed here using Gear's method may be used to critically evaluate the code with a more computationally efficient temporal integrator such as the time splitting technique, the semi-implicit method, and the Newton linearization in solving chemically reactive flow problems.

2.5.2 Spatial Discretization

The governing PDEs given in Sections 2.1 thru 2.3 are spatially discretized by a Finite Element method. The particular Finite Element model used in this study employs a Galerkin formulation and linear basis functions. Unlike conventional Finite Difference methods, the flux boundary conditions are exactly incorporated into the Finite Element formulation without introducing any fictitious model nodal points or degrading the numerical accuracy. This allows accurate calculation of flux boundary conditions, which is very important especially in the present case because it leads to an accurate prediction of the particle gasification rate.

In chemically reactive flow problems including the vaporization and combustion of isolated particles, one or more steep fronts may appear/disappear or move continuously in the solution domain. The spatial stiffness may be resolved by increasing the order of basis functions in Orthogonal Collocation or Galerkin Finite Element formulations in the vicinity of the steep fronts. Even though further studies are required to evaluate this technique, our study shows that when Orthogonal Collocation Finite Element method is implemented with adaptively varying the degree of polynomial orders, numerical performance is very good in terms of reducing Gibbs overshooting/undershooting, numerical diffusion, and temporal stiffness due to close adjacent grid points. This technique is expected to perform as well with the Galerkin Finite Element method. However, the matrix structure becomes irregular, which causes difficulties in computer program coding and data allocation, and considerably increases the computational time.

The alternate approach, which is chosen in the present study, is to apply dense gridding in the vicinity of steep fronts. The node control is performed by various adaptive gridding techniques. Philosophically, adaptive gridding techniques widely used in chemically reactive flow problems are of two types. In the first method, adaptive gridding is based on a single fluid property or a single dependent variable behavior. This is implemented by

1. Moving nodes at mean fluid velocities or at some other characteristic velocity in a fluid, which is known as Lagrangian regridding procedures, or
2. Performing coordinate transformation to equally distribute gradients of important variables such as temperature.

In the combustion of isolated droplets, Lagrangian regridding procedures are inappropriate because neither a flame velocity nor a flame position is well defined. The coordinate transformation based on the equi-distribution of gradients of temperature was tried by the authors. Severe difficulties were found in obtaining convergence in the Newton-Raphson iteration of the non-linear initial value problem solver. This problem may be avoided by

applying a Newton linearization technique to perform temporal integration as shown by Dwyer and Sanders²⁻¹², but such a temporal integration is not acceptable in the present study as discussed in the previous section. The poor convergence in the non-linear initial value problem solver is probably because the coordinate transformation may increase stiffness or because the resulting grid system which is based only on the temperature profiles may not be good enough to resolve all the steep fronts in the model domain.

The second method considers more than one dependent variable to perform adaptive gridding. This is implemented by

1. Inserting or removing grid points to reduce local errors or equi-distribute mesh functions, or
2. Moving nodes smoothly at each time step to reduce global errors or equi-distribute mesh functions.

The former technique (1) is based on two step procedures; a solution step and adaptive gridding step, whereas in the latter technique (2), termed moving node technique, the node positions are computed together with the solution values at each node. Thus, node control is performed statically in the former technique (1), and dynamically in the latter technique (2). Adaptive gridding based on inserting or removing nodes can potentially solve partial differential equations to a prescribed level of accuracy, whereas moving node methods can follow evolving non-uniformities and very effectively reduce dispersive errors and Gibbs overshooting/undershooting. These adaptive gridding techniques are different from adaptive mesh refinement techniques,²⁻¹⁵⁻²⁻¹⁸ in which appropriately graded meshes are constructed from a coarse mesh through iterative procedures. In general, the adaptive gridding techniques discussed here may be more suitable for time dependent PDEs than the adaptive mesh refinement techniques because they modify the previous time step grid system slightly at each time step according to evolution of solutions.

Remarkable progresses have been made toward achieving adaptive gridding by inserting or removing grid points according to error estimates.²⁻¹⁹ This adaptive grid technique is implemented by adding or removing ODEs to the model and interpolating or projecting dependent variables to provide initial conditions for the added ODEs. Thus, dependent variable interpolation or projection must be well defined and performed accurately for maximum effectiveness. Whenever nodes are added or deleted, the initial value problem solver should be restarted, which is very costly for multi-step methods.

In the present study, moving node techniques were chosen to perform adaptive gridding. The moving node techniques move a fixed number of nodes smoothly at each time step to adjust nodes following evolution of solutions. No dependent variable transformation is involved, and nodes are not inserted or removed. Here, the moving node techniques are implemented onto the Galerkin Finite Element method to formulate a Moving node Finite Element Method (hereafter, M-FEM). For convenience, the conventional fixed node Galerkin Finite Element Method is termed the Fixed node Finite Element method (hereafter F-FEM). Unlike the F-FEM, the M-FEM should account for effects of node movements on dependent variables. The successful M-FEM formulation should be able to control nodes in a non-stiff manner, and prevent any abnormal behaviors such as node crossing. A detailed mathematical formulation is shown in the next section.

2.5.3 M-FEM Formulation

The mathematical derivations presented below are obtained by closely following Miller and Miller's²⁻²⁰ and Linch's²⁻²¹ work, in which more detailed discussions with rigorous mathematical justification are found.

In general, time dependent differential equation can be written as

$$u' = L(u) \quad t > 0 \quad (2-33)$$

where $L(u)$ is a non-linear partial differential operator. Because nodes are continuously deforming with time, the approximate solution, v , can be written in terms of both temporally varying node positions, $s_i(r)$, and nodal amplitudes, $a_k^i(t)$.

$$v(t) = v(a_1^1(t), \dots, a_m^1(t), \dots, a_1^n(t), \dots, a_m^n(t), s_1(t), \dots, s_m(t)) \quad (2-34)$$

In the finite element method, the approximation solution, v , is given by

$$v^k(x, t) = \sum_{j=1}^{j=m} a_j^k(t) \alpha_j(x, t) \quad k = 1, \dots, n \quad (2-35)$$

where a_j^k is a nodal amplitude of the k th dependent variable at the j th node. m and n are the number of node points and dependent variables, respectively. $\alpha_j(x, t)$ is the corresponding basis function. In contrast to the F-FEM, the basis function, α_j , is a function of both time and space because node points move continuously with time. The temporal variation of v is derived as follows by applying the chain rule differentiation to v with respect to time,

$$\frac{\partial v^k}{\partial t} = \sum_{j=1}^{j=m} \left(\frac{\partial a_j^k}{\partial t} \alpha_j + \frac{\partial s_j}{\partial t} \beta_j^k \right), \quad (2-36)$$

which implies that the approximate solution v is a function of both the amplitudes, a_j^k , and the nodal positions s_j . The basis functions α_j and β_j^k are defined by

$$\alpha_j = \frac{\partial v^k}{\partial a_j^k} \quad (2-37)$$

$$\beta_j^k = \frac{\partial v^k}{\partial s_j} \quad (2-38)$$

With the temporal variation of v given in Eq. (2-36), the standard method of weighted residual method is applied to derive the M-FEM formulation, which is given by,

$$\sum_{j=1}^{j=m} (\alpha_i, \alpha_j) \frac{\partial a_j^k}{\partial t} + \sum_{j=1}^{j=m} (\alpha_i, \beta_j^k) \frac{\partial s_j}{\partial t} = (\alpha_i, L^k(v)) \quad (2-39)$$

2.5.4 Nodal Equations

In order to close the M-FEM formulation, it is necessary to describe the temporal variation of node positions. There are two approaches to derive nodal equations. The first approach is to equi-distribute mesh function values over all zones.²⁻²² The second approach is to minimize global errors.²⁻²⁰⁻²⁻²³

In the mesh function approach, mesh functions are constructed to be a measure of local adequacies of mesh deployment. The mesh function sought is a non-negative and dimensionless function with the following properties,

$$\lim_{h_i \rightarrow 0} \theta_T^i = 0 \quad (2-40)$$

where

$$\theta_T^i \ll 1; \text{ good node deployment}$$

$$\theta_T^i \gg 1; \text{ poor node deployment} .$$

The node moving strategy is to move the nodes so as to equi-distribute the mesh function values over all zones. This can be accomplished by solving the following equation.

$$\frac{dh_i}{dt} = \theta - \theta_T^i \quad (2-41)$$

where

$$\theta = \sum_{i=1}^{i=m-1} \frac{\theta_T^i}{m-1} \quad (2-42)$$

$$h_i = s_{i+1} - s_i . \quad (2-43)$$

Because two end nodes s_1 and s_m are fixed, i.e., $ds_1/dt = ds_m/dt = 0$, the above differential equation can be easily solved to describe node movements. The mesh function, θ_T^i , is defined as linear combination of appropriate sub-mesh functions. The sub-mesh functions chosen in this study are

$$\theta_1^i = \frac{\sum_{k=1}^{k=n} w_k \left| a_{i+1}^k - a_i^k \right|}{\tau_1} \quad (2-44)$$

$$\theta_2^i = \frac{\sum_{k=1}^{k=n} w_k \left| \left(\frac{\partial a}{\partial r} \right)_{i+1}^k - \left(\frac{\partial a}{\partial r} \right)_i^k \right|}{\tau_2} \quad (2-45)$$

$$\theta_3^i = \frac{\left| Q_{i+1} - Q_i \right|}{\tau_3} \quad (2-46)$$

where Q_i is the amount of heat release due to chemical reactions at the i^{th} node. The weights, w_k , are employed to control the influence of dependent variables on node motion. Each τ_i is chosen to normalize the mesh function such that

$$\sum_{i=1}^{i=m-1} \theta_j^i = 1 \quad (2-47)$$

The first and second mesh functions, which were originally proposed by Madsen, are designed to prevent a stiff change in first and second order spatial derivatives. The third mesh function is implemented, in this work, to increase grid resolutions in the vicinity of a reaction zone. Then, the total mesh function becomes

$$\theta_T^i = \sum_{j=1}^{j=3} e_j \theta_j^i \quad (2-48)$$

where e_i 's are user specified constants. The suitable set of e_i 's is determined only by trial-and-error types of approaches. The values of e_i chosen in this study are; $e_1 = 1$, $e_2 = 0.005$, and $e_3 = 0.2$. Because the above mesh functions do not provide resistances against node crossing, additional node control is necessary to prevent nodes from crossing over each other and maintain a good node topology. Madsen recommended the following mesh function to control over excessive adjacent zone distortion,

$$\theta_4^i = \frac{|s_{i+1} - s_i|}{\tau_4} \quad (2-49)$$

The above mesh function causes the nodes to be equally spaced. However, a non-uniform node spacing may be more suited for the most of problems. Thus, in the present study, the additional node control is achieved by imposing the following constraint,

$$\frac{1}{B} < \frac{s_i}{s_{i-1}} < B \quad (2-50)$$

where B is a constant larger than 1. The B is chosen to be 5 in this study. It is important to note here that the values chosen for e_i 's and B do not affect the accuracy of model solutions significantly but do influence the numerical efficiency. In addition to node distortion, it should be noted that a extremely high node density in a small region may increase the temporal stiffness considerably. Thus, a minimum node separation distance should be enforced to maintain the numerical stiffness properties of the ODE system at the very manageable levels, i.e.

$$h_i < h_{\min} \quad (2-51)$$

The constraints are implemented by modifying m_i in small and distributing the excess over zones. The actual procedures of this node control algorithm are illustrated by Madsen.²⁻²²

The second approach is proposed by Miller.^{2-20, 2-24} This technique implicitly calculates node locations to minimize global errors. Galinas et al.²⁻²⁵ derived the following equations by minimizing the L^2 norm of the penalized residual function with respect to a_i^k and s_i .

$$\begin{aligned}
& \sum_{k=1}^{k=n} \sum_{j=1}^{j=m} w_k(\beta_i^k, \alpha_j) \frac{\partial a_i^k}{\partial t} + \sum_{k=1}^{k=n} \sum_{j=1}^{j=m} w_k(\beta_i^k, \beta_j^k) \frac{\partial s_j}{\partial t} \\
& - x_i^2 \frac{\partial s_{i-1}}{\partial t} + (x_i^2 + x_{i+1}^2) \frac{\partial s_i}{\partial t} \\
& - x_{i+1}^2 \frac{\partial s_{i+1}}{\partial t} \sum_{k=1}^{k=n} w_k(\beta_i^k, L^k(v)) \\
& + x_i w_i - x_{i+1} w_{i+1} \tag{2-52}
\end{aligned}$$

where X_i , $X_i w_i$ are penalty functions which are employed to prevent the formulation from becoming singular, to control the additional numerical stiffness arising due to introduction of nodal equations, and to provide resistances to node crossing. Considerable efforts have been made to search for appropriate penalty functions²⁻²⁵⁻²⁻²⁶ or to find a way to eliminate the necessity of penalty functions.²⁻²⁷

The performance of this approach with various penalty functions on the problems typically arising in the combustion system compares very well with alternate numerical techniques²⁻²⁸ in solving both stable and unstable freely propagating premixed laminar flames with one step chemistry.²⁻²⁹ However, as also shown by Cho et al.²⁻²⁹ for the simulation of droplet combustion, nodes are often locked into a sharp moving front. Thus as the front advances across the domain, the nodes ahead concentrate and the nodes behind stretch drastically. These difficulties may be resolved in a certain degree by incorporating Madsen's mesh function approach into the penalty function,

$$x_i^2 = \frac{c_1^2}{(\Delta s_i - \delta)} + c_2 \exp \left(\max_{i=1}^{i=m-1} (\theta - \theta_T)^i \right) \quad (2-53)$$

$$x_i \omega_i = \frac{c_3^2}{(\Delta s_i - \delta)^2} + c_2 \exp \left(\max_{i=1}^{i=m-1} (\theta - \theta_T)^i \right) (\theta - \theta_T^i) \quad (2-54)$$

It can be readily shown that these penalty functions have node movements guided by the mesh function approach, when the node deployment violates seriously the ideal mesh system defined by the mesh function.

Numerical experiments have been performed to compare the above two approaches. It was found that the second approach, which is based on minimization of global errors, depends too much on the selection of penalty functions and often introduces a severe numerical stiffness. On the other hand, the first approach, which is based on equi-distribution of mesh functions, provides only a sub-optimal node control, but no additional numerical stiffness arises from the node control. Because the problem itself is very stiff temporally, any additional stiffness due to a node control may introduce a serious difficulty in temporal integration. Thus, the first approach is employed to calculate node movements in the present study.

2.5.5 Solution Procedure

The combustion and vaporization of droplets are described by a set of differential-algebraic equations, Eq. (2-10), (2-16), (2-17), (2-18), (2-20), (2-21), and (2-31). The gas phase mass and heat balance equations, Equations (2-1), and (2-17) are discretized by the M-FEM. The liquid phase equations, Eq. (2-21) are discretized by the F-FEM with uniformly spaced gridding. Then,

the resulting ODE systems are integrated by coupling with the overall mass balance equation of the liquid droplet, Eq. (2-18), and the concentrations of the surface species.

In addition to chemical species concentration and temperature at each grid point and the droplet radius, m_p and r are unknown. Among unknowns, the m_p is a single unknown, but appears in almost every equation. In order to maintain the banded matrix structure, the m_p is treated as unknown at each grid point. Then, a set of algebraic equations is added into the ODE systems to assure that these variables are equal everywhere. A similar approach was taken by Smooke et al.²⁻¹⁶ to determine the flame speed in freely propagating adiabatic flame. The resulting ODE system with the tridiagonal matrix structure is solved by the various implementations of Gear's method.

In the most previous approaches, the Jacobian matrix is evaluated numerically to reduce efforts for computer program coding. In the current work, the analytical form of Jacobian matrix is used to improve convergeance as well as a numerical convergeance for sensitivity coefficients. Furthermore, it was found that the usage of the analytical Jacobian matrix reduces computational time for Jacobian matrix evaluation significantly. As a result, the total computation time required for the solutions was reduced by over 10 times.

Even though all the results presented in this paper are based on the above procedure, it is worthwhile to note that the energy conservation equation for the solid phase may be decoupled from those for the gas phase without loss of significant accuracy, because the liquid phase processes are much slower than the gas phase processes.

2.6 Sensitivity Analysis

Sensitivity analysis provides a formal method for extracting the relationship between input and output parameters. Sensitivity analysis can be used to evaluate the sensitivity of output parameters to model input parameters as well as the uncertainty in their values. Hence, the sensitivity analyses would be powerful interpretive tools in investigating chemically reactive flow which is complicated by non-linear interactions among various processes and includes a large number of input parameters containing significant uncertainties. However, the application of the sensitivity analyses especially to the space-time problem may become inhibitably expensive greatly exceeding the efforts required for model solutions. In this section, sensitivity analysis methods for the space-time problems are reviewed. A computationally efficient method in calculating sensitivity coefficients, which utilizes the information obtained in solution procedures, is also discussed.

2.6.1 Description of Sensitivity Coefficients

For a space-time problem in which both the system variables and the system parameters are functions of space and time, the functional derivative defined below provides elementary sensitivity information

$$\Omega_{m,\ell}(x,t,;x',t') = \frac{\delta Y_m(x,t)}{\delta \phi_\ell(x',t')} \quad (2-55)$$

The sensitivity density ($\Omega_{m,\ell}$) represents the response of the dependent variable m at position x , and time t with respect to a variation of the parameter ϕ at position x' and time t' . Thus, the sensitivity density provide a detail system response to the variation of the particular parameter value at (x', t') . However, the sensitivity equations should be solved repeatedly for each variation of parameters. Thus, the complete sensitivity information for

a single parameter may require solution of up to "n x m" equations (where n is the number of nodes, m is the number of time steps taken). Then, the calculated sensitivity densities may be examined individually or be integrated to provide a total variation of dependent variable of interest (δY_m),

$$\delta Y_m(x, t; x_1 < x < x_2, t_1 < t < t_2) =$$

$$\int_{t_1}^{t_2} \int_{x_1}^{x_2} \Omega_{m,\ell}(x, t; x', t') \delta \phi_m(x', t') dx' dt' \quad (2-56)$$

where x_1 and x_2 define the boundary of the space the spatial region, and t_1 and t_2 define the temporal duration.

For computational efficiency, the sensitivity coefficients based on constant relative variation of parameters rather than the sensitivity densities are used in this study. In order to take advantage of the constant relative variation assumption, the parameter (ϕ_ℓ) is redefined by performing linear transformation,

$$\phi_\ell = (1 + \xi_\ell) \phi_\ell \quad (2-57)$$

where ξ_ℓ is the constant parameter perturbed in the sensitivity analysis and is set equal to zero for each parameter. Then the familiar sensitivity coefficients are derived by taking partial derivative with respect to ξ_ℓ .

$$S_{i,j} = \frac{\partial Y_m}{\partial \xi_\ell} \quad (2-58)$$

The above sensitivity coefficients may be divided by Y_m to provide normalized sensitivity information.

It is often of interest to study the effects of variation of parameters in finite region of physical coordinates (i.e., $x_1 < x < x_2$) or a certain model condition. For example, many of thermal properties as well as chemical kinetic properties at high temperatures are not well known. Thus, it would be helpful to study the importance of high temperature data for these parameters. This kind of sensitivity information can be obtained by applying the linear transform defined in Eq. (2-57) only to the region of interest. If the constant variation (not constant relative variation) is assumed, then the following transformation is used

$$\phi_{\ell} = \phi_{\ell} + \zeta . \quad (2-59)$$

The sensitivity coefficients can be calculated by the same procedure discussed above.

2.6.2 Calculation of Sensitivity Coefficients

The sensitivity coefficients can be calculated by coupling the model equations with the sensitivity equations. However, this approach tends to increase the numerical stiffness and the resulting matrix size becomes large especially when a large number of parameters are considered. Here, the direct decoupled method (DDM) proposed by Dunker²⁻³⁰ was employed, in which the sensitivity equations are decoupled from the model equations, and integrated one time step behind the integration of the model equations. In this way, the sensitivity coefficients are efficiently calculated by reusing information obtained from solution procedures.

Here, the DDM is extended to treat the implicit form of ODEs by following Dunker's work. A set of implicit ODEs rather than explicit ODEs are resulted from discretization of PDEs by using the moving node FEM, which can be written as

$$A \frac{du}{dt} = g(u, t, \phi) \quad (2-60)$$

The Gear algorithm further discretizes the above ODEs by using finite difference approximations to yield

$$A(t_n, u) (u - \sum_{i=1}^{i=q} \alpha_i y_{n-i}) - h \beta_0 g(t_n, u) = 0 \quad (2-61)$$

Where q is the order of integration (here, $1 \leq q \leq 5$) and β_0 is the coefficient used in the Gear algorithm. This finite difference formulation may be re-written in a more convenient form for a modified Newton interaction technique,

$$A(t_n, u) (u - u_n^m) - h \beta_0 z(t_n, h, u, u_n^m) = 0 \quad (2-62)$$

$$z(u) = g(t_n, u) - A(t_m, u) \frac{u_n^m - a_n}{h \beta_0} \quad (2-63)$$

The solutions are obtained by the modified Newton iteration,

$$[T(t_n, y) - h \beta_o J(t_n, y)] (y_n^{m+1} - y_n^m) = - h \beta_o z(t_n, y_n^m) \quad (2-64)$$

The sensitivity equations can be derived by applying the partial derivative to Eq. 2-10.

$$[A(t_n, y) - h \beta_o J(t_n, y)] S_n = A(t_n, y) \sum_{i=1}^{i=q} \alpha_i S_{n-2} + h \beta_o z \zeta, n \quad (2-65)$$

The similarity between Newton iteration formula for solutions and sensitivity equations become quite apparent by comparing these two equations. The DDM greatly increases computational efficiency by taking advantage of the similarity found between these two equations. The procedure of the DDM is as follows: the sensitivity equations, Eq. (2-65) and the model equations, Eq. (2-64), are solved sequentially. The model equations are integrated first from t_{n-1} to t_n by using the Newton iterative formula. During this solution procedure, the parameters related to integration such as a time step ($t_n - t_{n-1}$) and the order of integration (q_n) are determined. Then the Jacobian matrix is re-evaluated and LU decomposed, and these integration parameters as well as the LU decomposed matrix and the model solutions are used to solve the sensitivity equations. Each sensitivity equation is solved separately. This procedure is performed iteratively with time.

2.7 References for Section 2.0

2-1 Coffee, T.P., and Heimerl, J.M., "Transport Algorithms for Premixed Laminar Steady State Flame, Comb. and Flame," 43, 273 (1981).

2-2 Kee, R.J., Warnartz, J., and Miller, J.A., "A Fortran Computer code Package for the Evaluation of Gas Phase Viscosities, Conductivities, and Diffusion Coefficients," Sandia National Laboratories Report, SAND 83-8209, (1983).

2-3 Yanenko, N.N., The Method of Fractional Steps, Springer, New York, (1971).

2-4 Zienkiewicz, O.C., Hinton, E., Leung, K.H., and Taylor R.L., Innovative Numerical Analysis for the Applied Engineering Sciences, ed. Shaw, R., University Press of Virginia, Virginia, (1980).

2-5 Preussner, P.R., and Brand, K.P., "Application of a Semi-implicit Euler Method to Mass Action Kinetics," Chem. Engng. Sci., 36, 1633 (1981).

2-6 Gear, C.W., Numerical Initial Value Problems, Prentice Hall, Eglewood Cliffs, N.J., (1971).

2-7 Oran, E., and Boris, J., "Detailed Modelling of Combustion systems," Pro. Energy Combust., 1, 1 (1981).

2-8 Oran, E., and Boris, J., Numerical Simulations of Reactive Flow, Elsevier, New York, 1987.

2-9 McRae, G.J., Goodin, W.R., and Seinfeld, J.H., "Numerical Solutions of the atmospheric Diffusion Equations for chemically Reactive Flows," J. of Comp. Phys., 45, 1 (1982).

2-10 Cho, S.Y., "Mathematical Modeling and Sensitivity Analysis of Acid Deposition," Ph.D. Thesis, University of Iowa, (1986).

2-11 Cho, S.Y., Carmichael, G.R., and Cohen, D.M., "Coupled Transport and Chemistry Calculations on NASA/GODDARD's Massively Parallel Processor Computer," computers and Chemistry, in press.

2-12 Dwyer, H.A., and Sanders, B.R. (1986). Detailed Computation of Unsteady Droplet Dynamics. Twentieth Symposium (international) on Combustion Institute, Pittsburgh.

2-13 Cho, S.Y., Carmichael, G.R., and Rabitz H., "Sensitivity Analysis of the Atmospheric Reaction-Diffusion Equation," Atmos. Environ., 21, 2598 (1987).

2-14 Yuk, K.I., "Extrapolative Crank-Nicolson Galerkin Finite Element Method Applied to a Diffusion Reaction Problem," M.S. Thesis. Univ. of Iowa, (1982).

2-15 Carey, G.F., "A Mesh Refinement Scheme for Finite Element Computations," Comp. Meth. in Applied Mech. and Eng., 1, 93 (1976).

2-16 Babuska, I., and Rheinboldt, "Adaptive Approaches and Reliability Estimations in Finite Element Analysis," Comp. Meth. in Applied Mech. and Eng., 17/18, 519 (1979).

2-17 Smooke, M.D., Miller, J.A., and Kee, R.J., "Determination of Adiabatic Flame Speeds by Boundary Value Methods," Comb. Sci. and Tech., 34, 79 (1983).

2-18 Berger, M.J., and Oliger, J., "Adaptive Mesh Refinement for Hyperbolic Partial Differential Equations," J. of Comp. Phys., 53, 484 (1984).

2-19 Bieterman, M., and Babuska, I., "An Adaptive Method of Lines with Error Control For Parabolic Equations of the Reaction-Diffusion Type," J. of Comp. Phys., 63, 33 (1986).

2-20 Miller, K. and Miller, R.N., "Moving Finite Elements I & II," SIAM 2-21 Lynch, D.R., J. of Comp. Phys., 47, 387 (1982).

2-22 Madsen, N.K., "Non-Stiff Adaptive Moving Node Techniques," Scientific Computing, Stepleman, R. ed, 19, (1983).

2-23 Yanenko, N.N., Kovenya, V.M., Lisejkin, V.D., Fomin, V.NM., Vorozhotsov, E.V., "On Some Methods for the Numverical Simulation of Flows with Complex Structure," Comp. Meth. in Applied Mech. and Eng., 17/18, 659 (1979).

2-24 Miller, K., "Alternative Modes to Control the Nodes in the Moving Finite Element Method," Adaptive Computational Methods for Partial Differential Equations (Babuska, I., Chandra, J., and Flaherty, J.E., ed), 165, SIAM, Philadelphia, P.A., (1983).

2-25 Gelinas, R.J., Doss, S.K., and Miller, K., "The Moving Finite Element Method: Application to General Partial Differential Equations with Multiple Large Gradients," J. of Scientific Computing (Stepleman, R. ed.), 55, (1981).

2-26 Hrymak, A.N., McRae, G.J., and Westerberg, A.W., "An Implementation of a Moving Finite Element Method," J. of Comp. Phys., 63, 168 (1986).

- 2-27 Wathen, A.J., "Moving Finite Elements and Oil Reservoir Modeling," Ph.D. Thesis, Dept. of Mathematics, Univ. of Reedling, (1984).
- 2-28 Peters, N., and Warnatz, J., (eds), "Numerical Methods in Laminar Flame Propagation," Vieweg, Wiesbaden, (1982).
- 2-29 Cho, S.Y., Yetter, R.A., and Dryer, F.L., "Application of the Moving Finite Element Method to Chemically Reactive Flow Problems," Eastern Section: The Combustion Institute Meeting, Combustion Institute, Pittsburgh, (1988).
- 2-30 Dunker, A.M., "The Decouple Direct Method for Calculating Sensitivity Coefficients in chemical Kinetics," *J. Chem. Phy.* 81, 2385 (1984).

3.0 HETEROGENEOUS SURFACE REACTION MECHANISMS

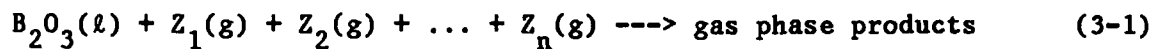
This section describes the heterogeneous surface reaction mechanisms that will be used to describe particulate boron ignition, oxidation, and volatilization. Mechanisms are presented for two idealized cases corresponding to the two distinct stages of boron combustion that have been observed experimentally.^{3-1,3-2} The first reaction set includes reactions between gas phase species and a boron oxide surface. This case is applicable when the boron particle has a significant oxide coating (> 10 Å) and is important in describing the chemical transformations that promote oxide gasification. The second case treats a "clean" boron surface (no appreciable oxide coating) is applicable to the second-stage ignition and full-fledged boron surface burning that occurs at high temperatures (ca. 1900 K) once the oxide layer has been removed.

3.1 Overview

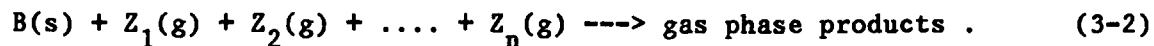
The systematic development of a complete and self-consistent kinetic model for the heterogeneous reactions which may be important processes in the two observed stages of boron combustion proceeded in four steps.

First, thermodynamic equilibrium calculations for several hydrocarbon/boron/air mixtures and kinetic calculations using the homogeneous gas phase oxidation model developed previously^{3-3,3-4} were used to identify potential gas phase reactants. These gas phase species will be designated as Z(g).

Second, a complete heterogeneous reaction set for particulate boron and liquid B₂O₃ gasification in a hydrocarbon combustion environment was formulated in terms of global reactions having the general form



and



Third, kinetic mechanisms consisting of surface adsorption and desorption steps were developed which could collectively describe the global reactions in Eqs. (3-1) and (3-2). In the case of B_2O_3 gasification, these reaction steps were formulated in terms of the structure of vitreous boron oxide using elementary thermochemical and kinetic arguments. In the case of particulate boron surface oxidation, kinetic mechanisms and rate parameters were formulated on the basis of experimentally observed reaction channels and measured reaction cross sections for small boron ion clusters.

Fourth, kinetic calculations were performed and model results analyzed for internal consistency and general agreement with available experimental data.

Since the number of reactions represented by Eqs. (3-1) and (3-2) is enormous, it was necessary to selectively prune this reaction set to a more computationally manageable number of reactions without excluding important reaction pathways. Consequently, thermochemical and, when possible, kinetic data, in conjunction with experimental observations and earlier modeling work were used to extract from Eqs. (3-1) and (3-2) the most important reactions.

For a first order representation of the surface kinetics, three criteria were used to reduce the reaction set defined by Eqs. (3-1) and (3-2). First, only reactions whose reaction enthalpy is less than some maximum enthalpy are included in the reduced reaction set. The cutoff enthalpy was defined based on the vaporization enthalpy of the appropriate condensed phase to ensure that

the surface reactions included in the model were thermodynamically competitive with vaporization. Second, global reactions which involve gas phase reactants and/or products that were predicted to be negligible on the basis of thermodynamic and kinetic calculations with the homogeneous gas phase oxidation model were excluded from the surface reaction model to ensure internal consistency. This criterion eliminated global reactions, for example, which satisfied the first criterion but yielded $B_2O(g)$ as a final gas phase product. Third, only reactions which are first order in gas phase reactants were included in the surface kinetics model presented here. This criterion was initially based on the assumption that reaction rates for second order reactions would tend to be slower than first order reaction rates. This assumption was found to be consistent with model calculations (summarized in Section 4) for high temperature boron oxide vaporization and boron combustion which indicated that only ca. 1% of the surface was covered by adsorbed species. However, the reaction mechanisms adopted in this model would not provide an adequate description of oxide layer formation at lower temperatures ($T < 1600$ K).

It is important to note that these criteria are not rigid. Rather, they provide defensible reasons for the particular reactions included in the kinetic model, yet are readily expanded to include additional reactions (by increasing the cut-off enthalpy, including additional species in the homogeneous oxidation model, or incorporating second order processes) as additional experimental or theoretical work dictates is necessary.

3.2 Gas Phase Boron Speciation and Thermodynamics

3.2.1 Gas Phase Reactants, Heats of Formation and Entropies

Thermochemical equilibrium calculations and results from the application of gradient sensitivity analysis to the kinetic calculations for the homogeneous gas phase oxidation indicate that $HOBO(g)$, $B_2O_3(g)$ and $BO_2(g)$ are major gas phase species in oxygen rich environments while $HBO(g)$, $B_2O_2(g)$ and

BO(g) are the primary species in fuel rich environments.^{3-3,3-4} Thus, these species, in conjunction with several hydrocarbon combustion intermediates and products, will be viewed as comprising the primary set of gas phase species which can react with the boron or boron oxide surface. The complete set of primary gas phase species and their entropies and heats of formation are given in Table 1. The heat of formation for HBO(g) is based on the theoretical calculations of Page.³⁻⁵ All other data is from recent JANAF listings.³⁻⁶

Table 1 - $\Delta H_f,_{298}$ and S_{298} for Primary Gas Phase Speciation
(\pm uncertainties in parentheses)

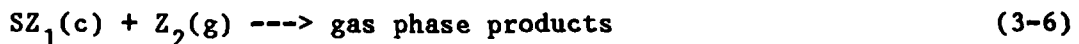
Species	$\Delta H_f,_{298}$ (kcal/mole)	S_{298} (cal/mole-deg)
BO	0.0 (2.0)	48.63 (0.01)
BO_2	- 68.0 (2.0)	54.93 (0.05)
B_2O_2	-109.0 (2.0)	57.98
B_2O_3	-199.8 (1.0)	[67.8 (1.0)]
HBO	- 60.0 (0.7)	48.40 (0.1)
HOBO	-134.0 (1.0)	[57.30]
H	52.1 (0.001)	27.39 (0.004)
O	59.6 (0.024)	38.47 (0.005)
OH	9.3 (0.29)	43.89 (0.01)
H_2O	- 57.8 (0.01)	45.11 (0.01)
CO	- 26.4 (0.04)	47.21 (0.01)
CO_2	- 94.1 (0.011)	51.07 (0.03)

3.2.2 Gas Phase Bond Energies

The heats of formation in Table 1 were used to determine the bond energies given in Table 2. These bond energies, along with an assumed bond order, were subsequently used to estimate reaction enthalpies and activation energies for the elementary reactions defined in Section 3.3. Note that not all the species listed in Table 2 are primary gas phase species. However, they were all considered in estimating the reaction enthalpies of elementary reactions and heats of formation for surface speciation and are listed here for completeness.

3.3 Definition of Elementary Reactions

As noted in Section 3.1, kinetic mechanisms for the global reactions represented by Eqs. (3-1) and (3-2) were formulated in terms of simple adsorption and desorption reaction steps. In addition, a few second order reactions were adopted to ensure that the global reactions were reversible. As a result, four classes of reactions were defined in the present model to be elementary and have reaction rates which could be expressed as a simple Arrhenius function of temperature. These reactions may be written, in general, as:



where S is a reactive surface site and SZ(c) is a surface complex.

Table 2 - Gas Phase Bond Energies (\pm uncertainties in parentheses)

Bond	Bond Order	D_o (kcal/mole)	D_o (eV)
HB=O	2.0	225.4 (3.0)	9.23
B=O	2.0	192.8 (3.5)	8.37
OBB=O	2.0	191.0 (27.0)	8.29
OBOB-O	1.5	149.8 (27.0)	6.50
HOB-O	1.5	145.8 (2.0)	6.33
HO-BO	1.5	143.3 (3.3)	6.21
(OH) ₂ B-OH	1.0	132.5 (4.8)	5.75
OBO-BO	1.0	131.0 (5.0)	5.68
OB-O	1.0	127.0 (4.5)	5.51
BO-B	1.0	120.0	
OB-BO	1.0	109.0 (6.0)	4.73
(HO) ₂ B-B(OH) ₂	1.0	76.0 (13.0)	3.30
H-B	1.0	78.2 (0.04)	3.39
HB-H	1.0	110.3	
H-BO	1.0	98.7 (15.5)	4.28
H-H	1.0	103.0 (0.5)	4.47
O=O	2.0	118.0 (0.1)	5.12
H-O	1.0	101.0 (0.3)	4.38
HO-H	1.0	118.0 (0.1)	5.12
H-OBO	1.0	118.1 (3.0)	5.00
C=O	2.0	256.0 (0.04)	11.11
OC=O	2.0	127.6 (0.06)	5.54

3.3.1 Adsorption Reactions

For our present purposes, adsorption will refer strictly to chemisorption processes. Ideally, adsorption channels and rate parameters for the kinetic model would be based on experimental data or microscopic theoretical calculations. Unfortunately, this approach was only partially feasible in the current model because of the lack of experimental data. It was therefore necessary to formulate adsorption reactions and estimate rate parameters using simple thermodynamic and kinetic arguments. This was particularly true for the B_2O_3 surface. When experimental data was lacking, therefore, chemisorption at the surface of a condensed phase was treated as follows:

- a. The clean surface was assumed to have a particular structure in terms of which it was possible to define reactive surface sites or reactive surface structural units.
- b. Potential adsorption channels and surface speciation was defined by considering the various bonding possibilities between a surface site and a gas phase species Z.
- c. Gas phase bond energies and assumed surface species structure were used to estimate adsorption enthalpies. The most thermodynamically stable surface complexes that were consistent with the overall global reactions in Eqs. (3-1) and (3-2) were adopted as the dominant adsorption channel.
- d. The adsorption rate constant was taken to have the form³⁻⁷

$$k_a(T) = k_{\max}(T) \times s_0 \times e^{(-E_a/k_B T)} \quad (3-7a)$$

where

$$k_{\max} = [k_B T / 2\pi m]^{1/2} \quad (3.7b)$$

In Eq. (3.7) k_{\max} is the number of molecules of mass m striking the surface per unit area per second, s_0 is the sticking probability, E_a is the activation energy and k_B is Boltzmann's constant. If there is no activation energy and if every molecule striking the surface chemisorbs ($s_0 = 1$), then $k_a = k_{\max}$ is an upper limit to rate constant.

e. Lastly, the chemisorption rate is given by the Langmuir rate³⁻⁷

$$r_a(T) = k_a(T) \times (1-\theta) \times [Z(g)] \quad (3.8)$$

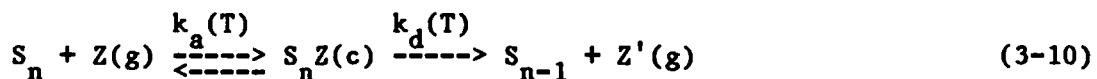
for immobile adsorption, and

$$r_a(T) = k_a(T) \times (1-\theta)^2 \times [Z(g)] \quad (3.9)$$

for mobile adsorption where θ is the fraction of surface sites covered by adsorbate.

3.3.2 First Order Desorption Reactions

The global reactions defined by Eqs. (3-1) and (3-2), may be characterized by an initial adsorption of gas phase $Z(g)$ to yield the surface complex $SZ(c)$, followed by decomposition of this complex to yield the final gas phase product $Z'(g)$. A complete reaction sequence can be written as



The desorption enthalpy is then given by

$$H_d = H_r - H_a \quad (3-11)$$

where H_a is the estimated adsorption enthalpy and H_r is the reaction enthalpy determined from heats of formation for reactants and products. The first-order desorption rate constant (probability per sec) is given by

$$k_d(T) = A_d \times e^{(-E_d/k_B T)} \quad (3-12)$$

As a first-order approximation, the coefficient A_d was expressed as the transition state frequency factor $k_B T/h$ and the activation energy was estimated using gas phase bond energies.

The desorption reaction rate for the inverse adsorption step, i.e.,



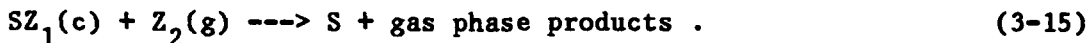
was estimated from the adsorption rate constant k_a and equilibrium constant K_{eq} . K_{eq} was computed using the estimated adsorption enthalpy and tabulated values for gas phase entropies from Table 1.

3.3.3 Second Order Reactions

For the B_2O_3 surface, the simplest adsorption model was typically found to result in the formation of two surface complexes for each gas phase reactant adsorbed. Consequently, for the global reactions represented by Eq. (3-1) to be reversible it was necessary to include the second order desorption steps represented by



in the kinetic model. Similarly, it was found that for the global reactions represented by Eq. (3-2) for particulate boron to be reversible, the kinetic model had to include second order reactions of the form



In both these cases, rate parameters were estimated from K_{eq} for the global reaction and the adsorption/desorption rates defined in Sections 3.3.1 and 3.2.2.

3.4 Boron Oxide Surface Reactions

Oxidation reactions between oxygen and a clean boron surface are typically exothermic (see Section 3.5.1). Subsequent reactions, however, between gas phase reactants and the oxide layer that forms on the boron surface are typically highly endothermic. Consequently, oxide layer formation tends to inhibit oxidation until the particle temperature, through convective and radiative heat transfer or self-heating, reaches the vaporization temperature of B_2O_3 . Removal of the oxide layer can be aided by surface reactions which, although endothermic, require less energy than is needed for vaporization. Experimental evidence indicates that hydrogen containing species tend to increase B_2O_3 vaporization rates³⁻⁸ and to decrease both the ignition temperature and ignition time delay for boron particles.^{3-1,3-2}

3.4.1 Global Reactions

Table 3 lists reactions between condensed B_2O_3 and primary gas phase species to produce gas phase products. Following the criteria discussed in Section 3.1, only reactions which are first order in gas phase reactants and whose reaction enthalpy is less than 110 kcal/mole are included; reactions with a larger reaction enthalpy would be competitive with B_2O_3 vaporization ($\Delta H \sim 100$ kcal/ mole). Also, reactions which involved $B(OH)_2(g)$ as a final

product were excluded, even if the reaction enthalpy was less than 110 kcal/mole, because equilibrium calculations for the oxidation of a JP4/solid boron mixture in air indicated that $B(OH)_2$ would be a minor species.^{3-3,3-4} As shown in Table 3, there are only three reactions which,

Table 3 - Boron Oxide Surface: Global Reactions (Excludes Reactions With Reaction Enthalpies > 110 kcal/mole and Reactions Involving $B(OH)_2(g)$ As a Product)

Reaction	ΔH (kcal/mole)
$B_2O_3(l) + O(g) \longrightarrow 2BO_2(g)$	108.4 (4.5)
$B_2O_3(l) + OH(g) \longrightarrow HOBO(g) + BO_2(g)$	92.7 (3.8)
$B_2O_3(l) + H_2O(g) \longrightarrow 2HOBO(g)$	93.8 (2.5)

based on current thermochemical data, satisfy these constraints. The important gas phase reactants are the hydrocarbon combustion products $O(g)$, $OH(g)$ and $H_2O(g)$, although $O(g)$ is not expected to have much influence on the gasification process.

3.4.2 Oxide Structure

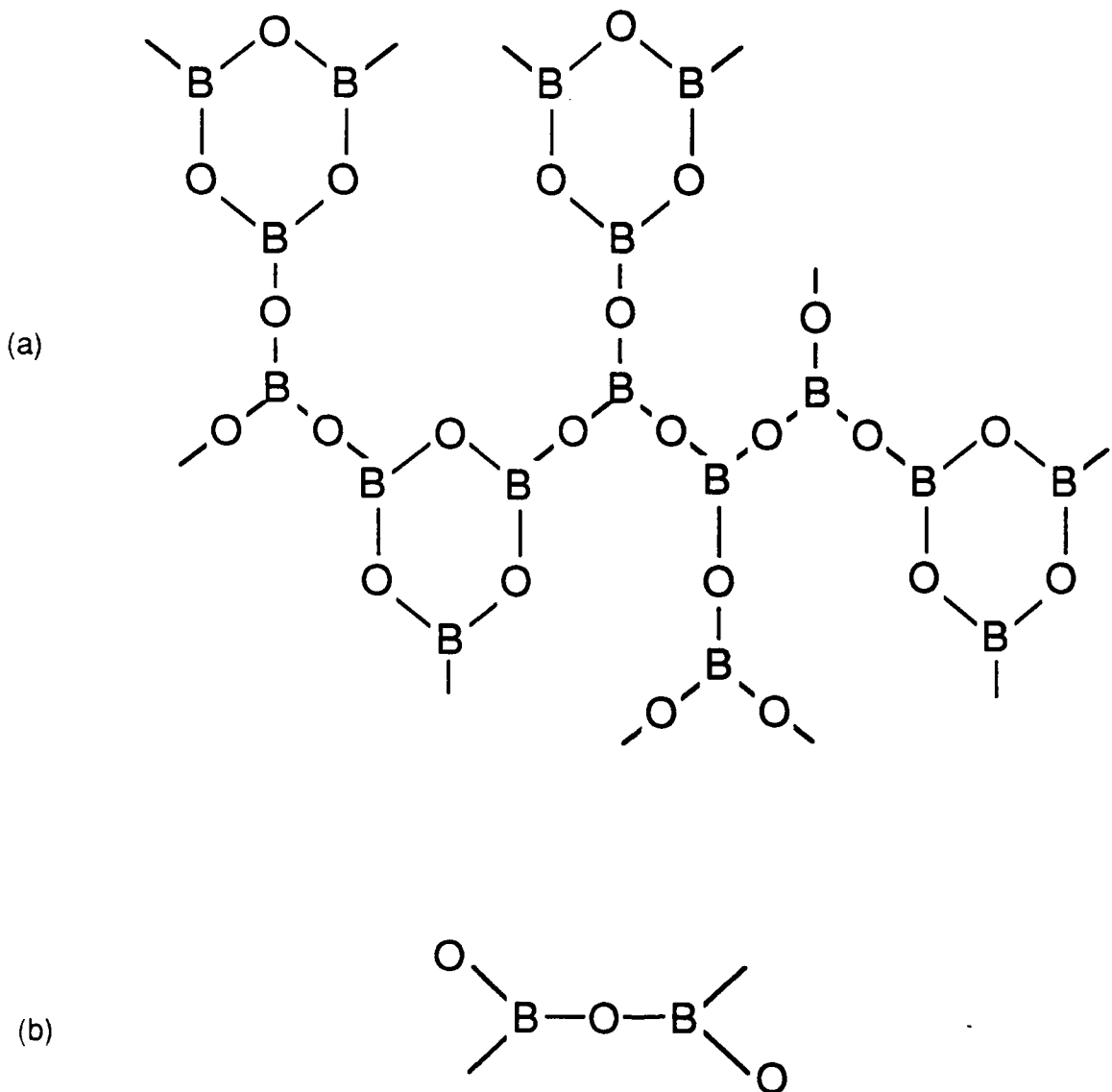
Structure of vitreous boron trioxide has been a subject of considerable disagreement and controversy. Early concepts ranged from that of a molecular liquid consisting of the dimers, B_4O_6 , an ionic melt involving complex boron-oxygen ions, to that of a highly associated network of interlinking BO_3 triangles.³⁻⁹ The latter structure is in general agreement with the classical theory of the vitreous state for B_2O_3 , SiO_2 and GeO_2 .

Early ^{11}B NMR spectra were thought to generally support the model of a random network of planar BO_3 triangular units interconnected through the

oxygen atoms at the vertices.^{3-10, 3-11} However, a double bond resonance in which boron attracts one electron from oxygen and forms a predominately ionic bond in addition to the covalent sigma bond was introduced to bring experimental measurements of the quadrupole coupling constant into agreement with trigonal BO_3 structural units.

The most recent studies based on infrared and Raman spectroscopy,³⁻¹² X-ray,³⁻¹³ and NMR techniques³⁻¹⁴ have been interpreted to support the existence of a random network of boroxol rings interconnected by a random number of BO_3 triangles. NMR ^{17}O spectra for B_2O_3 glass, for example, indicated the presence of two distinct oxygen sites corresponding to oxygen atoms inside and outside the boroxol ring.³⁻¹⁴ Spectra of oxygen atoms outside the boroxol rings were characterized by much larger distributions in the coupling constant and asymmetry parameter than the spectra for oxygen atoms in the boroxol rings. In addition, an X-ray diffraction study of molten boron trioxide (650 C) concluded that the melt contained a mixture of boroxol rings linked by independent BO_3 units.³⁻¹⁵

Based on these latter experimental results, the structure of condensed phase, vitreous B_2O_3 can be represented as shown in Figure 3.1a. However, for the purpose of estimating adsorption and desorption kinetic and thermochemical parameters for the global surface reactions listed above, we can initially neglect subtle differences in the bond angles and bond strengths of different surface sites, since the uncertainty in the estimated reaction rates should encompass any differences in surface site reactivity due to the presence of boroxol rings. Thus, for the present model, a reactive surface site will be represented as shown in Figure 3.1b. Our model for condensed B_2O_3 is, consequently, more consistent with studies based on computer modeling³⁻¹⁶ and molecular dynamics calculations³⁻¹⁷ which hold that the structure of vitreous boron trioxide can be understood on the basis of a continuous random network of BO_3 triangles containing no ring structures.

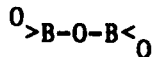


M90-262/R.B.

Figure 3.1. (a) One proposed structure of vitreous B_2O_3 consisting of boroxy rings interconnected by BO_3 units. (b) Surface structural unit used in the kinetic model to describe surface adsorption and desorption reaction steps.

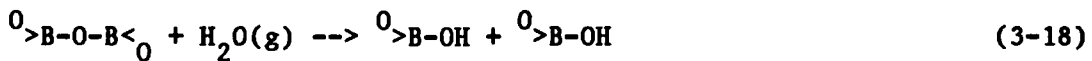
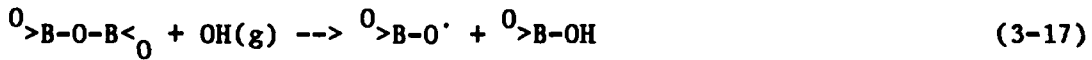
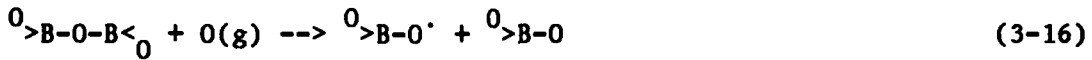
3.4.3 Adsorption Thermodynamics and Kinetics

For the B_2O_3 surface, the basic structural unit used to define surface speciation is



where the oxygen atoms are bonded through B-O bonds in trigonal BO_3 units. Surface speciation is then defined by treating the reactions between gas phase reactants and the B_2O_3 reactant as a simple 'bimolecular' reaction. Based on the reactions in Table 3, $O(g)$, $OH(g)$ and $H_2O(g)$ are the only gas phase reactants which need to be considered at this stage.

For each of the three gas phase reactants (O , OH , and H_2O) in which we are primarily interested, there are several potential surface complexes that could be formed upon adsorption. However, it was found that most of these complexes were either more than 10 Kcal endothermic, whereas the most thermodynamically favored complexes were typically 1-20 kcal exothermic, or would require significant bond rearrangement to yield final gas phase products consistent with the global reaction products in Table 3. Since experimental data for the kinetic mechanisms is not currently available, the most straightforward procedure was to adopt only the most thermodynamically stable surface complexes, based on estimated adsorption enthalpies, that were consistent with the global surface reactions in Table 3. As a result, the following three adsorption reactions were used in the kinetic model:



In Eqs. 3-16 and 3-17, $0\cdot$ represents oxygen with an unpaired electron.

Each of the adsorption reactions can be viewed as resulting from the fragmentation of a $>B-O-$ bond on the surface and the formation of a new bond between the electron deficient boron and the more electronegative portion of the gas phase reactant.

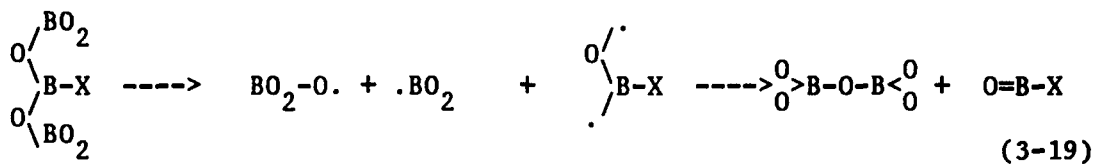
Estimated chemisorption enthalpies and rate parameters for the adsorption reactions are summarized in Table 4. The adsorption enthalpies and activation energies are based on gas phase bond energies. The sticking probabilities are based on a rough analogy to the adsorption probabilities for these reactants with other substrates.

Table 4 - Boron Oxide Surface: Adsorption Reactions

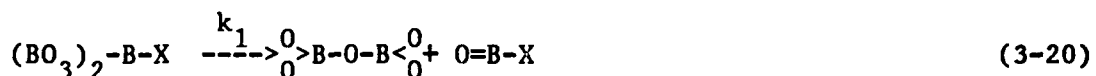
Z(g)	ΔH_{298} (kcal/mole)			$k_a(T) = k_{max} \times s_o \times e(-E_a/RT)$			Adsorption Products
	Min	Est	Max	k_{max} (cm/s)	s_o	E_a (kcal/mole)	
0	0	-10	-50	$925xT^{0.5}$	0.2 - 0.7	0 - 30	$2[>BO\cdot]$
OH	0	-10	-25	$897xT^{0.5}$	0.2 - 0.7	0 - 30	$[>BOH] + [>BO\cdot]$
H_2O	0	-10	-35	$872xT^{0.5}$	0.1 - 0.6	5 - 50	$2[>B-OH]$

3.4.4 Desorption Reactions

The surface species that result from the adsorption reactions, Eqs. (3-16) and (3-17), may be written as $>B-X$ with $X=(OH, O\cdot)$ where the dot indicates a lone electron. Then gas phase products consistent with the reactions in Eq. (3.1) can be viewed as arising from the following sequence of bond cleavage and formation:



It is clear that this reaction sequence may not be elementary. Nevertheless, it will be assumed that reaction of the two radicals to yield the B_2O_3 surface structural unit and formation of the $\text{O}=\text{B}-$ double bond is much faster than fragmentation of the two $\text{B}-\text{O}$ bonds. The decomposition reaction can then be written as



In Equation (3-20) k_1 is the first-order desorption rate constant given by

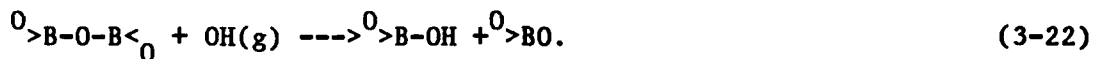
$$k_1 = A_1 e^{-E_1/RT} \quad (3-21)$$

where the desorption coefficient A_1 is given approximately by the transition state frequency factor $k_B T/h$. Desorption reaction products, reaction enthalpies and reaction rates are summarized in Table 5.

Table 5 - Boron Oxide Surface: First Order Desorption Reactions

Reaction	H ₂₉₈ (Kcal/mole)			k=A ₁ *e(-E ₁ /RT)	
	Min	Est	Max	A ₁ (ps ⁻¹)	E ₁ (Kcal/mole)
>B-OH \rightarrow HOBO(g)	39	51	63	20	40 - 60
>BO. \rightarrow BO ₂ (g)	42	54	66	20	40 - 70

It can be seen that these reactions in conjunction with the chemisorption reactions in Table 4 can be used to describe the reactions in Eq. (3-1) for the B_2O_3 surface which are first order in gas phase reactants. For example, the reaction between the B_2O_3 surface and the hydroxyl radical $OH(g)$ to yield $HOBO(g)$ and $BO_2(g)$ can be described by the following reaction sequence:



3.5 Boron Particle Surface Reactions

Once the oxide layer is removed, a boron particle burns rapidly with a surrounding flame sheet which is detached, but near the surface (see Figures 1.1 and 1.2). Since the volatility of boron is low, boron burns more like a carbon particle rather than a liquid hydrocarbon droplet.³⁻¹⁸ In particular, gasification of the boron particle occurs by chemical transformation into more volatile components. Thus, heterogeneous and homogeneous chemistry play a more dominant role in the gasification of boron than for liquid hydrocarbons. For example, liquid hydrocarbon droplets gasify primarily by a simple vaporization process which proceeds in the presence or absence of an oxidant.

The volatile component formed during boron gasification was initially believed to be $BO(g)$, however there may be significant levels of $HOBO(g)$ and $HBO(g)$, as well as $B_2O_3(g)$, $B_2O_2(g)$ and $BO_2(g)$. It is interesting to note that the dominant equilibrium gas phase boron species $HOBO(g)$ and $HBO(g)$ (in boron/JP4/air systems) are isoelectronic with the primary hydrocarbon oxidation products $CO_2(g)$ and $CO(g)$, respectively.^{3-3, 3-4} The formation of BO and other suboxides and suboxyhydrides may be compared to the formation of

CO during carbon gasification. There, $\text{CO}_2(\text{g})$, the major carbon combustion product, diffuses back to the carbon particle surface to react heterogeneously to form more $\text{CO}(\text{g})$. Boron oxides and oxyhydrides may play similar roles in boron combustion.

3.5.1 Global Reactions

Table 6 lists reactions between solid boron and primary gas phase species to produce gas phase products. Only reactions whose reaction enthalpy was less than 150 kcal/mole are included; more endothermic reactions would not be thermodynamically competitive with boron vaporization since the heat of formation of $\text{B}(\text{s})$ is approximately 133 kcal/mole. In addition, this reaction list is limited to those reactions which are first order in gas phase reactants. Lastly, reactions which involved $\text{B}_2\text{O}(\text{g})$, boron hydrides and species such as $\text{B}(\text{OH})_2(\text{g})$, $\text{H}_3\text{B}_0_3(\text{g})$ and $\text{H}_3\text{B}_3\text{O}_3(\text{g})$ were excluded because these species are minor gas phase constituents.^{3-3, 3-4}

3.5.2 Experimental Rate Data

Two sets of experimental data, summarized below, were used to estimate reaction steps and rate parameters for the global reactions in Table 6.

Cluster Ion Reactions

Anderson et. al³⁻¹⁹⁻³⁻²² have performed a series of investigations into the reactivity of boron ion clusters using the cluster ion beam technique. In this work, the reactions of thermalized, size selected B_{1-13}^+ ions were examined under single collision conditions for several gas phase reactants, including $\text{O}_2(\text{g})$, $\text{D}_2\text{O}(\text{g})$, $\text{CO}_2(\text{g})$ and $\text{CO}(\text{g})$. Using experimental reaction cross sections, temperature dependent rate constants for these reactants were then obtained by dividing the measured cross section by a collision cross section and averaging over a Boltzmann distribution. For reference, the B_{12}^+ cluster reactions and product channels observed by Anderson's group are listed in Table 7.

Table 6 - Boron Surface: Global Reactions

Reaction	$\Delta H(298)$ (Kcal/mole)
$B(s) + O(g) \rightarrow BO(g)$	-59.6 (2.0)
$B(s) + O_2(g) \rightarrow BO_2(g)$	-68.0 (2.0)
$B(s) + O_2(g) \rightarrow BO(g) + O(g)$	59.6 (2.0)
$2B(s) + O_2(g) \rightarrow B_2O_2(g)$	-109.0 (2.0)
$2B(s) + O_2(g) \rightarrow 2BO(g)$	0.0 (4.0)
$B(s) + OH(g) \rightarrow HBO(g)$	-56.7 (1.0)
$B(s) + OH(g) \rightarrow BO(g) + H(g)$	42.8 (2.3)
$B(s) + H_2O(g) \rightarrow BO(g) + H_2(g)$	57.8 (2.0)
$B(s) + H_2O(g) \rightarrow HBO(g) + H(g)$	62.5 (0.7)
$B(s) + BO_2(g) \rightarrow B_2O_2(g)$	-41.0 (4.0)
$B(s) + BO_2(g) \rightarrow 2BO(g)$	68.0 (6.0)
$B(s) + B_2O_3(g) \rightarrow B_2O_2(g) + BO(g)$	90.8 (6.0)
$B(s) + HOBO(g) \rightarrow BO(g) + HBO(g)$	86.6 (3.7)
$B(s) + HOBO(g) \rightarrow B_2O_2(g) + H(g)$	77.1 (3.0)
$B(s) + CO_2(g) \rightarrow BO(g) + CO(g)$	67.7 (2.0)

Of the 15 reactions in Table 6 one reaction can be neglected based on Anderson's boron ion cluster work. Specifically, for clusters larger than B_6^+ , the D_2O product distributions were observed to be dominated by a single channel: $B_n^+ + D_2O(g) \rightarrow B_{n-1}D^+ + HBO(g)$. Accordingly, we can assume that $HBO(g) + H(g)$ is the primary product channel for the reaction between particulate boron and H_2O and neglect the channel corresponding to $BO(g) + H_2(g)$.

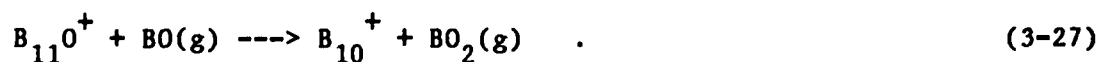
Table 7 - B_{12}^+ Cluster Reaction Product Channels

Reaction	Gas Phase Products (most stable)	Reaction Probability	
		1750 K	2500 K
$B_{12}^+ + O_2 \rightarrow B_{11}O^+$	BO	0.00834	0.008001
$\rightarrow B_{10}^+$	B_2O_2	0.046932	0.052014
$\rightarrow B_{11}^+$	BO_2	5.3×10^{-9}	3.6×10^{-7}
$B_{12}^+ + D_2O \rightarrow B_{10}D_2^+$	B_2O	0.030898	0.022496
$\rightarrow B_{11}D^+$	DBO	0.449861	0.408516
$B_{12}^+ + CO_2 \rightarrow B_{12}O^+$	CO	0.000321	0.000528
$B_{12}^+ + CO \rightarrow B_{12}CO^+$	----	0.000137	0.00016

Note also that the reaction probability for



is on the order of 10^{-7} at $T=2500$. As a consequence, in the present model we shall assume that the 2nd global reaction in Table 6, $B(s) + O_2(g) \rightarrow BO_2(g)$, proceeds via the reaction sequence.



It should also be noted that in the channel producing $B_2O_2(g)$ no surface complex is formed. In our model, however, we will assume that for larger particles thermal accommodation will allow complex formation with a residence time governed by the desorption rate for $B_2O_2(c) \rightarrow B_2O_2(g)$. However, to maintain internal consistency with other reactions, additional desorption channels have also been included.

Lastly, to ensure that global reaction 3 in Table 8 is reversible, the reaction



must be included in the model. Written as an adsorption reaction, this incorporates an $O_2(g)$ reaction channel that was not observed by Anderson.

Flow Reactor Observations

Rosner et. al.³⁻²⁴⁻³⁻²⁶ have investigated the heterogeneous kinetics for the high temperature gasification of solid boron utilizing low-pressure transverse filament flow reactor techniques and 'real-time' microwave induced plasma emission spectroscopy (MIPES) element detection. This work included studies of reactions between solid boron and $O(g)$, $O_2(g)$, $CO_2(g)$, $H_2O(g)$ and $B_2O_3(g)$. Experimental conditions typically covered temperatures between 1300 K and 2100 K and reactant partial pressures between ca. 10^{-3} and 10^{-1} Pa. Measured reaction rates were reported in terms of a non-dimensional, 'overall' rate constant that was defined as the ratio between the net flux of boron atoms, irrespective of speciation, emerging from the surface as a result of chemical reaction, to the arrival flux of gaseous reactant. The reported reaction probabilities are therefore independent of reaction products.

In the present model, this experimental work was used to estimate rate constants for boron surface reactions with $O(g)$ and $B_2O_3(g)$. For $B_2O_3(g)$, the

experimental data indicate a remarkably high reaction probability with a maximum close to unity near 2000 K, much higher than that for the $O_2(g)/B(s)$ reaction and comparable to that observed for atomic reactants such as $O(g)$.

Arrhenius plots indicate that the reaction is not elementary over a broad range of conditions and that there may be several different rate-controlling reactions with rather different activation energies. Since there is currently not enough experimental data to speculate on the reaction mechanism, we adopted a rather crude fit to the experimental data which represents an approximate average reaction probability for $T > 1800$ K.

3.5.3 Kinetic Model

A kinetic model was formulated to describe the global reactions given in Table 6 in terms of adsorption and desorption reaction steps. Adsorption steps were generally defined by analogy to observed reaction channels for thermalized, size selected boron ion clusters under single collision conditions. Adsorption enthalpies and, in some cases, desorption activation energies have been defined in terms of the heats of formation for surface complexes. These were estimated using gas phase bond energies as

$$H_1 = \text{heat of formation of } BO(c) \longrightarrow -71.0 \text{ Kcal/mole} \quad (3-29)$$

$$H_2 = \text{heat of formation of } BH(c) \longrightarrow 26.0 \text{ Kcal/mole} \quad (3-30)$$

$$H_3 = \text{heat of formation of } HBO(c) \longrightarrow -45.0 \text{ Kcal/mole} \quad (3-31)$$

$$H_4 = \text{heat of formation of } BCO(c) \longrightarrow -80.0 \text{ Kcal/mole} \quad (3-32)$$

$$H_5 = \text{heat of formation of } B_2O_2(c) \longrightarrow -70.0 \text{ Kcal/mole} \quad (3-33)$$

Adsorption reactions are listed in Table 8. Adsorption enthalpies are expressed in terms of estimated heats of formation for the appropriate surface complex and tabulated JANAF heats of formation for the other reactants. Rate parameters are based on Anderson's B_{12}^+ reaction cross sections and Rosner's MIPES studies. All these reactions are reversible and rate constants for the reverse reaction were computed in the kinetics code using k_{eq} and k_a .

For the reactants $O_2(g)$, $H_2O(g)$, $CO_2(g)$ and $CO(g)$ we have assumed that the dominant product channels correspond to those observed by Anderson's group for B_{12}^+ clusters. The reaction probability per collision is then given by the measured cross section divided by a collision cross section and averaged over a Boltzmann distribution. The temperature dependent reaction probability is then fit to an Arrhenius function, $s=s_0 \times \exp(-E/RT)$.

Anderson's work could not determine neutral gas phase products. Consequently, when more than one product was possible [e.g. $2BO(g)$ versus $B_2O_2(g)$] the most stable products were used.

The last three reactions in Table 8 represent adsorption reactions for gas phase reactants, which are formed by surface reactions. As in the model for B_2O_3 surface reactions, they are included to ensure reversibility and the rates are determined from K_{eq} for the appropriate global reactions.

The desorption steps needed to describe the global reactions given in Table 6 are listed in Table 9 along with estimates of the desorption enthalpy and rate parameters. Since these desorption reactions are all first order in the surface complex, the desorption rate is taken to have the form

$$r_d = A_d \times T \times \exp(-E_d/RT) . \quad (3-34)$$

Table 8 - Boron Surface: Adsorption Reactions

Reaction	k _{max} (cm/sec)	s ₀	E _a (cal/mole)	H _a (Kcal/mole)
B(s) + H(g) = BH(c)	3623	0.1	0.0	H ₂ -52.1
B(s) + O(g) = BO(c)	909	0.8	0.0	H ₁ -59.6
2B(s) + O ₂ (g) = B ₂ O ₂ (c)	643	0.064	1014.0	-109.0
2B(s) + O ₂ (g) = BO(c) + BO(g)	643	0.0082	0.0	H ₁
B(s) + O ₂ (g) = BO(c) + O(g)	643	0.001	1000.0	H ₁ +59.6
B(s) + OH(g) = BO(c) + H(g)	882	0.02	1000.0	H ₁ +42.8
B(s) + OH(g) = HBO(c)	882	0.02	1000.0	H ₃ -9.3
2B(s) + H ₂ O(g) = BH(c) + HBO(g)	857	0.0062	8000.0	H ₂ -2.2
B(s) + BO ₂ (g) = B ₂ O ₂ (c)	556	0.005	5000.0	H ₅ +68.0
B(s) + BO ₂ (g) = BO(c) + BO(g)	556	0.005	5000.0	H ₁ +68.0
B(s) + B ₂ O ₃ (g) = B ₂ O ₂ (g) + BO(g)	436	0.87	0.0	90.8
B(s) + HOBO(g) = HBO(c) + BO(g)	549	0.0025	4000.0	H ₂ +134.0
B(s) + HOBO(g) = B ₂ O ₂ (c) + H(g)	549	0.0025	4000.0	H ₅ +186.1
B(s) + CO ₂ (g) = BO(c) + CO(g)	548	0.0013	4517.0	H ₁ +67.7
B(s) + CO(g) = BCO(c)	687	0.00015	0.0	H ₄ +26.4
B(s) + BO(g) = B ₂ O(c) = BO(c)	Rate computed from K _{eq}			H ₁
B(s) + B ₂ O ₂ (g) = B ₃ O ₂ (c) = B ₂ O ₂ (c)	Rate computed from K _{eq}			H ₅ +109.0
B(s) + HBO(g) = HB ₂ O(c) = HBO(c)	Rate computed from K _{eq}			H ₃ +60.0

The desorption prefactor ($A_d \times T$) was taken to equal the transition state frequency factor ($k_B T/h$) and the activation energy as set equal to the endothermic desorption enthalpy. Rate parameters are not given for those reactions which are the reverse of the adsorption reactions listed in Table 10 since they follow from directly from the equilibrium constant and are computed during execution of the kinetics code. They are included in this Table only to illustrate all the desorption channels included in the model.

Table 9 - Boron Surface: First Order Desorption Reactions

Reaction	H_d (Kcal/mole)	A_d (ps ⁻¹)	E_d (Kcal/mole)
$BH(c) \rightarrow B(s) + H(g)$	52.1-H ₂	Reverse adsorption	
$BO(c) \rightarrow BO(g)$	-H ₁	0.02	-H ₁
$BO(c) \rightarrow B(s) + O(g)$	59.6-H ₁	Reverse adsorption	
$B_2O_2(c) \rightarrow B_2O_2(g)$	-109.0-H ₅	0.02	-109.0-H ₅
$\rightarrow 2B(s) + O_2(g)$	-H ₅	Reverse adsorption	
$\rightarrow B(s) + BO_2(g)$	-68.0-H ₅	Reverse adsorption	
$\rightarrow 2BO(g)$	-H ₅	Neglect	
$HBO(c) \rightarrow HBO(g)$	-60.0-H ₃	0.02	-60.0-H ₃
$\rightarrow BO(g) + H(g)$	52.1-H ₃	0.02	52.1-H ₃
$\rightarrow B(s) + OH(g)$	9.3-H ₃	Reverse adsorption	
$BCO(c) \rightarrow B(s) + CO(g)$	-26.4-H ₄	Reverse adsorption	

There are potentially at least four major channels associated with the desorption of $B_2O_2(c)$, two of which are the reverse of adsorption reactions. The remaining two channels correspond to the product distributions $B_2O_2(g)$ and $2BO(g)$, with the former being approximately 109 Kcal/mole more stable. The thermodynamically favoured $B_2O_2(g)$ was taken as the dominant channel.

To ensure that the global reactions in Table 6 were reversible, a few second order reactions were in the kinetic model. All these reactions are reverse of adsorption reaction in Table 8 so that in model calculations the rate constant is obtained directly from K_{eq} . These reactions are listed in Table 10 to help clarify specifically which second order reactions are currently included in the model.

Table 10 - Boron Surface: Second Order Reactions

Reaction
$BO(c) + H(g) \rightarrow B(s) + OH(g)$
$BO(c) + O(g) \rightarrow B(s) + O_2(g)$
$BO(c) + CO(g) \rightarrow B(s) + CO_2(g)$
$BO(c) + BO(g) \rightarrow 2B(s) + O_2(g)$
$BO(c) + BO(g) \rightarrow B(s) + BO_2(g)$
$HBO(c) + BO(g) \rightarrow B(s) + HBO(g)$
$B_2O_2(c) + H(g) \rightarrow HBO(g)$
$BH(c) + HBO(g) \rightarrow 2B(s) + H_2O(g)$

3.6 References for Section 3.0

- 3-1 Macek, A., "Combustion of Boron Particles at Atmospheric Pressure," Comb. Sci. and Tech. 1, 181 (1969).
- 3-2 Macek, A., "Combustion of Boron Particles: Experiment and Theory," Fourteenth Symp. (Int.) on Comb., pg. 1401, The Combustion Institute, Pittsburgh, PA (1972).
- 3-3 Yetter, R.A., Rabitz, H., Dryer, F.L., Brown, R.C. and Kolb, C.E., "Kinetics of High Temperature B/O/H/C Chemistry," Combustion and Flame 83, 43 (1991).

3-4 Brown, R.C., Kolb, C.E., Yetter, R.A., Dryer, F.L. and Rabitz, H.R., "Development of a Boron Assisted Combustion Model with Sensitivity Analysis," Aerodyne Research, Inc. Final Report No. ARI-RR-580 (1987).

3-5 Page, M., "Multireference Configuration Interaction Study of the Reaction $H_2 + BO \rightarrow HBO$," *J. Phys. Chem.* 93, 3693 (1989).

3-6 JANAF Thermochemical Tables, Third Edition, Parts I and II, *J. of Physical and Chemical Reference Data*, Volume 14 (1985).

3-7 Wedler, G., Chemisorption: An Experimental Approach, Butterworths, (1976).

3-8 Turns, S.R., Holl, J.T., Solomon, A.S.P. and Faeth, G.M., "Gasification of Boron Oxide Drops in Combustion Gases," *Combust. Sci. and Tech.* 43, 287 (1985).

3-9 MacKenzie, J.D., "Structure of Liquid Boron Trioxide," *J. Chem. Phys.* 29, 605 (1958).

3-10 Silver, A.H. and Bray, P.J., "Nuclear Magnetic Resonance Absorption in Glass I. Nuclear Quadrupole Effects in Boron Oxide, Soda Boric Oxide and Borosilicate Glasses," *J. Chem. Phys.* 29, 984 (1958).

3-11 Silver, A.H., "Nuclear Magnetic Resonance in $B_2O_3-H_2O$ Glasses and Boric Acids," *J. Chem. Phys.* 32, 959 (1960).

3-12 Krogh-Moe, J., "Interpretation of the Infrared Spectra of Boron Oxide and Alkali Borate Glasses," *Phys. and Chem. Glasses* 6, 46 (1965).

3-13 Mozzi, R.L. and Warren, B.E., "The Structure of Boron Oxide," *J. Appl. Cryst.* 3, 251 (1970).

3-14 Jellison, Jr., G.E., Panek, L.W., Bray, P.J. and Rouse, Jr., G.B., "Determination of Structure and Bonding in Vireous B_2O_3 by Means of B^{10} , B^{11} , and O^{17} NMR," *J. Chem. Phys.* 66, 802 (1988).

3-15 Miyake, M., Suzuki, T., Morikawa, H., Takayi, and Marumo, F., "Structural Analysis of Molten B_2O_3 ," *J. Chem. Soc. Faraday Trans. 1*, 80, 1925 (1984).

3-16 Elliott, S.R., "A Continuous Random Network Approach to the Structure of Vitreous Boron Trioxide," *Phil. Mag. B* 37, 435 (1978).

3-17 Soules, T.F., "A Molecular Dynamic Calculation of the Structure of B_2O_3 Glass," *J. Chem. Phys.* 73, 4032 (1980).

3-18 Glassman, I., Williams, F.A. and Antaki, P., "A Physical and Chemical Interpretation of Boron Particle Combustion," Twentieth Symposium (International) on Combustion, the Combustion Institute, Pittsburgh, PA (1984).

3-19 Hanley, L., Whitten, J.L. and Anderson, S.L., "Collision-Induced Dissociation and ab Initio Studies of Boron Cluster Ions: Determination of Structures and Stabilities," *J. Phys. Chem.* 92, 5803 (1988).

3-20 Hanley, L. and Anderson, S.L., "Oxidation of Small Boron Clusters Ions (B_{1-13}^+) by Oxygen," *J. Chem. Phys.* 89, 2848 (1988).

3-21 Ruatta, S.A., Hanley, L. and Anderson, S.L., "Dynamics of Boron Cluster Ion Reactions with Deuterium: Adduct Formation and Decay," *J. Chem. Phys.* 91, 226 (1989).

3-22 Hintz, P.A., Ruatta, S.A. and Anderson, S.L., "Interaction of Boron Cluster Ions with Water: Single Collision Dynamics and Sequential Etching," *J. Chem. Phys.* 92, 292 (1990).

3-23 Hintz, P.A. Ruatta, S.A. and Anderson, S.L., "Cluster Based Reaction Probabilities for Boron with Oxygen, Hydrogen, Water, Nitrogen, Nitrous Oxide, Carbon Dioxide, Carbon Monoxide, Methane, Teltrafluoromethane and Silane," Interim Report SBIL-A89, State University of New York, Chemistry Department (1989).

3-24 Gomez, A., Zvuloni, R. and Rosner, D.E., "Flow Reactor Studies of Boron Vaporization and Kinetically-Controlled Oxidation Using Microwave-Induced Plasma Emission Spectroscopy: Preliminary Results," presented at the 1986 Technical Meeting. The Combustion Institute Eastern States Section, Dec. 12, 1986, San Juan, Puerto Rico, and at the Joint Meeting of the French and Italian Section of the Combustion Institute, June 16, 1987, Amalfi, Italy.

3-25 Zvuloni, R., Gomez, A. and Rosner, D.E., "Direct Measurements of the High Temperature Kinetics of Solid Boron Gasification by Its Higher Oxide $B_2O_3(g)$: Chemical Propulsion Implications," *J. Propulsion and Power*, in press (1989).

3-26 Zvuloni, R. and Rosner, D.E., "High Temperature Gasification Rate of Solid Boron In Mixtures of its Highest Oxide $B_2O_3(g)$, and Water Vapor," *AIAA J. Propulsion and Power*, Submitted 1989.

4.0 MODEL RESULTS

4.1 B₂O₃(l) Gasification

The spherical particle combustion model described in Section 2.0 was used to simulate the gasification of a liquid boron oxide droplet injected into high temperature, hydrocarbon combustion environment.

In the flat-flame burner experiments of a single suspended droplet,⁴⁻¹ droplet diameters were on the order of 1000 μm . In contrast, much smaller (20 - 100 μm) boron particles coated with liquid boron oxide have been used to observe ignition characteristics.⁴⁻² In the present model simulations, therefore, the droplet diameter was varied between 50 - 1000 μm to examine the effects of the droplet size. In addition, ambient temperatures between 1600 K and 2200 K were considered. This temperature range covers the observed ignition temperature of particulate boron. The ambient gas mixture composition at three temperatures is presented in Table 13. This data was obtained from equilibrium calculations for a JP4/air mixture with an equivalence ratio of 0.5.

Table 13 - The Ambient Mixture Compositions in Mole Fractions Obtained from Equilibrium Calculation of a JP-4/Air Mixture with an Equivalence Ratio of 0.5

Temperature	1600 K	1800 K	2000 K
O	0.0005%	0.004%	0.02%
OH	0.019%	0.05%	0.14%
O ₂	10%	10%	10%
H ₂ O	6.8%	6.8%	6.7%
CO ₂	6.8%	6.8%	6.8%

Temporal variations of the gasification rate and surface species concentrations for a 50 μm boron oxide droplet and an ambient temperature of 1800 K are presented in Figure 4.1. Figure 4.1 shows that the initial transient period is relatively short; less than 0.05% of the particle's lifetime t_f . Additional model simulation results confirmed this observation for the range of conditions treated here. Thus, only the quasi-steady state behavior will be discussed hereafter and all model results for gasification rates, surface chemical species concentrations, gas phase species concentrations, temperatures, etc. are the quasi-steady state values unless otherwise noted.

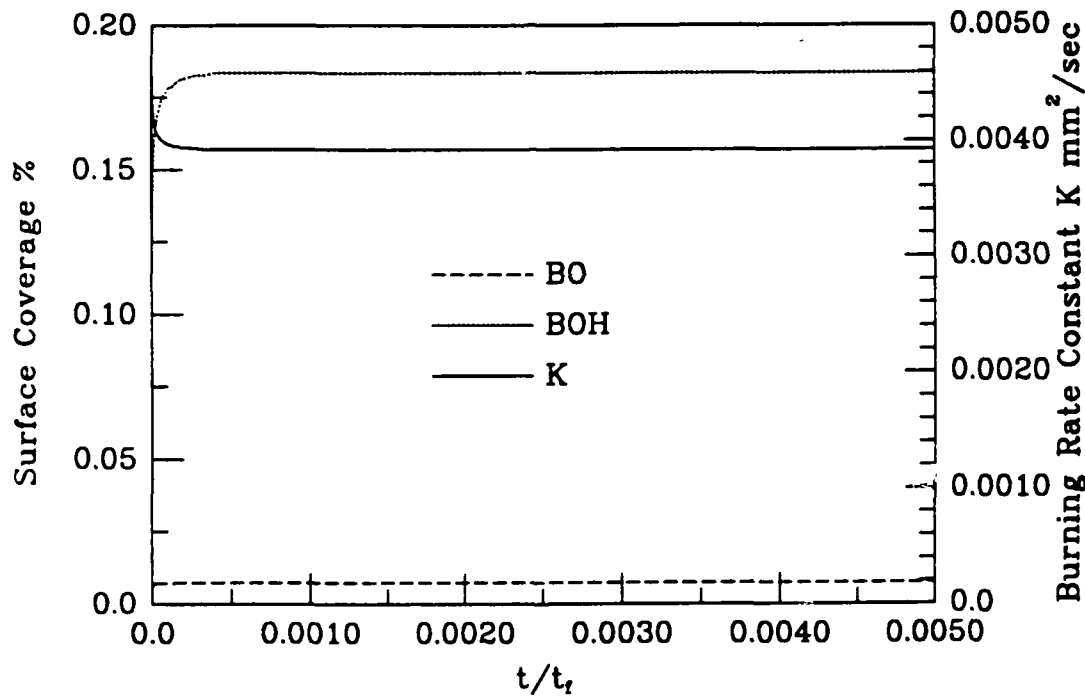


Figure 4.1. Temporal Variation of the $\text{B}_2\text{O}_3(\ell)$ Gasification Rate and Percent Surface Coverage By Adsorption Products for a 50 μm Particle at an Ambient Temperature of 1800 K. t_f denotes the droplet lifetime.

Figures 4.2 and 4.3 show the gasification rates due to vaporation and surface reactions with H_2O/OH versus droplet diameter for four ambient temperatures. These plots can be used to identify rate controlling steps since the gasification rate stays constant in the diffusion controlled regime and is linearly proportional to the particle diameter in the kinetically controlled regime. At ambient temperatures of 1600 K and 1800 K, Figure 4.2 shows that gasification by surface chemical reactions is kinetically controlled for particles smaller than 200 μm . As the particle's diameter increases, the diffusion process slows down and eventually becomes the rate controlling step. In contrast, gasification by the physical evaporation is always diffusion controlled.

The gasification rates as a function of particle diameter for ambient temperatures of $T = 2000$ K and $T = 2200$ K are shown in Figure 4.3. In contrast to the low ambient temperature cases ($T = 1600$ and 1800 K) presented in Figure 4.2, at these higher temperatures the evaporation gasification rate increases sharply for particle diameters less than 200 μm . This is due to the strong effect of the surface temperature on evaporation and not to changes in the rate-controlling steps. Analogous to the low temperature cases, gasification by surface reactions is kinetically limited while the gasification by the evaporation is diffusion limited for small particles. Therefore, as the particle diameter decreases, the heat loss per unit area due to the surface reactions stays the same but the diffusional heat transfer from the ambient to the particle increases. As a result, the surface temperature increases as the particle diameter decreases. This surface temperature increase is large enough to increase the physical evaporation rate substantially under high ambient temperature conditions.

Figures 4.2 and 4.3 also show that as the ambient temperature increases, gasification by the physical evaporation is accelerated faster than gasification by the surface reactions. This is due to differences in the associated activation energies.

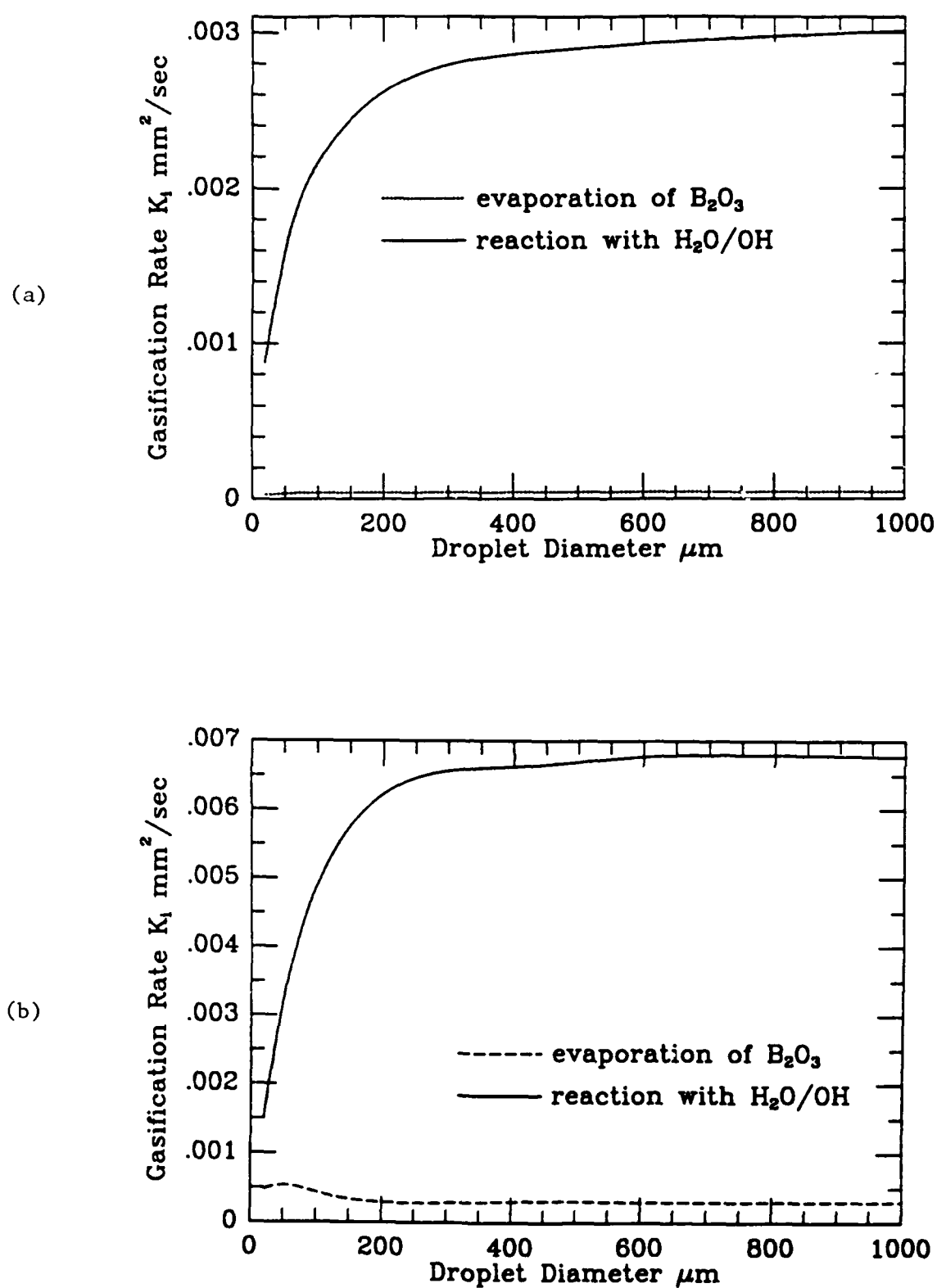


Figure 4.2. Calculated $\text{B}_2\text{O}_3(\ell)$ Gasification Rates Due to Surface Reaction and Physical Evaporation as a Function of Particle Diameter at Ambient Temperatures of (a) 1600 K and (b) 1800 K

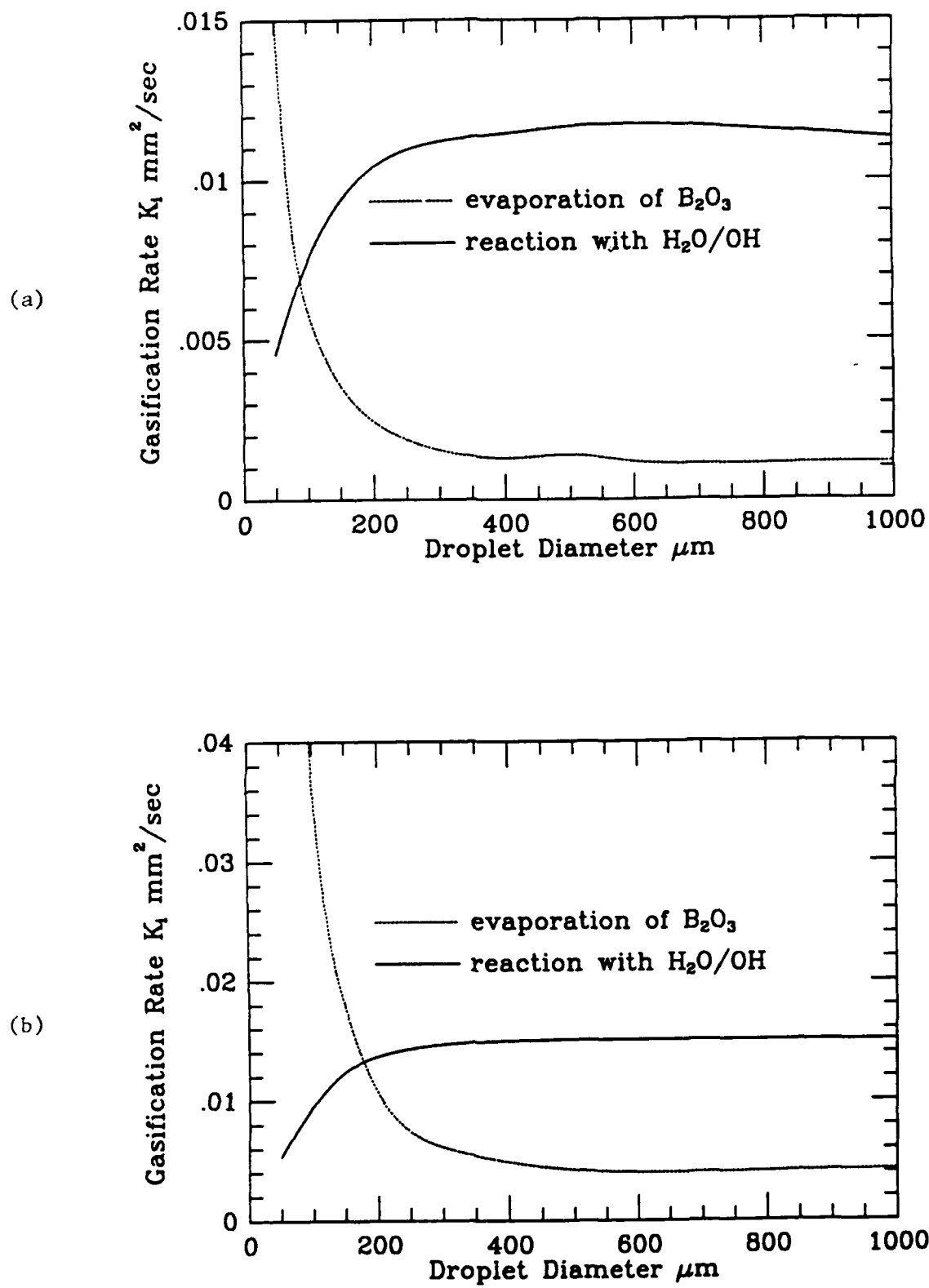


Figure 4.3. Calculated $\text{B}_2\text{O}_3(l)$ Gasification Rates Due to Surface Reaction and Physical Evaporation as a Function of Particle Diameter at Ambient Temperatures of (a) 2000 K and (b) 2200 K

Figures 4.2 and 4.3 also demonstrate that gasification by the surface reactions dominates over over the physical evaporation. This is especially true for larger particles where both mechanisms are diffusion controlled. However, gasification by the surface reactions becomes slower as the particle diameter decreases. Figure 4.3 shows that physical evaporation is more important than surface reactions in gasifying the small droplets ($< 100 \mu\text{m}$) at temperatures above 2000 K. Consequently, experimental results obtained for $1000 \mu\text{m}$ particles by Turns et al.⁴⁻¹ should be interpreted very carefully, because their conclusions about the relative importance of surface reactions may not be directly applicable to smaller particles.

The overall gasification rate are obtained by simply adding the individual gasification rates due to surface reactions and physical evaporation. Figure 4.4 shows the overall gasification rate as a function of particle diameter for ambient temperatures of 1600 K, 1800 K, 2000 K and 2200 K. For large particles ($> 200 \mu\text{m}$), gasification is diffusion limited and the overall gasification rates are independent of particle diameter. For small particles ($< 200 \mu\text{m}$), gasification is kinetically limited for the low ambient temperatures ($T = 1600 \text{ K}$ and 1800 K), but deviates considerably from the d^1 behavior for the high ambient temperatures ($T = 2000 \text{ K}$ and 2200 K). This deviation from d^1 behavior is caused by the increased contribution from physical evaporation as shown in Figure 4.3.

Gas phase chemical species and temperature profiles are shown in Figure 4.5 for particle diameters of $50 \mu\text{m}$ and $500 \mu\text{m}$ and an ambient temperature of 1800 K. The boron containing species, $\text{BO}_2(\text{g})$, $\text{B}_2\text{O}_3(\text{g})$, and $\text{HOBO}(\text{g})$ are mainly produced from liquid boron oxide surface reactions and thus have their maximum values near the surface. $\text{BO}_2(\text{g})$ shows the largest decrease with distance from the surface, and the fall off is particularly sharp for the $500 \mu\text{m}$ diameter particle (Figure 4-5b). This is because for large particles, diffusion mass transfer is slow relative to the homogeneous gas phase

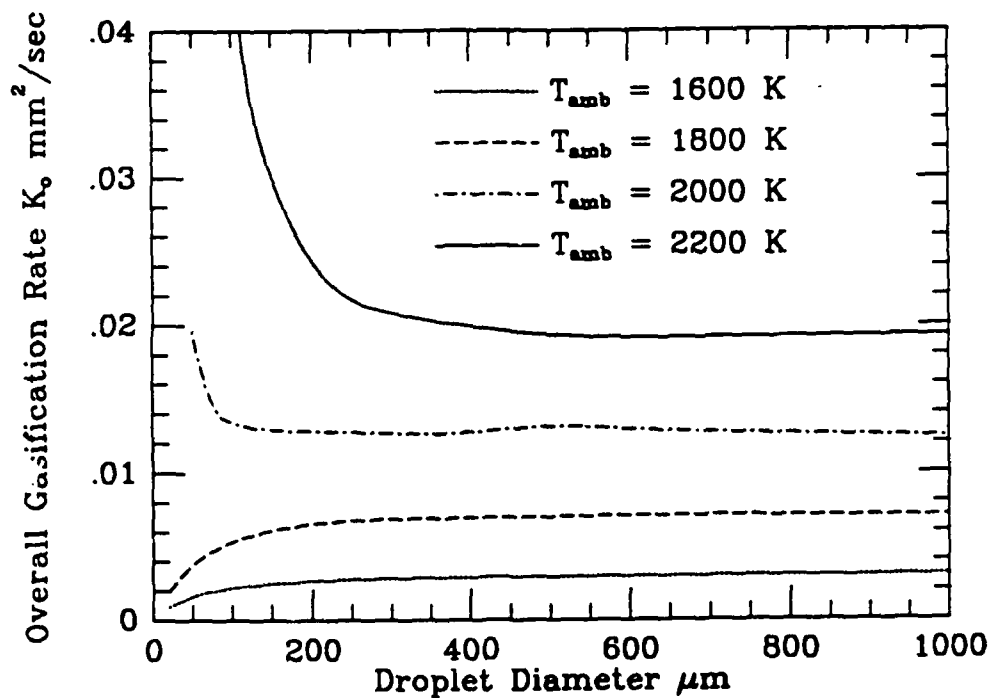


Figure 4.4. Calculated Overall $\text{B}_2\text{O}_3(\ell)$ Gasification Rates as a Function of Particle Diameter at Ambient Temperatures of 1600 K, 1800 K, 2000 K, and 2200 K.

chemistry that converts $\text{BO}_2(\text{g})$ to HOBO and $\text{B}_2\text{O}_3(\text{g})$. The higher concentrations of $\text{BO}_2(\text{g})$ and $\text{HOBO}(\text{g})$ at the surface of the 500 μm diameter particle are also due to slower diffusion mass transfer rates. In contrast, the $\text{B}_2\text{O}_3(\text{g})$ concentration at the surface of the 500 μm diameter particle is found to be lower than that of the 50 μm diameter particle because of the lower surface temperature.

As listed in Section 3.0, the surface reaction mechanisms used in the present work consist of adsorption, reaction between adsorbed species and desorption. The reaction fluxes from each elementary step are presented in Figures 4.6, 4.7, and 4.8. These reaction fluxes can be used to identify major pathways.

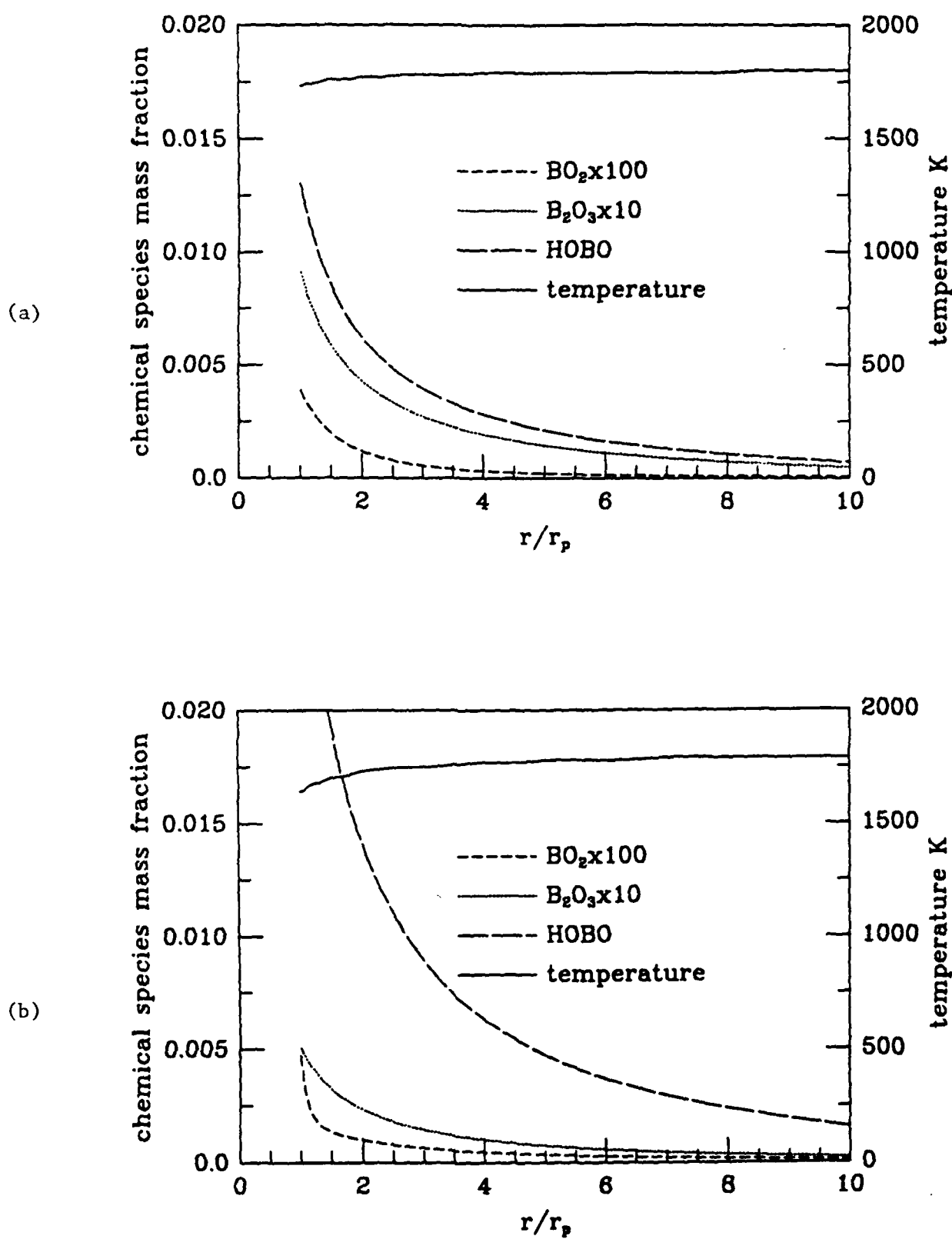


Figure 4.5. Radical Species Mass Fraction and Temperature Profiles for an Ambient Temperature of 1800 K and Droplet Diameter of (a) 50 μm and (b) 500 μm .

Adsorption and desorption fluxes as a function of particle diameter are shown in Figures 4.6 and 4.7. As the droplet diameter increases, the adsorption fluxes of HOBO(g) and the desorption fluxes of $>B-OH(c)$ increase rapidly in the kinetically controlled regime and increase only slightly in the diffusion controlled regime. They also increase rapidly as the ambient temperature increases. Even though the adsorption of HOBO(g) has the largest adsorption flux, the desorption of $>B-OH(s)$ is also fast enough to return HOBO molecules back to the gas phase. The adsorption of $H_2O(g)$ appears to have the largest flux next to that of HOBO. As shown in Table 4, the adsorption of one $H_2O(g)$ molecule creates two surface species $>B-OH(c)$ which desorb to produce two molecules of HOBO(g). The adsorption flux of O(g) atom and $BO_2(g)$, as well as the desorption flux of $>BO(c)$ is small for the given ambient conditions in which the concentration O(g) is much smaller than that of OH(g) or $H_2O(g)$. Because of the abundance of OH(g) and $H_2O(g)$ in the ambient environment, the desorption of $>B-OH$ is the dominant desorption pathway in gasifying liquid boron oxides. This is shown in Figure 4.7.

The reaction fluxes for second order reactions between two surface species are shown in Figure 4.8. They were found to be one order of magnitude smaller than the reaction fluxes for adsorption or desorption. Furthermore, the calculated surface coverage by the adsorbed species are very small (< 1%) as shown in Figure 4.9. This is because desorption is sufficient (relative to adsorption) to keep the surface coverage low.

Sensitivity analysis is a useful tool in identifying important input parameters in determining physically important output parameters. In the present work, a parameter sensitivity coefficient of the gasification rate with respect to surface kinetic rate constants was used to measure the response of the gasification rate to variation in the surface reaction rate parameters. This analysis showed that the rate parameters associated with $H_2O(g)$ and OH(g) adsorption, $>B-OH(s)$ desorption and the second order reaction $>B-OH + >B-OH$ are important in determining gasification rate. Figure 4.10 displays sensitivity coefficient profiles for these important rate parameters as a function of droplet diameter for an ambient temperature 1800 K.

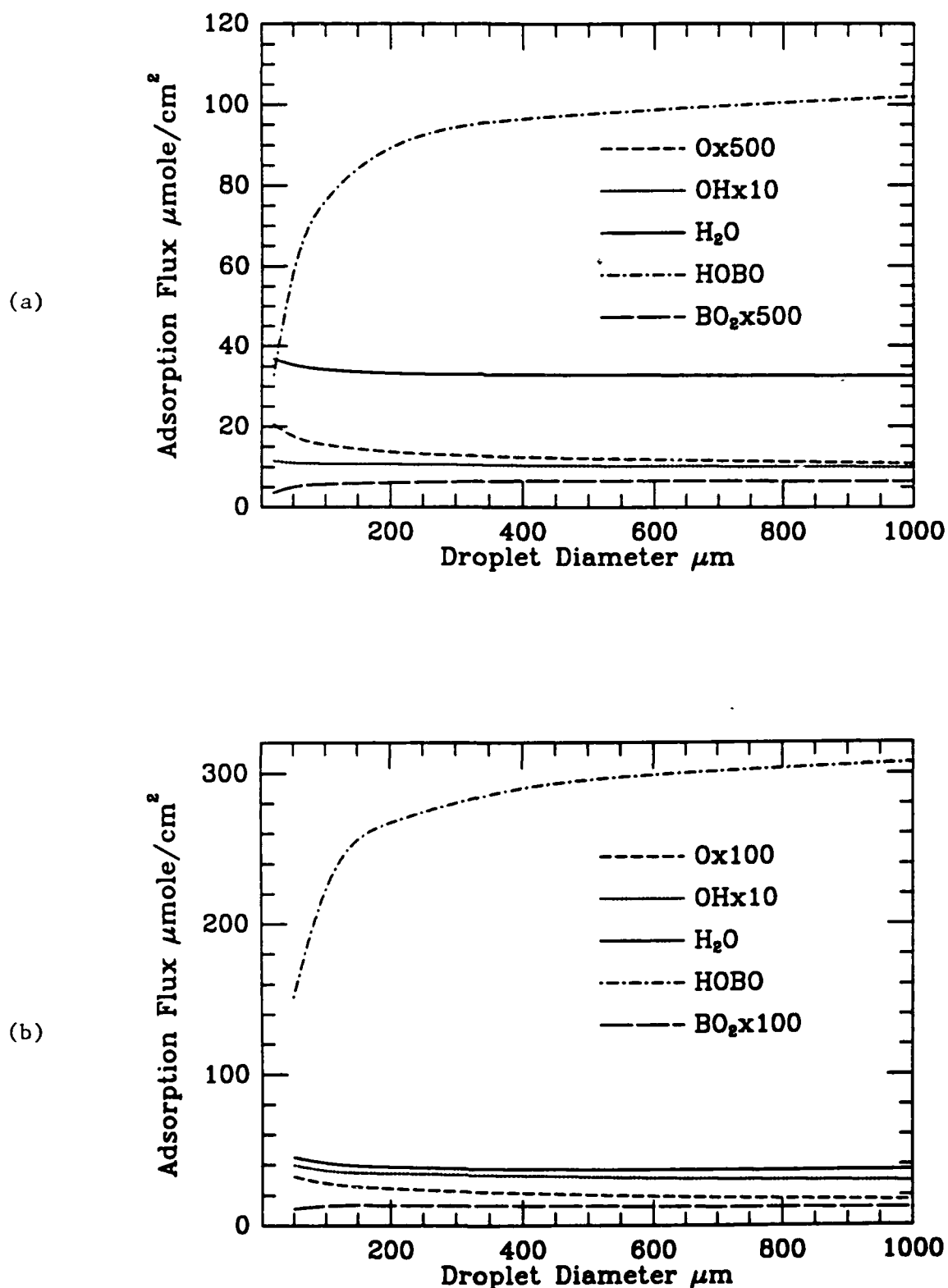
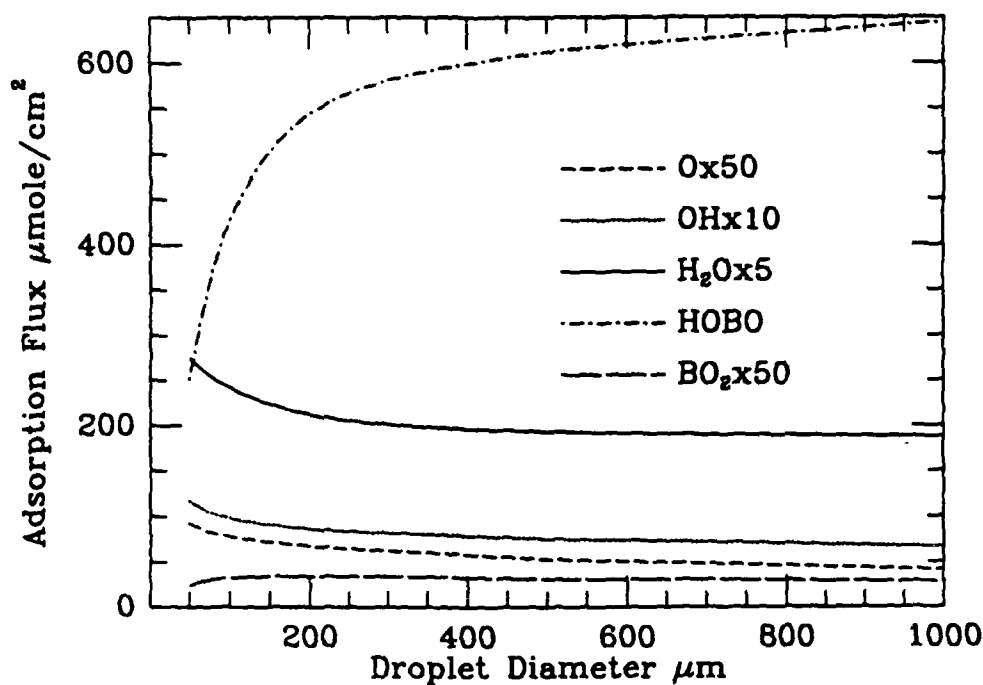


Figure 4.6. Adsorption Fluxes as a Function of Droplet Diameters for Ambient Temperatures of (a) 1600 K, (b) 1800 K, (c) 2000 K and (d) 2200 K

(c)



(d)

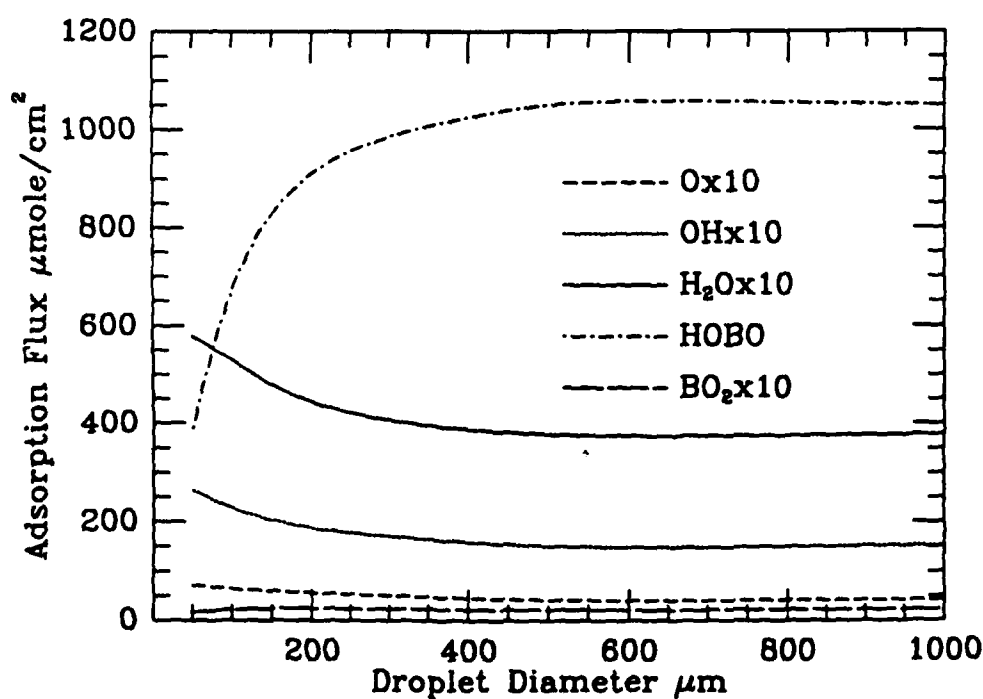


Figure 4.6. Adsorption Fluxes as a Function of Droplet Diameters for Ambient Temperatures of (a) 1600 K, (b) 1800 K, (c) 2000 K and (d) 2200 K (Continued)

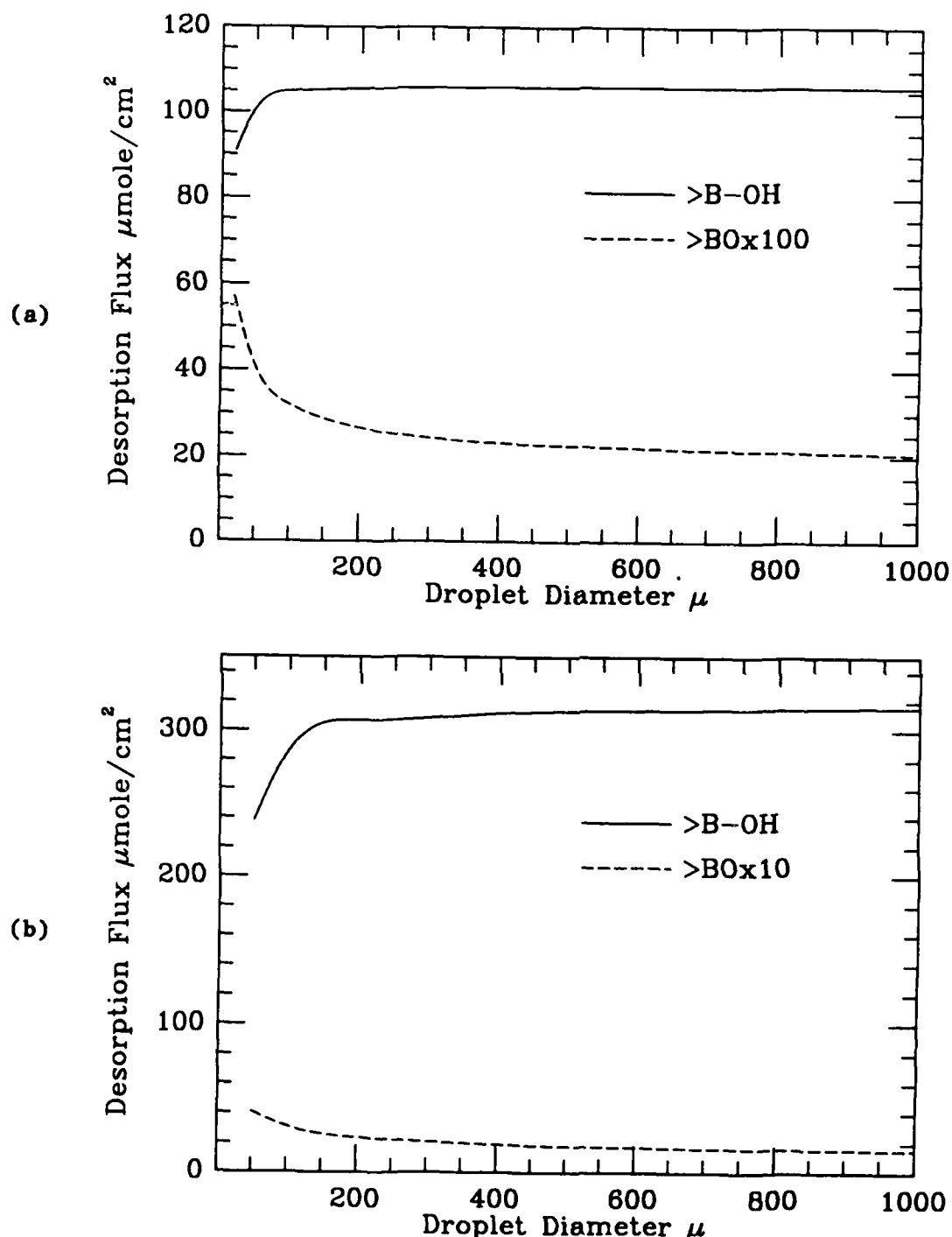


Figure 4.7. Desorption Fluxes as a Function of Droplet Diameters for Ambient Temperatures of (a) 1600 K, (b) 1800 K, (c) 2000 K and (d) 2200 K.

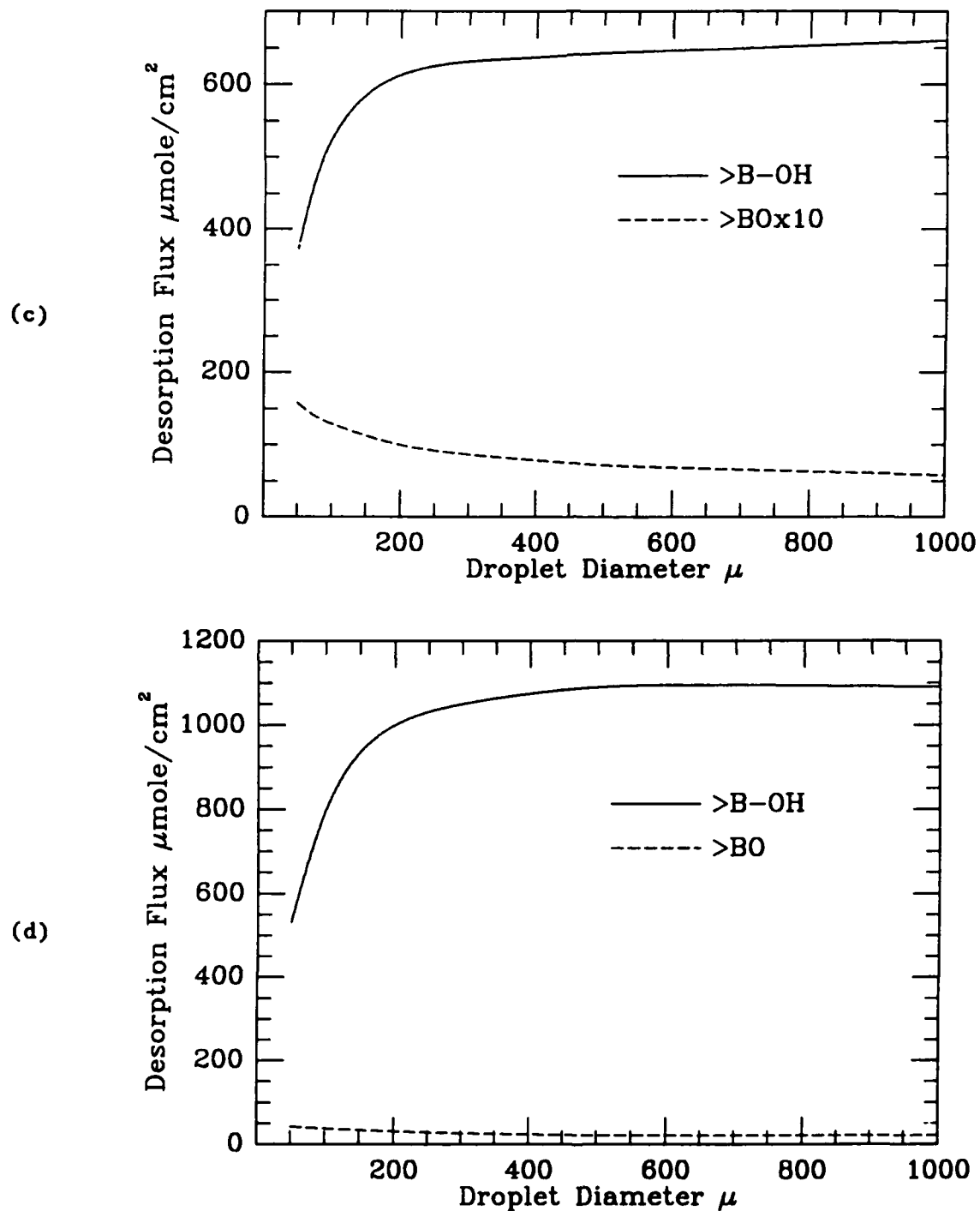
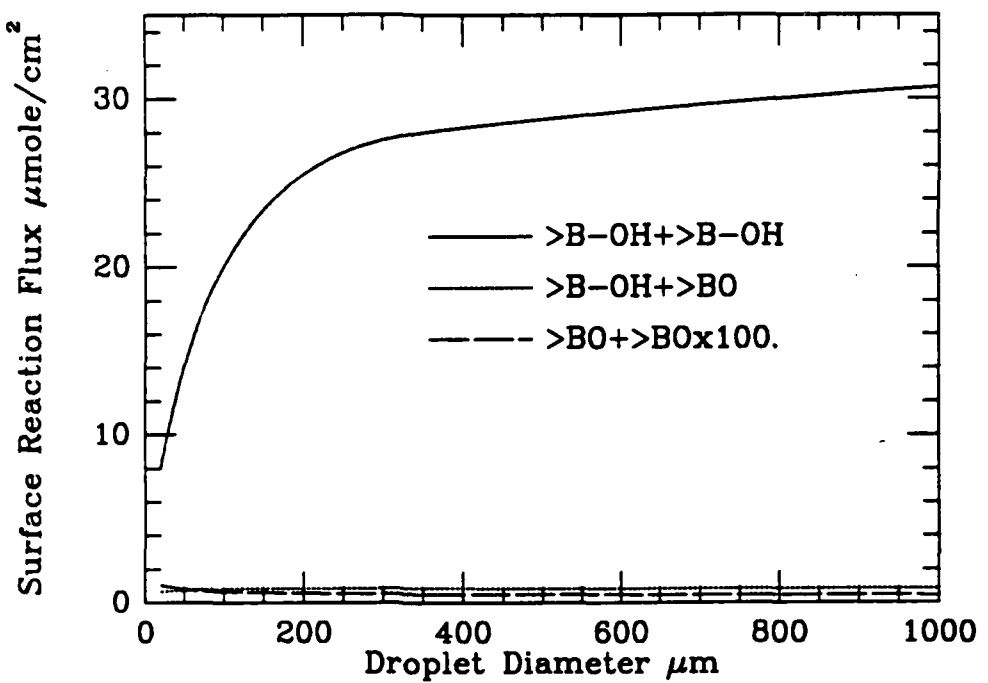


Figure 4.7. Desorption Fluxes as a Function of Droplet Diameters for Ambient Temperatures of (a) 1600 K, (b) 1800 K, (c) 2000 K and (d) 2200 K (Continued)

(a)



(b)

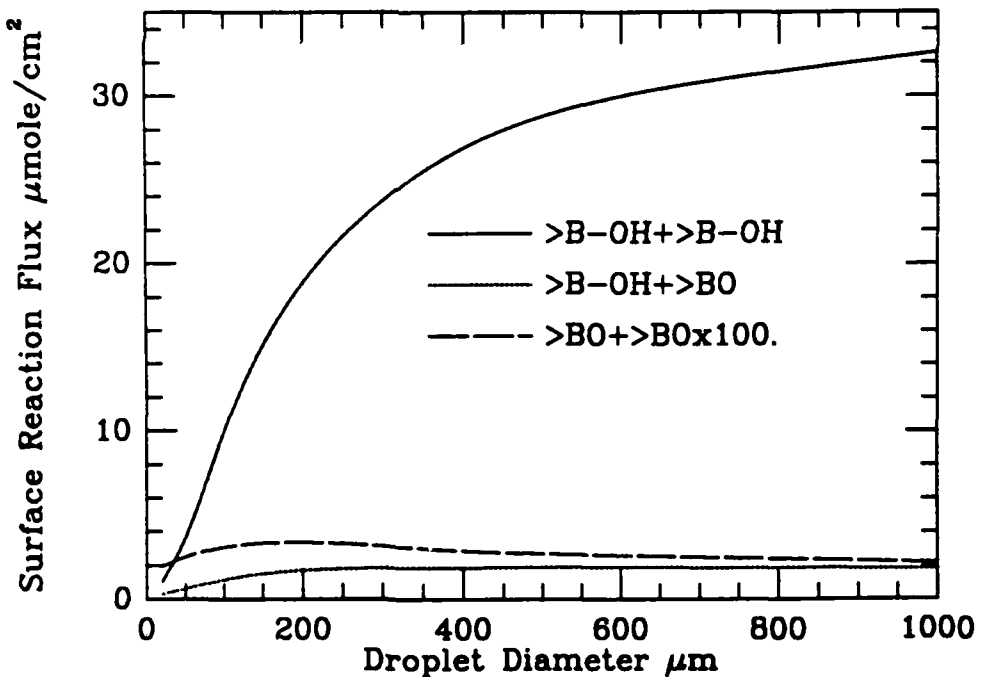
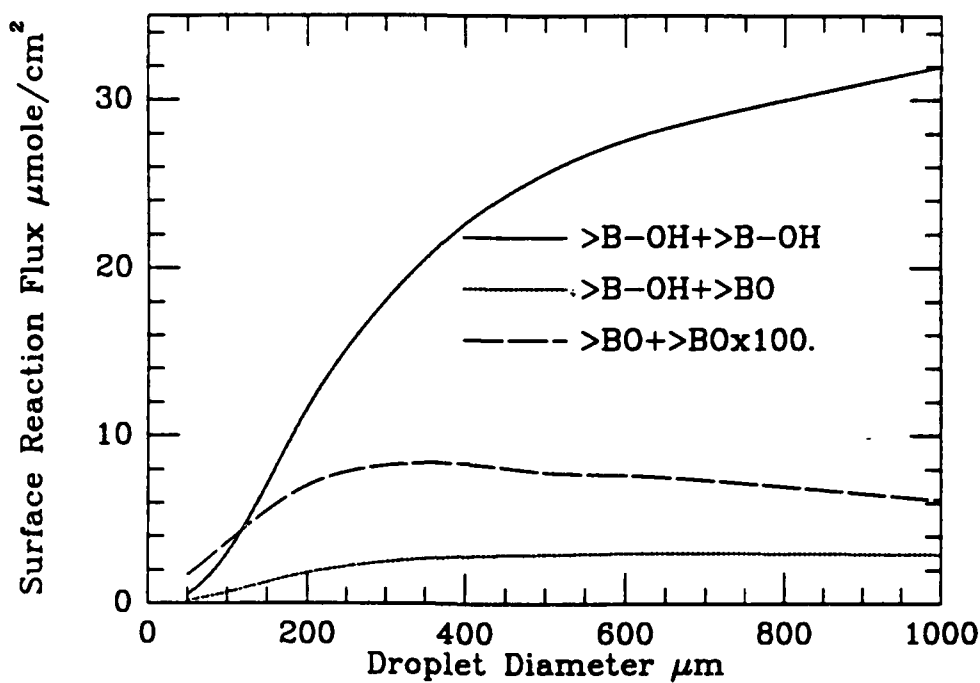


Figure 4.8. Surface Reaction Flux as a Function of Droplet Diameter for Ambient Temperatures of (a) 1600 K, (b) 1800 K, (c) 2000 K and (d) 2200 K

(c)



(d)

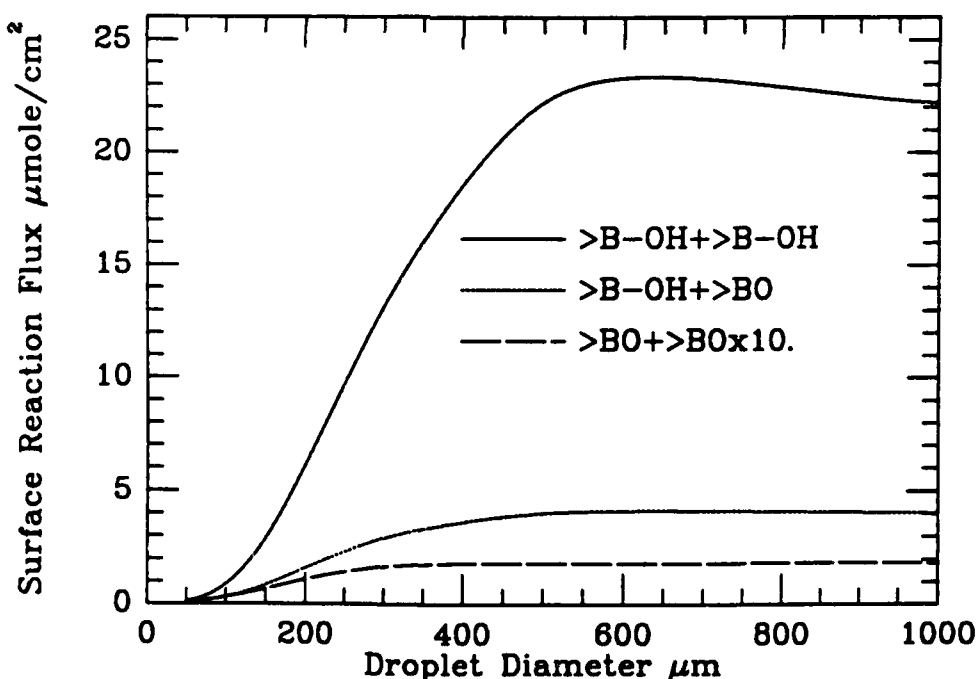


Figure 4.8. Surface Reaction Flux as a Function of Droplet Diameter for Ambient Temperatures of (a) 1600 K, (b) 1800 K, (c) 2000 K and (d) 2200 K (Continued)

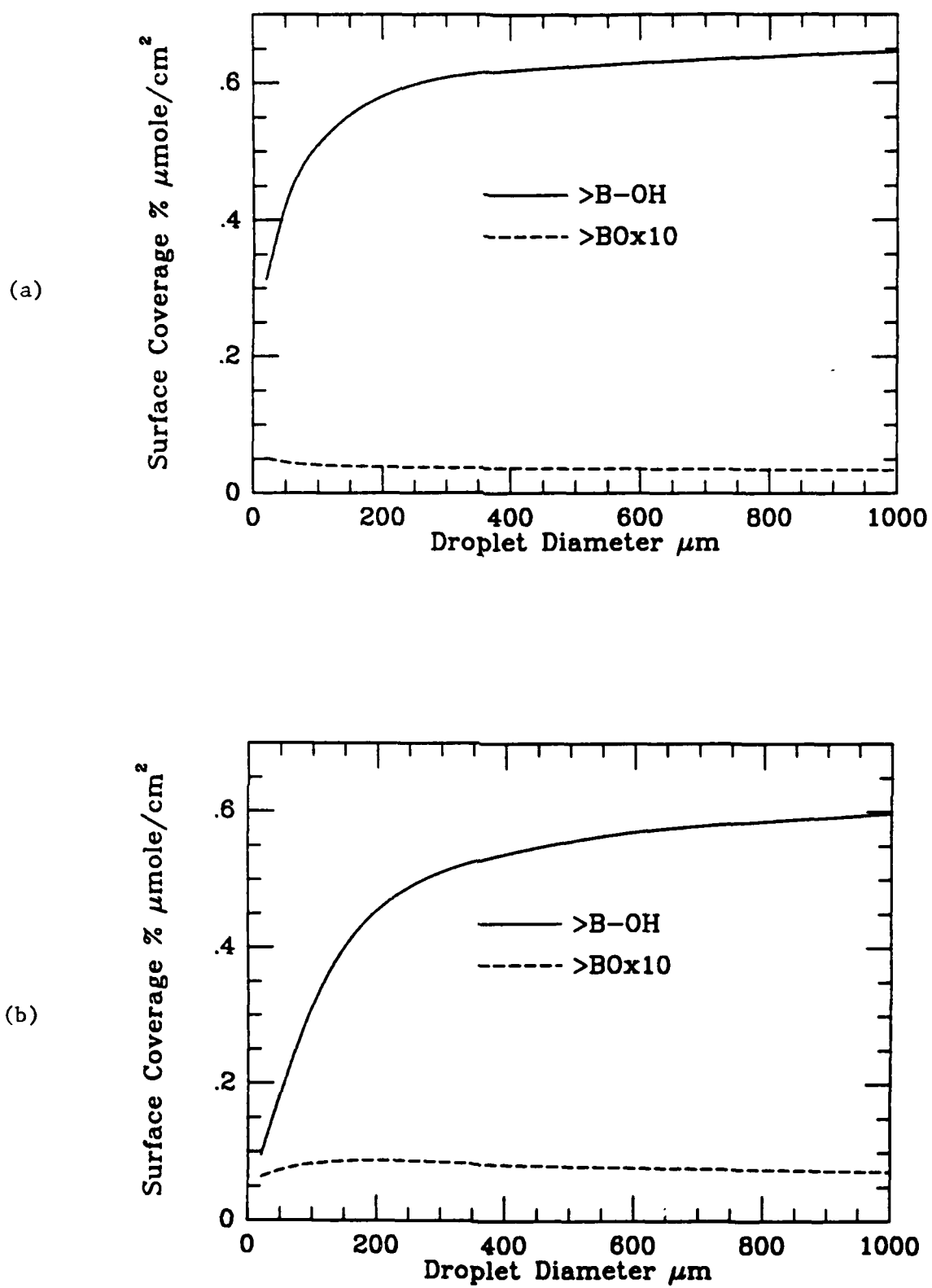
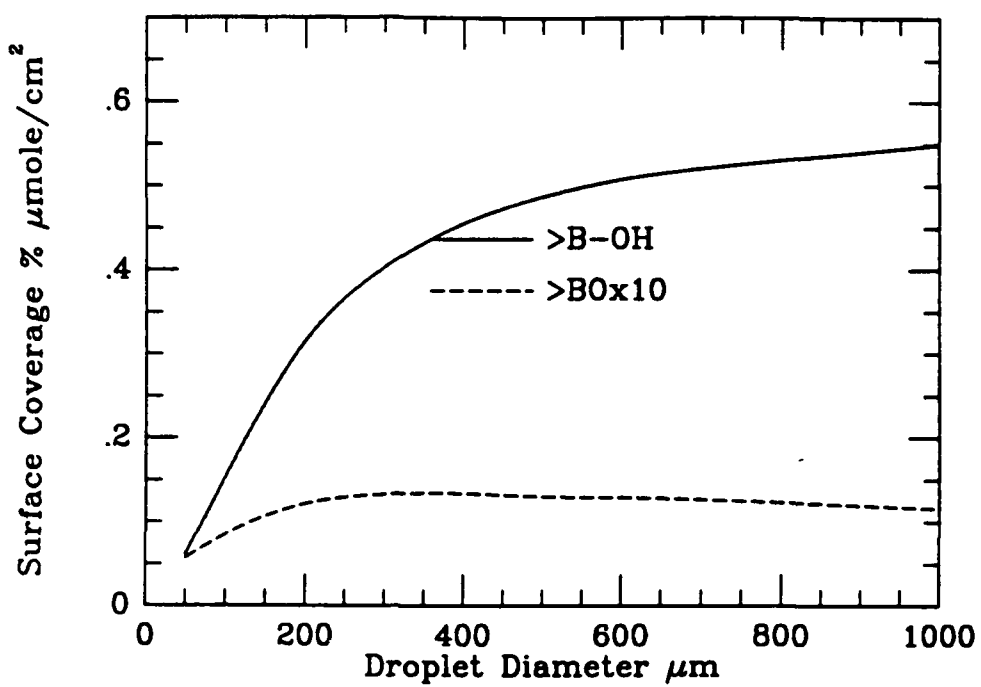


Figure 4.9. Percentage Surface Coverage as a Function of Droplet Diameter for Ambient Temperatures of (a) 1600 K, (b) 1800 K, (c) 2000 K and (d) 2200 K

(c)



(d)

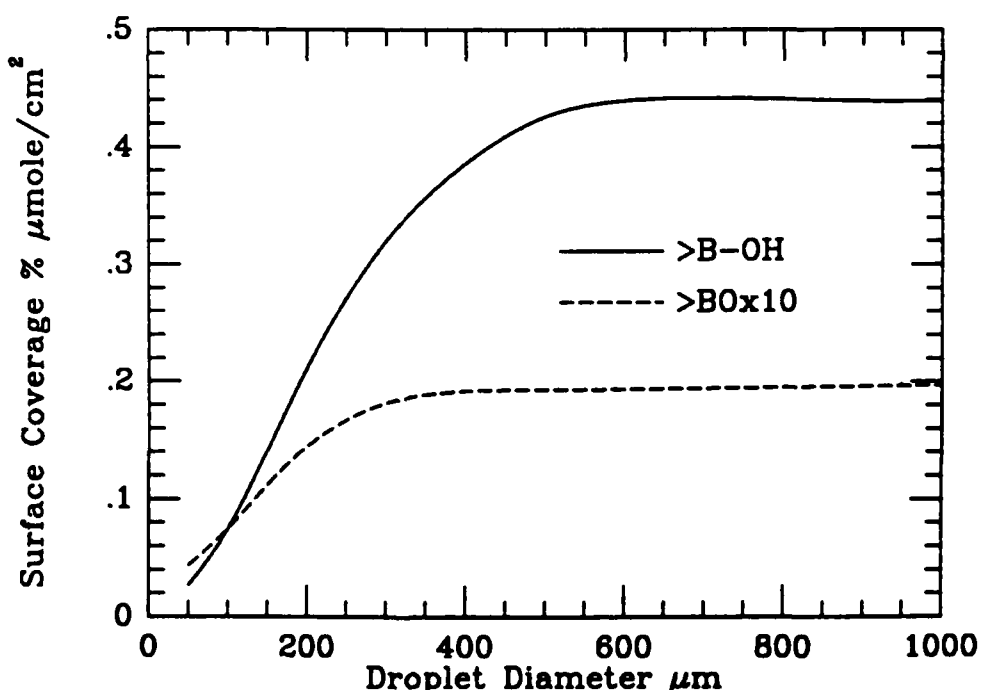


Figure 4.9. Percentage Surface Coverage as a Function of Droplet Diameter for Ambient Temperatures of (a) 1600 K, (b) 1800 K, (c) 2000 K and (d) 2200 K (Continued)

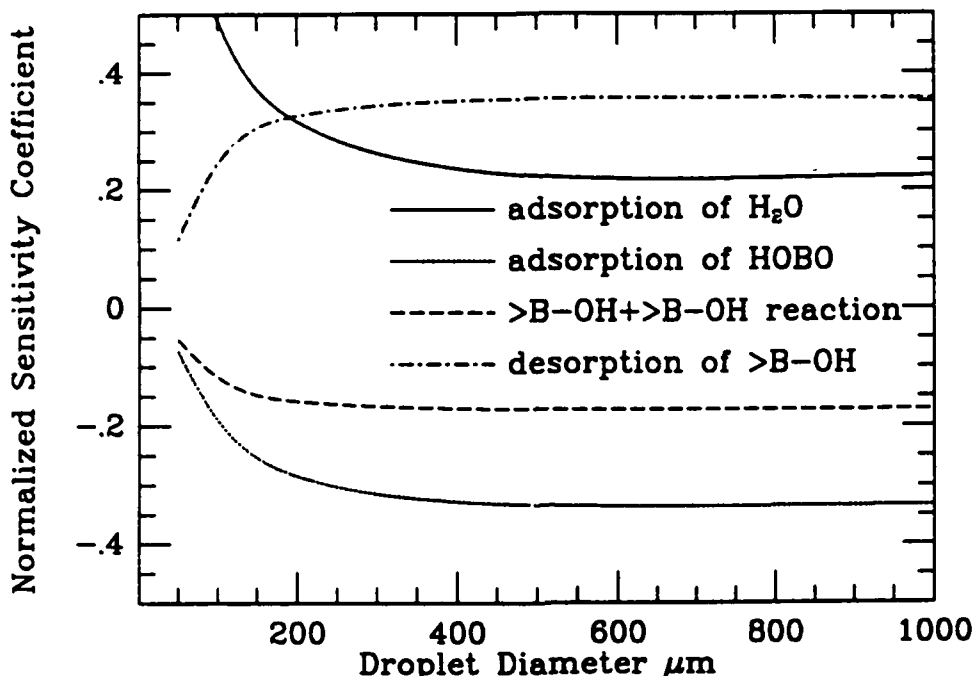


Figure 4.10. Sensitivity Coefficient Profiles as a Function of Droplet Diameter for an Ambient Temperature of 1800 K

4.2 High Temperature Particulate Boron Oxidation

The section presents model results for the oxidation of 200 μm solid boron particle in a hydrocarbon combustion environment using the surface reactions and rate parameters described in Section 3.5. The same ambient mixture composition (Table 13 in Section 4.1) used in the model simulations of liquid B_2O_3 gasification was also used to treat particulate boron oxidation. Model results are presented here for two cases corresponding to ambient temperatures of 1400 K and 2000 K.

For the simulations described here, the particle radius was kept fixed in order to explicitly examine the steady-state behavior. The burning rates for the two cases studied are presented in Figure 4-11. The transient period prior to steady-state conditions is clearly evident. The final time, t_f , in this figure was chosen as 10 sec. It is seen that for both $T_{\text{amb}} = 1400$ K and 2000 K, a steady-state is reached within 12 msec. Figure 4-11 also indicates

that the burning rate is only weakly dependent on the ambient temperature. In particular, a 600 K increase in the ambient temperature only increases the burning rate constant by ca. 11%.

Temperature profiles are shown in Figure 4-12. These profiles indicate a temperature at the particle surface that is between 600 K and 700 K higher than the ambient. This difference is primarily dictated by surface reaction enthalpies and, consequently, subject to the current uncertainties in thermochemical parameters. The temperature profiles for both cases treated decrease monotonically with radial distance from surface and fall to within 100 K of the ambient temperature within nine particle radii.

Radial profiles of the species mass fractions for $T_{amb} = 1400$ K are shown in Figure 4-13. It is readily seen that the mass fractions for gas phase oxidizers decrease near the particle surface. Although gas phase chemistry may play some role in this behavior, the decrease is primarily attributable to reactions at the surface. Consequently, the extent of this decrease can be

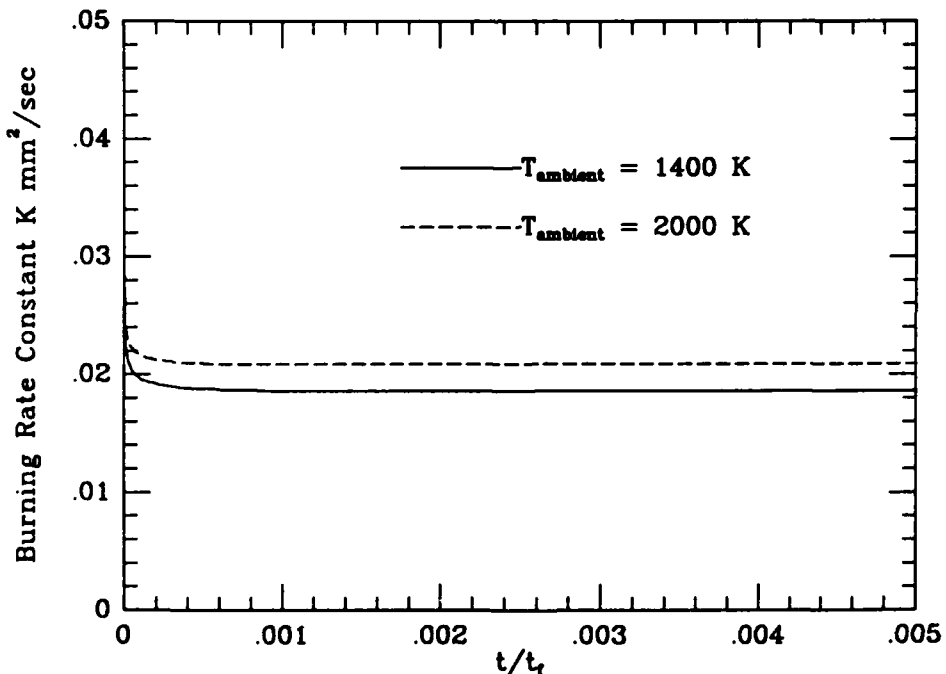


Figure 4.11. Calculated B(s) Burning Rate Constant for an Ambient Temperature of 1400 K and 2000 K

used as a qualitative criterion for judging the relative oxidizing strength of the various gas phase reactants. On this basis, the model results agree qualitatively with observed experimental reaction probabilities. In particular, $O(g)$, $OH(g)$ and $B_2O_3(g)$ are seen to be relatively strong particulate boron oxidizing agents, while $CO_2(g)$, $O_2(g)$ and $H_2O(g)$ are relatively moderate. $HOBO(g)$ was clearly found to be the least effective gas phase reactant, however, there is little experimental rate data for $B(s)/HOBO(g)$ reactions currently available and the estimated rate parameters given in Section 3.0 are highly uncertain. In addition, because the $HOBO(g)$ mass fraction is significantly larger than the mass fractions of other potential reactants, it may be an important oxidizing species even if its rate constant is relatively small.

The mass fractions for surface reaction products $BO_2(g)$, $CO(g)$, $BO(g)$, $B_2O_3(g)$, $HBO(g)$, $H(g)$ and $H_2(g)$ all show pronounced peaks at the surface. The species containing boron, however, decrease rather sharply and, with the exception of $BO_2(g)$, are negligible beyond one particle radius ($200 \mu m$) from the surface. This is the consequence of homogenous gas phase chemistry which converts boron sub-oxides and oxyhydrides to the primary boron oxidation products $HOBO(g)$ and $B_2O_3(g)$. Here there is good agreement with previous homogeneous oxidation model results which indicated that surface products were quickly converted to $HOBO(g)$ and $B_2O_3(g)$. Similarly, the indication in Figure 4-13 that $HOBO(g)$ tends to peak closer to the surface than $B_2O_3(g)$ is a consequence of the gas phase chemistry model which was shown to predict that $HOBO(g)$ was formed more rapidly by gas phase reactions than $B_2O_3(g)$.⁴⁻³

Radial profiles of the species mass fractions for $T_{amb} = 2000$ K are shown in Figure 4-14. In general, the mass fraction profiles exhibit the same trends as described above for the case corresponding to $T_{amb} = 1400$ K. The most notable difference is the decrease in the $HOBO(g)$ mass fraction and a corresponding increase in the $B_2O_3(g)$ mass fraction. This behavior is a direct consequence of the gas phase chemistry which was found in earlier modeling work to show a shift towards $B_2O_3(g)$ with higher ambient temperatures.

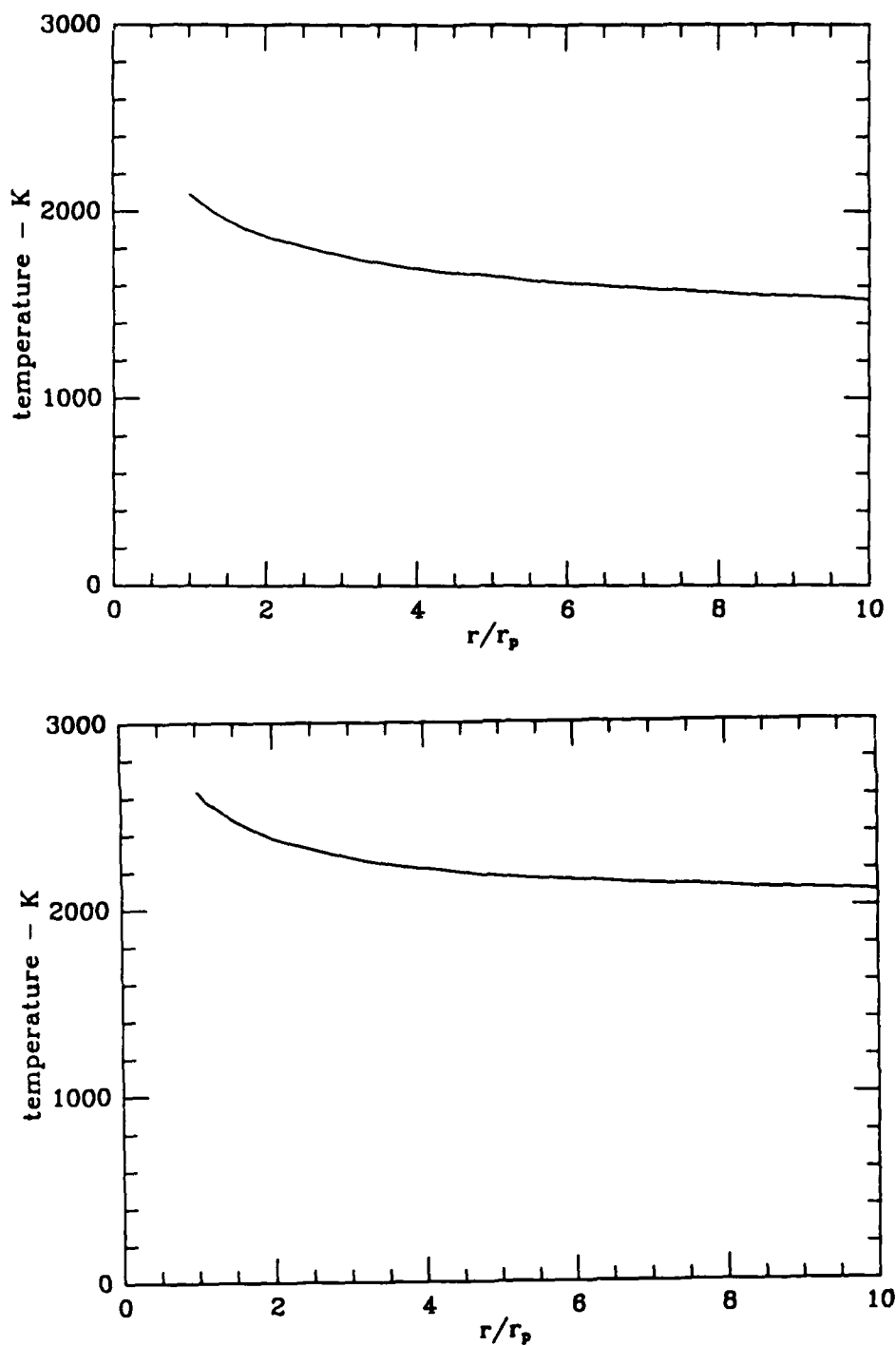


Figure 4.12. Particulate Boron Oxidation Temperature Profiles for an Ambient Temperature of (a) 1400 K and (b) 1500 K

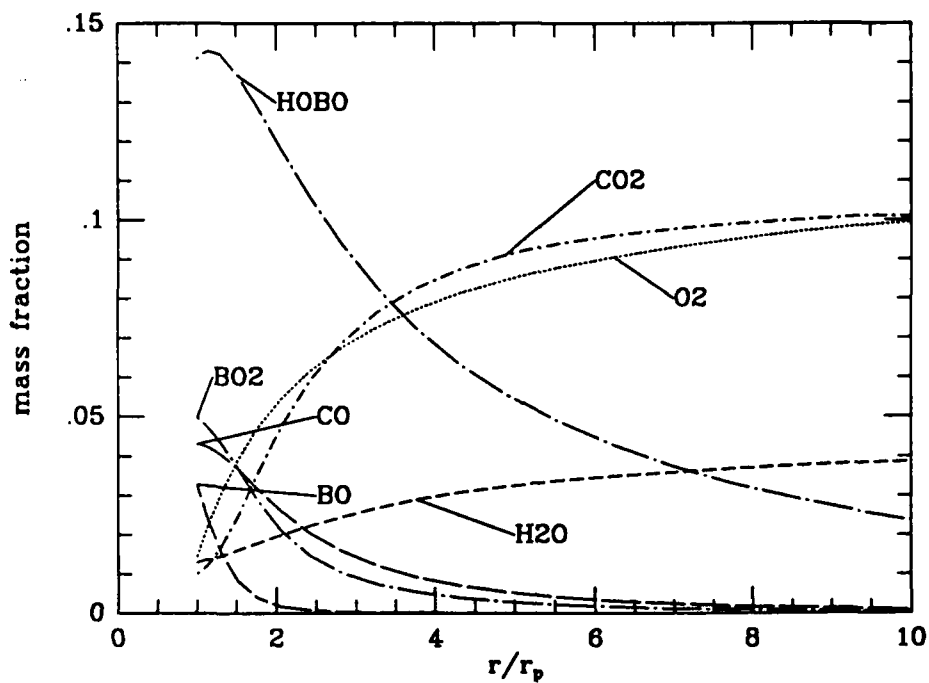


Figure 4.13. Species Mass Fraction Radial Profiles for the Oxidation of a 200 μm Spherical Boron Particle in a JP4/air Mixture at an Ambient Temperature of 1400 K

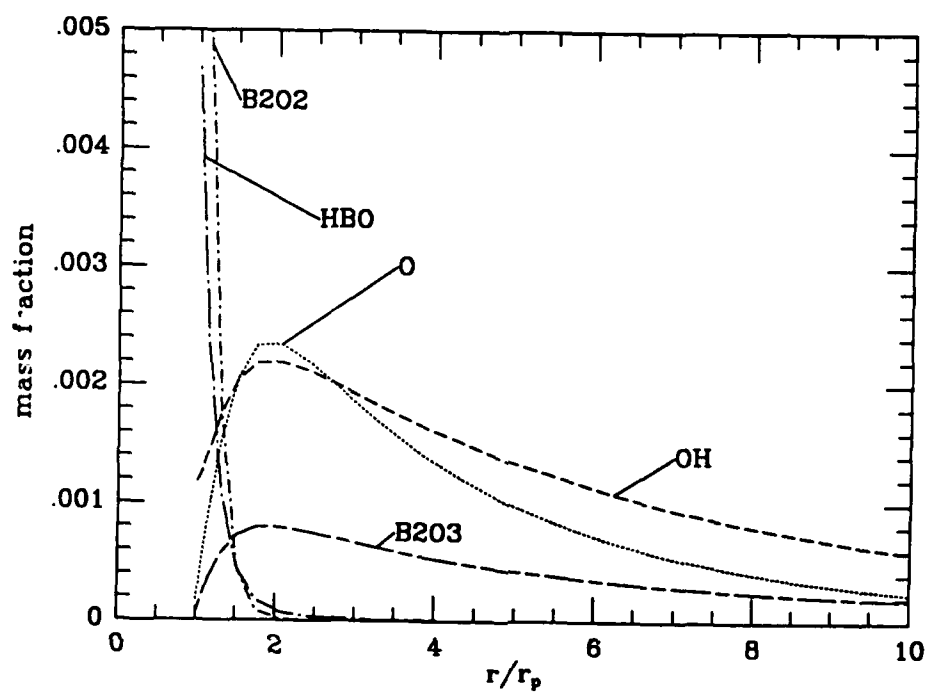


Figure 4.13. Species Mass Fraction Radial Profiles for the Oxidation of a 200 μm Spherical Boron Particle in a JP4/air Mixture at an Ambient Temperature of 1400 K (Continued)

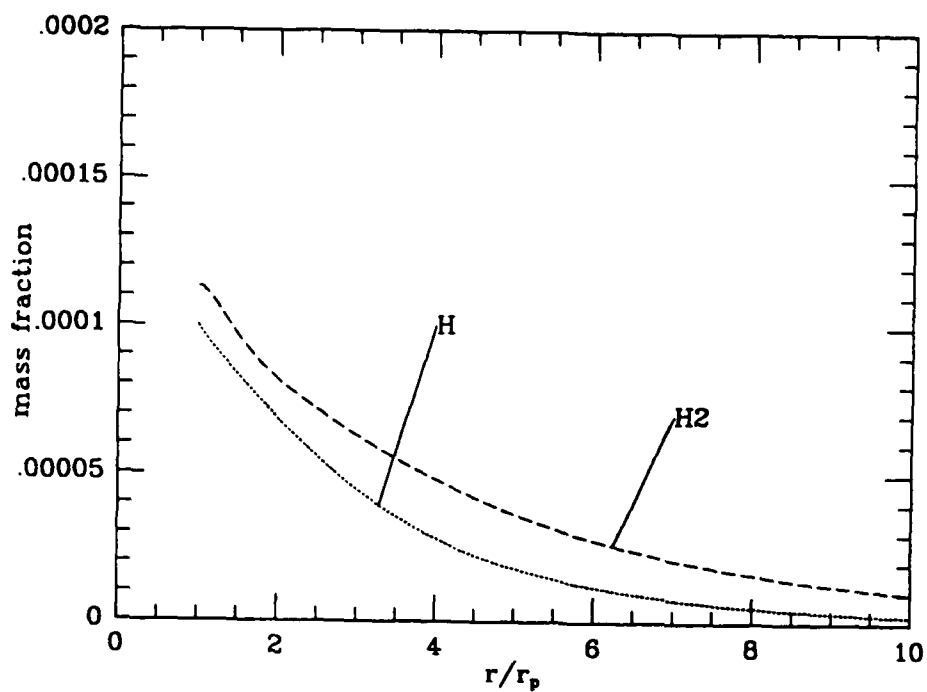


Figure 4.13. Species Mass Fraction Radial Profiles for the Oxidation of a 200 μm Spherical Boron Particle in a JP4/air Mixture at an Ambient Temperature of 1400 K (Continued)

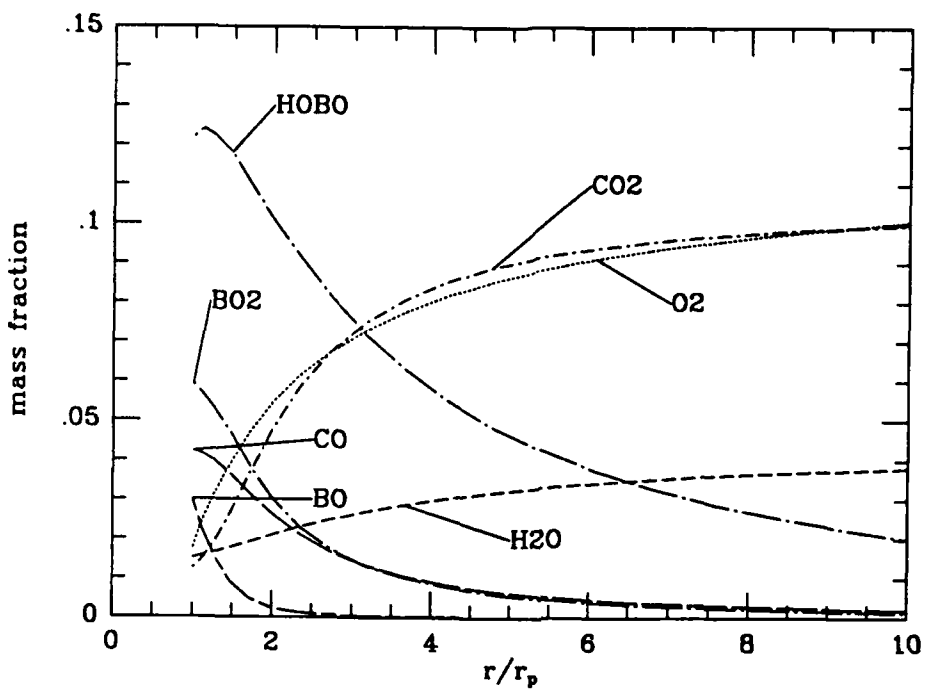


Figure 4.14. Species Mass Fraction Radial Profiles for the Oxidation of a 200 μm Spherical Boron Particle in a JP4/air Mixture at an ambient temperature of 2000 K

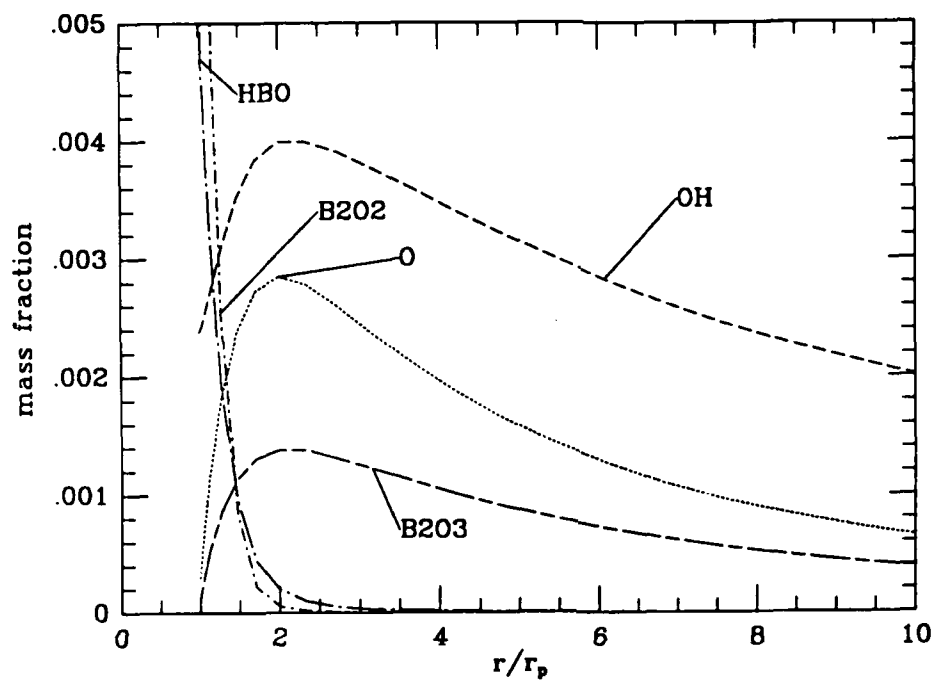


Figure 4.14. Species Mass Fraction Radial Profiles for the Oxidation of a 200 μm Spherical Boron Particle in a JP4/air Mixture at an ambient temperature of 2000 K

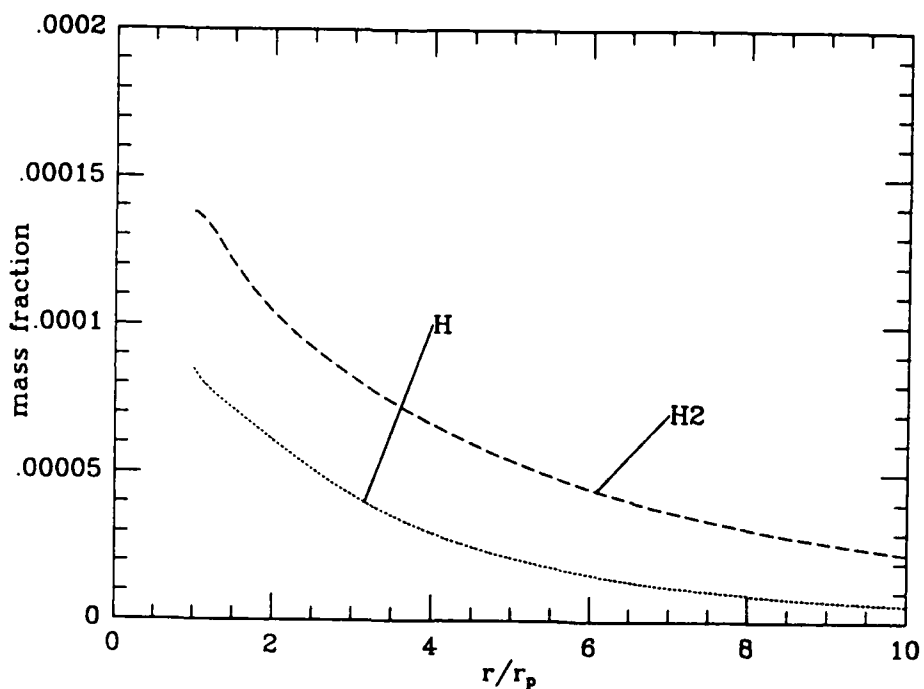


Figure 4.14. Species Mass Fraction Radial Profiles for the Oxidation of a 200 μm Spherical Boron Particle in a JP4/air Mixture at an ambient temperature of 2000 K (Continued)

Overall, therefore, the model results indicate that the species distribution near the particle surface is predictably governed by heterogeneous surface reactions. However, homogeneous gas phase chemistry rapidly converts the species formed through surface reactions to the primary boron oxidation products of HOBO(g) and $\text{B}_2\text{O}_3(\text{g})$. At radial distances greater than ca. one particle radius from the surface, the species distribution and temperature is governed by gas phase oxidation reactions. Because the products of surface reactions undergo gas phase reactions so quickly, the gas phase chemistry is largely independent of the surface chemistry. The feature is consistent with earlier modeling results for the gas phase oxidation model⁴⁻³ and a continuously stirred reactor model⁴⁻⁴ for coupling between surface reactions and gas phase chemistry.

4.3 References for Section 4.0

4-1 Turns, S.R., Holl, J.T., Solomon, A.S.P. and Faeth, G.M., "Gasification of Boron Oxide Drops in Combustion Gases," Combust. Sci. and Tech. 43, 287 (1985).

- 4-2 Macek, A., "Combustion of Boron Particles at Atmospheric Pressure," Combustion Science and Technology 1, 181 (1969).
- 4-3 Yetter, R.A., Rabitz, H., Dryer, F.L., Brown, R.C. and Kolb, C.E., "Kinetics of High Temperature B/O/H/C/ Chemistry," Combustion and Flame 83, 43 (1991).
- 4-4 Brown, R.C., Annen, K.D., Kolb, C.E., Cho, S.Y., Yetter, R.A., Dryer, F.L., and Rabitz, H., "First Annual Report on Boron Combustion Model Development with Kinetic Sensitivity Analysis," Aerodyne Research, Inc. Report No. ARI-RR-703, May 1989.